Materials Analysis Using a THz Imaging System Based on Atomic Vapour

NOURAH FAHAD ALMUHAWISH

Materials Analysis Using a THz Imaging System Based on Atomic Vapour

Nourah Fahad Almuhawish

A thesis submitted in partial fulfilment

of the requirements for the degree of

Doctor of Philosophy

Quantum Light and Matter

Department of Physics

Durham University

United Kingdom

October 10, 2022

Materials Analysis Using a THz Imaging System Based on Atomic Vapour

Nourah Fahad Almuhawish

October 10, 2022

Abstract

This thesis studies the response of the interaction between Rydberg atomic vapour and a THz frequency field. When Caesium atoms at room temperature are excited to a Rydberg state using three infrared lasers and a 0.55 THz field resonant with the $14P_{3/2} \rightarrow 13D_{5/2}$ transition is applied, the atoms respond by emitting a green optical fluorescence corresponding to the $13D_{5/2} \rightarrow 6P_{3/2}$ decay. This response is exploited to investigate the absorption coefficient for different polymer materials that transmit well in the THz frequency range using the Beer–Lambert law. We calibrate the system to obtain a measure of THz intensity. As the THz imaging system is highly sensitive to environmental changes, and to show that our results are consistent, we provide a comparison of results between our atomic detection method and a commercial thermal power meter. Additionally, we measure the absorption coefficient of the same materials at a frequency of 1.1 THz, and the results are compared with those measured at 0.55 THz. The THz imaging system is also used to perform some experiments in order to demonstrate its effectiveness in real-world applications. The system provides an interesting image contrast in the case of a sample containing two different polymer materials measured at two THz frequencies. The result is a proof-of-concept that multispectral THz imaging can provide additional information and is motivation to improve our THz imaging system by introducing a dual-species THz imager. We also investigate the polarisation spectroscopy of an excited-state transition of rubidium vapour at room temperature as a step towards a rubidium THz imaging system. The narrow dispersive signal produced by this spectroscopy technique is ideal for laser frequency stabilisation of excited-state transitions.

Acknowledgements

At this moment of accomplishment, I would like to express my heartfelt thanks to everyone who has helped me through my PhD journey. First and foremost, I would like to thank my supervisor, Kevin Weatherill, for his patience, support, encouragement, suggestions, confidence in me, guidance and response to my questions and queries promptly. With his help, I was able to overcome many difficulties. I am greatly indebted to him for understanding my situation, especially with my children due to Covid-19. I have been extremely lucky to have a supervisor like him. Thank you also to my second supervisor, Charles Adams, for the suggestions and invaluable advice he provided in our weekly meetings. Thanks must also go to all the members of the THz team, especially to Lucy for her welcome in the early days of my arrival in Durham and for being a great listener. She has been a solid support, showing me laboratory tactics and allowing me to inherit too well-calibrated experiments, as well as providing theoretical modelling. I would like to extend my sincere thanks to Matt and James for their help. Thanks, too, to Shuying and Andrew for the great teamwork.

Throughout my life, I have been encouraged and supported by my family; I wouldn't be where I am today without them. Thanks to my parents, Fahad Almuhawish and Hanan Almuqern, for being the best role models and showing faith in me since I was a child, for their support and giving me the liberty to choose what I desired to shape my life. Thanks to my siblings Muneerah, Abdullah, Abdulraouf, Waad and Faisal for supporting me with their jokes and showing me how no matter what I am going through, I will make it through to the end– and now you can stop asking "when will you finish and be back".

There are no words to express my gratitude to my husband, Abdullah Alateeq, because it is so boundless. Thanks with love for his unwavering love, endless support, encouragement and being my best friend and an amazing father to our

children. I am grateful to him for given up so much to make my dream and career a priority in our lives. Thanks to the unconditional love of my children, Seba and Mohammed, for their patience during my studies and for being beside me throughout this journey; they have seen me through the ups and downs and are waiting for me to finish to call me "Dr. Mum". Thank you to my friends especially Arwa who has supported me throughout my journey.

Finally, I would like to acknowledge the support of King Faisal University and the Saudi Arabian Cultural Bureau in the United Kingdom for a full scholarship.

Contents

Declaration

The work in this thesis is based on research carried out in the Quantum Light and Matter group, Department of Physics, Durham University, England. No part of this thesis has been submitted elsewhere for any other degree or qualification, and it is the sole work of the author unless referenced to the contrary in the text.

List of Figures

List of Tables

Chapter 1

Introduction

This thesis is a convergence between two considerably different fields: Rydberg atomic physics and THz wave technology. Studies of Rydberg atoms have developed into a mature discipline, and they are particularly attractive for quantum technologies. However, THz radiation is still a relatively new field of research in comparison to other regions of the electromagnetic spectrum. This is not because the THz band is not particularly interesting, but instead because generating and detecting THz radiation can present particular challenges. Nevertheless, in recent years, the use of THz technologies has expanded rapidly and made considerable progress. This thesis aims to use Rydberg atoms in a thermal vapour as a THz detector to image an incident THz field. We will first give an overview of the THz field applications and detectors, before introducing the technique of Rydberg atom sensing.

1.1 THz technology

The THz band is known as the region in the electromagnetic radiation spectrum, which is usually defined as 0.1–10 THz corresponding to wavelengths between 300 mm and 30 μm, bridging the gap between the microwave and infrared (IR) regions [1, 2]. Moreover, since the THz band extends over a different region of the

electromagnetic spectrum, they can give complementary information about the image than microwaves, infrared, visible, ultraviolet, or x-ray images.

There are a wide range of THz systems being developed today, and their applications have been used across a range of different sectors, such as in industry [3] and health care [4]. The properties of terahertz waves lead to the exploitation of this field in many real-world applications and multidisciplinary research fields. One unique feature of THz radiation is its ability to penetrate optically-opaque materials such as plastics, cloth, and paper. This makes THz a suitable technology for non-destructive testing (NDT), for instance, industry-wide quality control in pharmaceuticals [5], food inspection [6], inspect packaging [7], historical art objects [8, 9] and in security applications, such as in the detection of concealed objects, drugs, and explosives [10, 11, 12, 13]. Where microwaves share this characteristic of being able to penetrate materials, THz radiation offers superior spatial resolution due to its short wavelength [14, 15].

In terms of safety, the low photon energy of THz radiation makes it non-ionising ($\sim$ 4.1 meV at 1 THz) [16]. This gives it an advantage as a potential security tool for in vivo sensing [17, 18, 19]. Additionally, as THz radiation is highly sensitive to absorption by polar substances, such as water [20], this radiation can be exploited to monitor the ingress of water through building materials [21].

It must be noted that there are many advantages to THz radiation, but the technology has not been fully explored nor its potential wholly realised. Due to the lack of THz wave sources and insufficiently sensitive detectors, THz radiation has been called the "terahertz gap" [22].

The THz spectrum lies at the boundary between mature and well-developed technologies. The concepts of these existing devices cannot be modified to detect THz frequencies in the visible and IR waves, which are detected by semiconductor photodetectors devices and microwave and radiowaves, which are detected by high-speed electronic devices. Due to the fact that semiconductor photodetectors devices have

band gaps greater than the THz photon energy, this leads to the band-gaps of semiconductors shrinking at THz frequencies and thermal noise starting to dominate, making the semiconductor devices unsuitable for detecting the THz band. At high frequency, the efficiency of conventional electronic devices decreases and they do not respond well to the THz frequency.

In recent years, the development of THz technology has proliferated, and many systems have been developed to utilise this technology.

1.2 THz Detectors

The detection methods in the THz frequency range can be classified into two main categories: coherent and incoherent detectors. A coherent detector detects both the phase and amplitude of the THz signal and is also known as an indirect or 'heterodyne' detector. These detectors use a nonlinear device to mix the THz radiation signal with a local oscillator [23]. Time-resolved coherent detection of pulsed THz fields led to the development of THz time-domain spectroscopy (THz-TDS) [24].The most common techniques that apply THz coherent detection are commonly performed through photoconductive antennae [25, 26] and electro-optic sampling (EOS) [27, 28].

Incoherent detectors are only sensitive to the intensity of the THz signals and are known as direct detectors. THz imaging can be performed using incoherent detectors, and the image can be acquired either by a single-pixel imaging technique or an array of pixels. Despite the former technique offering better spatial resolution, the latter has a speed advantage. Several THz imaging systems in transmission and reflection modes have been exploited using different THz detector technology. For instance, liquid helium cooled bolometers [29], Schottky diodes [30], pyroelectric detectors [31] and Golay cells [32].

1.3 THz Imaging

As early as 1976, T. S. Hartwick recorded the first terahertz images using an optically pumped molecular THz laser [33]. Several decades later, the first THz two-dimensional imaging was demonstrated [34], based on an optoelectronic THz time-domain spectroscopic (THz-TDS) imaging system using femtosecond lasers. Since then, a variety of different imaging techniques have emerged and developed. In most cases, the THz imaging system uses a single pixel detector which is required to scan the sample in two dimensions.

Many THz imaging applications have been limited by the time needed to form images. The development of THz technology and the increasing range of THz sources and detectors have demonstrated that no one technology is ideally suited to solving all problems. As a result, many different THz imaging systems have been used to form images. THz imaging system sources can be classified as continuous-wave imaging, and pulsed THz imaging [35, 34].

1.3.1 Single Pixel Imaging

The majority of THz imaging systems that have been reported are based on single-pixel imaging and use time-domain spectroscopy (TDS) [36]. Single-pixel imaging systems are based on raster-scanning the sample through a focused beam. An image is formed by pixel-by-pixel acquisition with serial data acquisition using a photoconductive detector. The process of this method is usually slow, resulting in the speed at which images can be acquired being severely limited.

The first TDS imaging system used a single-pixel detector by Hu and Nuss in 1995 [34]. This system used a femtosecond optical source and two pairs of off-axis paraboloids. The first paraboloid was to form a focal spot on the object plane between the THz transmitter and THz detector. THz radiation from the sample is collected and focused on the THz detector using another pair of paraboloids. This imaging

system acquired the image of a 4.5 cm × 2.3 cm leaf sample after 48 hours. However, in modern THz imaging systems using this raster-scanning method, higher speed methods are employed. In broadband THz pulse imaging (TPI) systems using time-domain spectroscopy [37], in addition to the acquisition being slow due to the mechanical scanning of each pixel, the other drawbacks are depending on bulky and expensive ultrafast laser sources to generate and detect THz radiation, and TPI systems are limited to low THz power. An object can be imaged by raster scanning across the THz beam. Therefore, TDS imaging systems take a long time to acquire images and are not suitable for many applications. An alternative approach to THz imaging is based on a narrowband range of continuous wave (CW) source. For example, backward-wave oscillators [38] and CW photomixer [35].

In recent years, quantum cascade lasers (QCLs) [39] have emerged as being well suited to THz imaging as they are compact, easy to use, and they deliver CW high output power exceeding 100 mW [40]. QCLs with various different single-pixel detectors have been reported. For example, a Golay cell which is the most common type of thermal THz detector based on the heating and expansion of a gas, where the thermal expansion is in response to heating. The advantages of the Golay cell detector include the ability to operate at room temperature, so there is no need for cooling, and it is relatively simple and low in terms of running costs. Disadvantages of this detector are the significant thermal mass resulting in a relatively slow time constant of around 1 second and large noise generated by internal thermals [41]. Using raster scanning of the 8 cm × 7.5 cm sample and a Golay cell detector with QCL emitting at 3.1 THz reported an acquisition time of 1.5 hours [42]. Raster scan imaging at 2.9 THz using a point contact Schottky diode mixer (SDM) at room temperature and a QCL were also reported [30]. Such a system can achieve a suitable resolution where metal strips 350 μm wide can be seen clearly with an acquisition time of 100 ms/pixel.

THz imaging in reflection geometry has recently been demonstrated based on a self-mixing in a QCL. A single QCL in CW mode operating at 2.6 THz is used as

the source and detector, where the object was raster scanned in two dimensions. Using this system, an image of a coin with the size of 25.9 mm × 25.9 mm was obtained with high resolution in 19 minutes [43].

The single-pixel systems suffer by being a time-consuming procedure for image acquisition, often taking several seconds per pixel. For larger images, the total acquisition time can reach several hours. In recent studies, single pixel systems have been improved to overcome these time limitations. For example, Rothbart and co-workers [44], used THz imaging systems in transmission mode using a 2.5 THz QCL source and a sensitive photoconductive single-pixel detector. This technique is based on a flat, fast scanning mirror, which deflects the beam in the direction of the object. However, this system can only achieve an acquisition time of 240 μs per pixel. For example, a THz image of 4 cm × 3.6 cm that consisted of 77 × 70 pixels with a size pixel of 0.55 mm could be imaged in this system at an acquisition time of 1.1 s.

Systems that use a multi-pixel spatial light modulator (SLM) could provide a more effective alternative to conventional imaging techniques that rely on single pixels. A THz spatial light modulator can be controlled optically through photoconductivity in a high resistivity silicon wafer and controlled by a digital micro-mirror device (DMD), which allows computational imaging with a single pixel detector. This technology acquired THz images with speeds up to 0.5 Hz [45]. A state-of-the-art single-pixel detector using THz pulse source and DMD can today achieve THz imaging in 32 × 32 pixels at six frames per second [46].

Single-pixel imaging systems can achieve high-resolution imaging as the image is formed by using pixel-by-pixel scanning. However, this is a slow process which results in the acquisition speed being limited; so, this system has not yet demonstrated the capability of real-time imaging.

1.3.2 Focal Plane Arrays (FPAs)

Focal plane arrays (FPAs) are the detectors used as an electronic integrated circuit in hand-held cameras. They operate in video mode to provide real-time THz imaging. The focal plane array works in parallel order rather than serial. This imaging system can acquire images in a single shot for frequencies below 300 GHz which results from the lack of suitable low-noise amplifiers [47]. This imaging system uses different array detectors, such as those based on complementary metal oxide semiconductor (CMOS) field effect transistors (FETs) [48, 49, 50], Schottky diodes [51, 52], or microbolometers [53, 54].

The first real-time THz 2D imaging using FPAs was in 2005 [53]. This imaging system used a far infrared gas laser (FIR) as an illumination source with an uncooled infrared microbolometer camera based on thermal infrared array sensors. The camera had 160 $\times$ 120 pixels with a pixel pitch of 46.25 μm. In the set-up at 2.52 THz, images of the sample of 29 mm $\times$ 1 mm were acquired at the 60 Hz frame rate, with an acquisition time of 16 ms. As an alternative, a real-time THz imaging system combined a quantum cascade laser (QCL) at 4.3 THz as an illumination source with a 320 $\times$ 240 pixels microbolometer focal plane array camera, with a pixel pitch of 46.25 μm [54]. The illuminated area of this system covered roughly 3 $\times$ 3 cm^2 in the object plane; each row of pixels samples was taken in 64 μs, as the focal plane array camera contained 240 rows with an inactive time of 1.47 ms. The total acquisition time was 16.6 ms per frame with a 60 Hz frame rate. Due to the sensitivity of microbolometers to both infrared and THz radiation, the uneven infrared background can be subtracted using a reference frame which leads to a reduced frame rate of 20 Hz. A different study was conducted by the same group with the same experimental set-up [55]. Over a distance of 10 m, the 4.3 THz QCL laser achieved good results at real-time imaging. However, at a longer distance of 25 m, the quality of the image decreased. Therefore the QCL laser was set at 4.9 THz, which is more suitable for long-range imaging. In this case, the

camera, which was located around 23 m from the QCL source, a 1 cm sample was imaged in real-time at a 20-frame average at 1 s, and there was a delay of 5 ms in displaying the images.

Also, the other study by [56], used a microbolometer camera which has 320 × 240 pixels with a pixel pitch of 50 μm and illuminating QCL laser was able to give real-time images for characters written with metallic ink on paper at a frame rate of 25 Hz. There have also been several studies that use this imaging system technique [57, 58]. Their results showed that microbolometer arrays were not sensitive enough to THz radiation, so a high power THz source was required [55]. A significant improvement in sensitivity could be achieved by designing focal plane array microbolometer cameras and optimising for THz frequency range [59].

Since CMOS offers high yield and low costs, a particular focus has been placed on CMOS integrated THz detector arrays. For instance, the first FET focal plane array using 0.25 μm CMOS as THz detectors for imaging was conducted by [60]. This imaging system contained an array of 3 × 5 pixels where the image of a postal envelope with hidden office supplies could be captured at 0.65 THz. Subsequently, a FET detector made from 65 nm Silicon on insulator (SOI) CMOS technology was also reported at 0.65 THz, as through the SOI, the sensitivity of the detector can be improved [61]. In the study [62], the group used a THz CMOS camera with a focal plane array of 1 k pixels. This camera contains the scanned area of 2.9 × 2.9 mm^2 which is divided into 32 × 32 pixels. Using this technique an image of a metal wrench with a 6 mm opening could be acquired with a frame rate of 25 Hz at 0.65 THz.

In a study that imaged a copper ruler from a CMOS THz imager of 31 × 31 pixels array with a pixel pitch of 240 μm, the images were displayed from a video at a frame rate of 100 frames per second [63]. Using a Schottky diode detector in 130-nm CMOS for imaging at 0.28 THz has been demonstrated [51]. Through this imaging system of 175 × 175 pixels, the sample of 70 mm × 70 mm can be imaged in 20 minutes, and the measurement time for each pixel was 40 ms.

The Trichopoulos group [64] performed broadband real-time THz imaging using backward heterostructure diode (HBD)-based FPA. The 31 × 31-pixel camera operated in the frequency range of 0.6–1.2 THz, capturing images at a rate of 5 frames per second and 12 seconds per pixel. This imaging system could image a steel screw 15mm × 8mm that was placed inside an envelope at 0.7 THz.

These detection arrays are uncooled systems running at room temperature and have a high level of complexity. Their sensitivity is limited, and their speed depends on underlying detector technology [59, 51]. The spatial resolution is limited by the pixel numbers and the pixel size of the FPAs and can be a challenge to increase [65]. However, high sensitivities are possible with cooled sensors such as the focal plane arrays for the photodetector array camera and spectrometer (PACS). These arrays are very expensive to fabricate and integrate, and their cooling operation requirements present a challenge for their use in real-world applications [66]. Although this imaging system can achieve even real-time imaging using a focal-plane array microbolometer camera with QCL, fringe patterns appear in the THz image [67].

1.3.3 Frequency Conversion

There have been significant advancements in real-time THz imaging technology in the past few years. Nonlinear optical wavelength up-conversion is a promising approach to detecting THz radiation. This method is based on the theory that any wavelength can be converted to a new wavelength in the range of sensitivity of a photon detector [68]. This technique uses a nonlinear medium such as crystal diamond sample [69] or $4-\text{dimethylamino}-\text{N}'-\text{methyl}-4'-\text{stilbazoliumtosylate}$ (DAST) [70, 71]. The study that used DAST crystals to generate THz radiation and up-convert to near IR [71] can image a 28 mm × 28 mm sample clearly at room temperature and at a frame rate of 60 frames per second. However, this requires high THz power, so this system used a frequency of 19.3 THz owing to the greater power of the THz wave that is emitted by the DAST crystal. As this system re-

quires high THz power to obtain a signal that can be measured, the system can only be operated using pulsed THz fields. This leads to the limitation of the frame rate of the system by the source repetition rate.

Recently, a new technique for THz-to-optical conversion has been reported in near-field [72] and far-field THz imaging [73]. This technique is based on atomic vapour at room temperature, where THz radiation is converted into visible light. In this thesis, we aim to use the work in [73] to extract a measure of THz intensity and material analysis.

Long acquisition times remain one of the biggest obstacles to the widespread application of THz imaging technology. A THz imaging system using single-pixel detectors is the most common system because most systems cannot afford expensive THz cameras. Table 1.1 summarises the advantages and disadvantages of the above imaging systems. Some of these studies, whose sample sizes are known, will be compared with our imaging system by converting their sample sizes to our imager size (1 cm^2).

Imaging Technology	Single Pixel Imaging			Focal Plane Arrays			Frequency Conversion	Atomic method
Performance	[34] (TDS)	[43] (TDS)	[44] (TDS)	[53] (MBM)*	[62] (CMOS)	[64] (HBD)	[71] (DAST)	[73]
Operation frequency (THz)	1-3	2.6	2.5	2.52	0.65	0.7	19.3	0.55
Imaging area (cm^2)	4.5 × 2.3	2.59×2.59	4 × 3.6	2.9×0.1	0.29 × 0.29	1.5 × 0.8	2.8 × 2.8	1 × 1
Acquisition time	48 h	19 min	1.1 s	16 ms	40 ms	200 ms	16 ms	0.3 ms**
Frame rate (fps)	-	-	-	60	25	5	60	3000
Acquisition time for imaging 1 cm^2	4.6 h	2.8 min	76 ms	60 ms	500 ms	170 ms	2 ms	0.3 ms
Advantages	High spatial resolution, offer spectral information			Real-time imaging, high speed depends on the detector technology			Real-time	Ultra-high-speed video, requires low THz power, sensitivity is high, diffraction limited spatial resolution
Disadvantages	Slow, not real-time			Complex system, expensive, sensitively is limited, requires high power, spatial resolution is limited			Requires high THz power	We do not get spectral information

Table 1.1: Comparison table of state-of-the-art THz imaging systems.
*(MBM) is a shorthand of microbolometer.
** In this work the standard exposure time used 200 ms.

1.4 Rydberg Atoms

A Rydberg atom, named after the Swedish spectroscopist Johannes Rydberg, is an atom excited to a higher state characterised by the principal quantum number n [74]. Atoms in the Rydberg state are both larger and exhibit various exaggerated properties, which are greater by several orders of magnitude than in lower states. Such atoms have, for example, a tremendous response to electric and magnetic fields and a strong dipole moment in the microwave and THz frequency regions; they are also known to have extremely long radiative lifetimes. In Rydberg atoms, the electron cloud size is proportional to the square of the principal quantum number. As a result of this size scaling property, other properties are scaled in tandem, including the lifetime, which is scaled as n^3, sensitivity to electric fields scaling as n^7, the size of the transition dipole matrix element between Rydberg states is scaled as n^2 and the orbital radius increases as n^2, whilst the binding energy of the Rydberg electron decreases as n^{-2} [75]. Researchers have extensively studied and exploited the properties of Rydberg atoms for many applications including quantum information processing [76], single photon sources [77], nonlinear optics [78], quantum simulation [79], electrometry [80, 81] and long-range Rydberg molecules [82].

Rydberg atoms have previously been demonstrated to be excellent electromagnetic field sensors in the radio frequency, microwave and THz ranges [83, 84, 85]. Rydberg atoms also have been used as receivers for AM and FM radio communication [86], and this technique is extended in a system that use a Rydberg atom-based mixer technique which allows for radio frequency phase measurements [87, 88].

Rydberg atoms have been exploited for imaging IR and THz fields [89, 90], using Rydberg atoms as photocathodes which is a destructive technique based on ionisation of atoms in the gas phase and the image is formed by detecting the resulting charges.

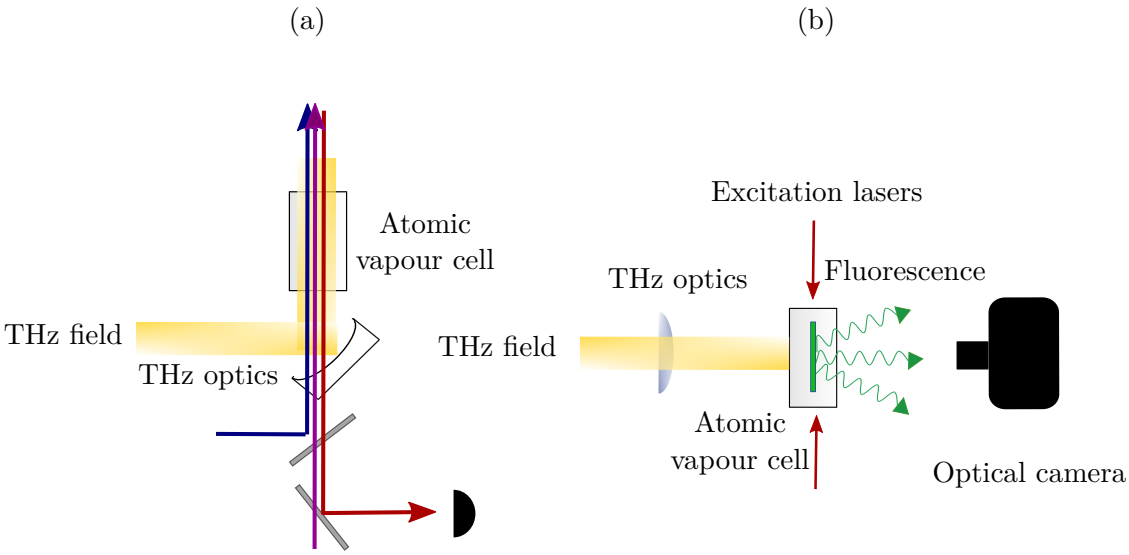

Figure 1.1: **Basic experimental setup:** (a) Experimental setup of EIT optical coherent detection [81]. (b) Experimental setup of atom-based THz imaging. Atoms in the vapour cell are excited by using excitation lasers into a Rydberg state and create a light sheet. A THz field propagating perpendicular to the excitation lasers at the position of the light sheet in the vapour cell induces fluorescence which is imaged using an optical camera.

However, as the electron in the Rydberg atoms is very far from the nucleus, these atoms are highly sensitive to other Rydberg atoms, and external electromagnetic fields, in particular to microwave and terahertz fields [91]. As Rydberg atoms have have well-known properties and their measurements are reproducible, this makes the Rydberg atomic sensor traceable to SI units. Recently, electromagnetically induced transparency (EIT) based on the Rydberg atom in a thermal vapour have been used for microwave electrometry [91, 80] and THz electrometry [81] measurements. There is also an EIT approach using a radio frequency field which is on-resonance with a Rydberg transition using Autler–Townes (AT) splitting [92], and an approach which is based on using two atomic species, Cs and Rb simultaneously [93].

EIT based detection involves a coherent optical probing - the applied electric fields on the atoms are detected at a photodiode as shown in Fig.1.1(a), which gives an SI tractable measurement of the electric field. In contrast, our method [94] using spontaneous emission provides a fast method for acquiring spatial information

about the field, but lacks the SI traceability of the EIT method. Our imaging system based on Rydberg atoms in a thermal vapour as a sensor to image THz frequencies is shown in Fig.1.1(b). We excite atoms contained within an atomic vapour cell using excitation lasers to create a light sheet of excited Rydberg atoms at the position of the vapour cell. A THz field propagates perpendicular to the excitation lasers at the position of the light sheet of Rydberg atoms, which acts as THz sensor and converts THz radiation into visible green fluorescence.

1.5 Thesis Structure

Chapter 2 discusses some of the theoretical concepts that underlie this thesis. These concepts will be used to interpret the experimental results in the subsequent chapters. Initially, we will give an overview of atomic structure, including fine and hyperfine splitting and electric-dipole moments; then, we introduce a Hamiltonian, which will be used to describe the dynamics of the atomic system.

Chapter 3 describes the experimental techniques used in this work, including laser systems, THz sources, and experimental layouts. In addition, the chapter provides details on the cell design and data collection methods.

Chapter 4 introduces an approach for measuring the absorption coefficient of materials in the THz range using an atomic imaging system. We also calibrate the imaging system to measure THz intensity. We will use this calibration to measure the absorption coefficient of different common polymers at a frequency of 0.55 THz using the Beer–Lambert law. These results will be compared with a commercial thermal power meter in order to prove our results are consistent.

Chapter 5 presents experimental results that demonstrate the usefulness of our THz imaging system. These experiments illustrate our THz imaging system's applicability to non-destructive testing (NDT) and security applications. We examine the contrast of an imaging sample containing two different polymer materials that are imaged at two different frequencies of THz.

Chapter 6 demonstrates progress toward multispectral imaging in the THz range by using two species in the same cell. To do that we investigate polarisation spectroscopy of an excited state transition in room-temperature rubidium vapour to be used for frequency stabilisation of laser coupling excited state transitions. The circularly polarised coupling beam will induce anisotropy in the atomic medium which will be probed on the excited-state transition. The linearly-polarised probe is decomposed into two circular polarisation components which results a narrow dispersive signal. We will investigate this signal as a function of the coupling power.

1.6 Publications

The following publications are the results of the work described in this thesis:

• Nourah F Almuhawish, Shuying Chen, Lucy A Downes, Matthew J Jamieson, Andrew R MacKellar, and Kevin J Weatherill. Polarization spectroscopy of an excited state transition in rubidium. OSA Continuum, 4(10):2598–2605, 2021. https://doi.org/10.1364/OSAC.439037

• Nourah F Almuhawish, Lucy A Downes, Matthew J Jamieson, Shuying Chen, and Kevin J Weatherill. Materials analysis using THz imaging system based on atomic vapour. In preparation.

Chapter 2

Atomic Structure and Atom-light Interactions

This chapter presents some of the theoretical concepts that are the foundation of this thesis. These concepts are used to interpret the experimental results that will be presented in the remaining chapters. Firstly, we will discuss how atomic structures are calculated, including fine and hyperfine splitting and how this is related to the work that has been done in this thesis. In the rest of this chapter, we will introduce a two-level system of atom-light interactions and how these states are coupled by dipole matrix elements, which is the basis for understanding many aspects of atomic physics. We then focus on more complex dynamics in systems with three levels. Finally, this chapter concludes with a consideration of atoms in a thermal vapour and how that will change the detunings in the Hamiltonian.

2.1 Atomic Structure

The structure of the atom is based on quantum mechanics theory. Throughout the history of atomic theory, it underwent many developments. Bohr's model of hydrogen [95] provides a great starting point for describing atomic structure. The main contribution of Bohr's models, often referred to as Bohr's semi-classical

theory, is the stationary state concept [96]. He postulated that the energy levels of hydrogen are quantised and related to the frequency by

$$h\nu_{fi} = E_f - E_i, \tag{2.1}$$

where ν_{fi} is the frequency between the initial and final states and h is the Plank's constant, E_i and E_f are the energies of the initial and final states where $E_f > E_i$.

Bohr's model also proposed the existence of the energy levels of hydrogen atoms, which can be expressed as [95]

$$E_n = -hc\frac{R_\infty}{n^2}. \tag{2.2}$$

Eq.2.2 known as the Rydberg formula, where n is the atomic principal quantum number, and when the atom is excited to high n states, it is called the Rydberg atom. R_∞ is the Rydberg constant, h and c are the Planck's constant and speed of light, respectively.

2.1.1 Alkali Metals

Alkali metals are Group 1 elements of the periodic table. Rubidium and caesium have become standard substances in atomic physics experiments due to the fact that their structure is relatively simple and resembles atomic hydrogen as there is only a single valence electron. Diode lasers used for rubidium and caesium are a low-cost technology. In CD players, the first cheap commercial diode lasers operated close to the rubidium ground-state transition of 780 nm [97]. In experiments rubidium and caesium are placed inside a glass vapour cell. In terms of pressure, significant atomic vapour pressure is present inside the cells at room temperature and increases with temperature. This allows for very high optical densities to be achieved relatively quickly to changes in temperature, which gives measurable signal levels [98]. The ability to manufacture small-scale thermal vapour cells with high optical density has

enabled the development of a variety of products, such as microwave electrometry based on Rydberg atoms [99], chip-scale atomic magnetometers [100], and terahertz detectors [101]. Alkali atoms can be described using a modified version of Eq.2.2 as

$$E_n = -hc\frac{R_\infty}{(n-\delta_l)^2}. \tag{2.3}$$

where δ_l refers to the quantum defect [102]. From this expression, the energy levels depend on both n the atomic principal quantum number and l the angular momentum. The quantum defect arises due to a pure Coulomb potential no longer being experienced by the valance electron, and it depends on l, where the quantum defect will be different for each value of l. When the electron is excited to high n states with higher angular momentum states l the electron is on average farther away from the core, and that means the interaction of the electron with the core decreases. As a consequence, the quantum defect also decreases and will be small relative to the lower angular momentum states.

2.1.2 The Schrödinger Equation

The Schrödinger equation can be described by the wavefunction ψ of the electron in a quantum mechanical conception. The time-independent Schrödinger equation for an electron with mass m_e in a spherically symmetric potential $V(r)$ can be written as,

$$\left(\frac{-\hbar^2}{2m_e}\nabla^2 + V(r)\right)\psi = E\psi, \tag{2.4}$$

where ψ is the wavefunction of the electron, $\hbar$ is the reduced Plank's constant, and E is the energy of the electron. For this potential V(r), the wavefunction can be expressed through the separation of the radial and angular parts and can be written as

$$\psi(r,\theta,\phi) = R_{n,l}(r)Y_{l,m}(\theta,\phi), \tag{2.5}$$

here $R_{n,l}$ defines the radial function of the solution where n and l are the principal and angular momentum quantum numbers, respectively. Where the spherical harmonics describe the angular function $Y_{l,m}$ and m is the magnetic quantum number; there are $2l+1$ possible values of m for each value of l within a range of values from $-l$ to l.

2.1.3 Fine Structure

The fine structure is caused by relativistic effects, which are not described by the Schrödinger equation and emerge from interactions between the effective magnetic field. This interaction is generated by the motion of the electron around the nucleus and is described by the electron orbital angular momentum L with the electron spin S, and that known as spin-orbit coupling (**L**.**S**) [95].

In the (**L**.**S**) spin-orbit coupling regime, the total angular momentum of the electron **J** is given by[95]

$$\mathbf{J} = \mathbf{L} + \mathbf{S}, \tag{2.6}$$

now l, j, m_j are the good quantum numbers to describe the system and m_s is no longer good quantum number. The spin-orbit coupling shifts the energy and can be calculated from [95]

$$E_{\mathrm{FS}} = \frac{\beta_{\mathrm{FS}}}{2}[J(J+1) - L(L+1) - S(S+1)], \tag{2.7}$$

where β_{FS} is the spin-orbit constant that has a different value for each value of l and s. The total angular moment number j has values between $|l-s| \leq j \leq l+s$. In the atom that has a single valance electron such as caesium $s = 1/2$, in the

states $l = 0$ there will be no change in the energy as $j = s$. So spin-orbit coupling leads $l > 0$ states to be split in pairs with values $j = l + 1/2$ and $j = l - 1/2$, and this is known as the fine structure splitting. In this thesis we use caesium and rubidium atoms. If we want to describe them in this coupling we need to use this notation nL_j where $L = S, P, D$ for $l = 0, 1, 2$ etc. So we can write the ground states of Cs as $6S_{1/2}$ and Rb as $5S_{1/2}$ using quantum numbers $n = 6, l = 0, j = 1/2$ in Cs and $n = 5, l = 0, j = 1/2$ in Rb. We will use this notation for energy levels in this thesis.

2.1.4 Hyperfine Structure

The hyperfine structure is the result of the interaction between the nuclear spin **I**, and the total angular momentum of the electron **J** that produces the total angular momentum in the hyperfine coupling regime [95].

$$\mathbf{F} = \mathbf{I} + \mathbf{J}. \tag{2.8}$$

The total angular number F has values that are in the range $|J - I| \leq F \leq J + I$. Each fine structure state will be split into multiple hyperfine states by this interaction, and these hyperfine states have an energy shift that is given by [95]

$$E_{\mathrm{HFS}} = \frac{A_{\mathrm{HFS}}}{2}[F(F+1) - I(I+1) - J(J+1)], \tag{2.9}$$

Eq.2.9 is only valid for $j = 1/2$. where A_{HFS} is the magnetic dipole constant that has different values for each value of I and J. For caesium with a nuclear spin quantum number $I = 7/2$, this will split the ground state $6S_{1/2}$ into two hyperfine states with $F = 3$ and $F = 4$.

2.1.5 Transition Dipole Moment

The dipole interaction between two states $|1\rangle$ and $|2\rangle$ of the valence electron is a measure of the strength of the coupling between the two states that are coupled by the electric dipole moment of the electron. This is characterized by the matrix elements of the position vector operator $\boldsymbol{\mu} = e\mathbf{r}$. The dipole operator can be defined as $\mu = e\mathbf{r}.\hat{\boldsymbol{e}}$, where $\mathbf{r}$ is the position vector and $\hat{\boldsymbol{e}}$ is the unit vector where the electric field polarisation is directed. The dipole matrix element for the transition between state $|1\rangle$ and state $|2\rangle$ in the integral form is given by [103]

$$d_{21} = -\int \psi_2{}^*(\mathbf{r})\mu\psi_1(\mathbf{r})d(\mathbf{r}), \tag{2.10}$$

if state $|1\rangle = |n, l, m\rangle$ and state $|2\rangle = |n', l', m'\rangle$, the transition dipole moment is given by

$$d_{n'l'm',nlm} = -\int \psi_2{}^*(\mathbf{r})\mu\psi_1(\mathbf{r})d(\mathbf{r}). \tag{2.11}$$

By decomposing the wavevectors $\psi_{1,2}$ into the product of radial and angular states using Eq.2.5 that can be written as

$$\begin{aligned} \psi_1(\mathbf{r}) &= R_{n,l}(r)Y_{l,m}(\theta, \phi), \\ \psi_2(\mathbf{r}) &= R_{n',l'}(r)Y_{l',m'}(\theta, \phi). \end{aligned} \tag{2.12}$$

In order for parity to be conserved through the electromagnetic interactions, the solution of the integral should be non-zero, which is finite for the radial part but for the angular part is only non-zero if $l' - l = \pm 1$ and $m'_l - m_l = [-1, 0, 1]$. Therefore, the dipole matrix element can only connect states with the opposite parity. $[-1, 0, 1]$ are the three components of the polarisation vector $\hat{\boldsymbol{e}}$ with respect to the quantisation axis of the atom which is corresponding to $[\sigma^-, \pi, \sigma^+]$ transitions. When the light is linearly polarised along the quantisation axis, the polarisation

vector is denoted by π, and when the light is circularly polarised in two opposite directions with the atomic quantisation axis aligned with the light propagation direction, the polarisation vector is denoted by $\sigma^{\pm}$ [95]. In order to find the dipole matrix element, we will transfer the polarisation vector from a cartesian basis into a convenient basis of vectors [103],

$$\begin{aligned} \epsilon_0 &= e_z, \\ \epsilon_{\pm} &= \frac{1}{\sqrt{2}}(e_x \pm i e_y). \end{aligned} \tag{2.13}$$

By relating the dipole operator to spherical harmonics, it can be written as

$$\mu_q = e\mathbf{r}.\boldsymbol{\epsilon}_q = er\sqrt{\frac{4\pi}{3}}Y_{l,q}(\theta,\phi), \tag{2.14}$$

where $Y_{l,q}(\theta,\phi)$ is a spherical harmonic function and $q = [-1, 0, 1]$, as $q = 0$ drives π transitions and $q = \pm 1$ drives $\sigma^{\pm}$ transitions.

Then the dipole matrix element is given by [104]

$$\langle n', l', j', m'_j|\mu_q|n, l, j, m_j\rangle = (-1)^{j'-m'_j} \begin{pmatrix} j' & 1 & j \\ -m'_j & q & m_j \end{pmatrix} \langle n', l', j'||\mu_q||n, l, j\rangle, \tag{2.15}$$

where $(\cdots)$ denotes the Wigner-3j coefficient, the angular terms which is sometimes referred to as the Clebsch-Gordan coefficient which is proportional to Wigner-3j coefficient but having a $1/\sqrt{(2j+1)}$ prefactor [105], and the term $\langle \cdots||\mu_q||\cdots\rangle$ is the reduced matrix element, which has no angular dependence and can be derived from wavefunctions radial overlap.

2.1.6 Spontaneous Decay

According to the Einstein A coefficient, the spontaneous decay rate on transition $|n, l\rangle \rightarrow |n', l'\rangle$ is proportional to the square of the reduced matrix element and is given by [106]

$$A_{n,l\to n',l'} = \frac{1}{4\pi\epsilon_0\hbar}\frac{4\omega_{n,n'}^3}{3c^3}\frac{l_{max}}{2l+1}|\langle n',l'||er||n,l\rangle|^2, \tag{2.16}$$

where $\omega_{n,n'}$ is the transition frequency between states $|n,l\rangle$ and $|n',l'\rangle$, l_{max} is defined as the largest angular momentum between l and l' and $\langle n',l'||er||n,l\rangle$ is the reduced matrix element.

There are many transitions that occur from the initial state $|n',l'\rangle$. The lifetime τ_0 of a state can be determined from the total rate of spontaneous transitions from the nl state to all allowed lower-lying states and is given by the relation

$$\frac{1}{\tau_0} = \Gamma_0 = \sum_{E_{n,l}>E_{n',l'}} A_{n,l\to n',l'}. \tag{2.17}$$

Blackbody photons can also initiate the transition between lower and higher states. A blackbody's temperature T determines the average number of photons per mode $\bar{n}_\omega$ at the transition frequency, based on the Planck distribution [106]

$$\bar{n}_\omega = \frac{1}{e^{\hbar\omega_{n,n'}/k_BT}-1}. \tag{2.18}$$

where k_B is Boltzmann's constant. The rate of blackbody radiation (BBR) induced transitions ($W_{n,l\to n',l'}$) is related by the Einstein A-coefficient and the average number of photons per mode at the transition frequency, based on the Planck distribution as

$$W_{n,l\to n',l'} = \bar{n}_\omega A_{n,l\to n',l'}, \tag{2.19}$$

The total rate of BBR-induced transitions can be written as:

$$\Gamma_\mathrm{BBR} = \sum_{n'} W_{n,l\to n',l'}, \tag{2.20}$$

By summing the spontaneous transition rate and the rate of transitions driven by BBR we can obtain the effective lifetime of the state (τ_eff)

$$\frac{1}{\tau_{\text{eff}}} = \Gamma_0 + \Gamma_{\text{BBR}}. \tag{2.21}$$

2.2 Atom-Light Interactions

An atom experiences excitation when interacting with a monochromatic field whose frequency is near-resonant. This section presents a semi-classical description of the interaction between a classical electromagnetic field with a quantised atomic system.

2.2.1 Two-Level System

A two-level atom system is the simplest case with which to begin. The two levels included in this system are the ground state $|1\rangle$ with energy $\hbar\omega_1$ coupled to the excited state $|2\rangle$ with energy $\hbar\omega_2$. This coupling is induced by a laser with frequency ω; when the laser is detuned from resonance is given by $\Delta = \omega - \omega_0$, where $\omega_0 = \omega_2 - \omega_1$ is the transition frequency. The state of this system is described by the wavevector as $|\psi\rangle = c_1|1\rangle + c_2|2\rangle$ and $c_{1,2}$ are the probability amplitudes of the system of the atom for being in the ground and excited state respectively. The total Hamiltonian $\hat{\mathcal{H}}_{\text{tot}}$ of the system is composed of two components [95]

$$\hat{\mathcal{H}}_{\text{tot}} = \hat{\mathcal{H}}_0 + \hat{\mathcal{H}}_{\text{int}}(t), \tag{2.22}$$

where $\hat{\mathcal{H}}_0$ is the unperturbed atomic Hamiltonian, and $\hat{\mathcal{H}}_{\text{int}}$ is the Hamiltonian for the atom-light interaction of the field that is time-dependent. The effects of dephasing processes will be ignored, and we will focus on the dynamics of the system. The unperturbed atomic Hamiltonian $\hat{\mathcal{H}}_0$ is given by

$$\hat{\mathcal{H}}_0 = \begin{pmatrix} \hbar\omega_1 & 0 \\ 0 & \hbar\omega_2 \end{pmatrix} \equiv \begin{pmatrix} 0 & 0 \\ 0 & \hbar\omega_0, \end{pmatrix} \tag{2.23}$$

In classical electromagnetic theory, the electromagnetic field can be modelled as an incident plane-wave optical field of frequency ω and polarisation vector $\hat{\boldsymbol{e}}$ propagating in the z-direction. In this case, the electric field is given by $\boldsymbol{E} = E_0\hat{\boldsymbol{e}}\cos(kz-\omega t)$. With the dipole approximation, which can be used when the wavefunctions of the atom are much smaller than the wavelength of the light, the z dependence of the electric field can be neglected in this case by considering interactions only with infrared, visible, and THz radiation. The dipole approximation electric field can be written as $\boldsymbol{E} = E_0\hat{\boldsymbol{e}}\cos(\omega t)$. This classical electromagnetic field couples states $|1\rangle$ and $|2\rangle$ through an electric dipole transition with a dipole operator μ to produce the interaction Hamiltonian,

$$\hat{\mathcal{H}}_{\text{int}} = -\mu E_0\cos(\omega t), \tag{2.24}$$

$$= \frac{\boldsymbol{d}_{21}E_0}{2}(|2\rangle\langle 1| + |1\rangle\langle 2|)(e^{i\omega t} + e^{-i\omega t}), \tag{2.25}$$

where $\boldsymbol{d}_{21}$ is the dipole matrix element for a two-level system, that is defined in Eq.2.15. By inserting Eq.2.23 and Eq.2.25 in Eq.2.22 the total Hamiltonian can be written as

$$\hat{\mathcal{H}}_{\text{tot}} = \frac{\hbar}{2}\begin{pmatrix} 0 & \Omega(e^{i\omega t} + e^{-i\omega t}) \\ \Omega^*(e^{i\omega t} + e^{-i\omega t}) & \hbar\omega_0 \end{pmatrix}, \tag{2.26}$$

where Ω is the Rabi frequency which is defined as

$$\Omega = \frac{\boldsymbol{d}_{21}E_0}{\hbar}. \tag{2.27}$$

2.2.2 Rotating Frame Transformation

Based on the Rotating Wave Approximation (RWA), the rapidly oscillating terms in off-diagonal elements that oscillate at approximately twice the frequency of the driving field can be eliminated since their time dependence averages out over the

much slower timescale of the evolution of the atomic populations coefficient c_1 and c_2 [107]. This leads the total Hamiltonian in Eq.2.26 to be written as

$$\hat{\mathcal{H}}_{\text{tot}} = \frac{\hbar}{2}\begin{pmatrix} 0 & \Omega \\ \Omega^* & 2\Delta \end{pmatrix}, \tag{2.28}$$

where $\Delta = \omega - \omega_0$. By diagonalising this Hamiltonian we can find the eigenvalues and eigenstates. The eigenvalues are given by

$$E_{\pm} = -\frac{\hbar\Delta}{2} \pm \frac{\hbar}{2}\sqrt{\Delta^2 + \Omega^2}. \tag{2.29}$$

Eigenstates are bare states of a system in the absence of a field ($\Omega = 0$), but when the field which is near resonant ($\Delta \approx 0$) is applied, the bare states are no longer eigenstates and are given by

$$|\pm\rangle = \frac{1}{\sqrt{2}}(|1\rangle \pm |2\rangle). \tag{2.30}$$

The ground and excited states will be shifted with the opposite sign. We can see from Eq.2.29, that when Ω is increased, the energy levels $E_{\pm}$ will be shifted further from each other. This shift is referred to as the AC Stark shift or light shift [95].

2.2.3 Three-Level System

In this section, we consider a three-level system as shown in Fig.2.1. The methods that are presented in section 2.2.1 are extended to an atomic system with three levels. The new atomic system as shown in Fig.2.1 can be described as the ground state $|1\rangle$ with energy $\hbar\omega_1$, an intermediate state $|2\rangle$ with energy $\hbar\omega_2$ and an excited state $|3\rangle$ with energy $\hbar\omega_3$. The ground state and intermediate state are coupled by the Rabi frequency Ω_{12}, shown by the red arrow in Fig.2.1, in which the resonance is detuned by $\Delta_{12} = \omega - \omega_{12}$. In addition to the first coupling, the intermediate state is coupled to the excited state by Rabi frequency Ω_{23}, shown by the blue

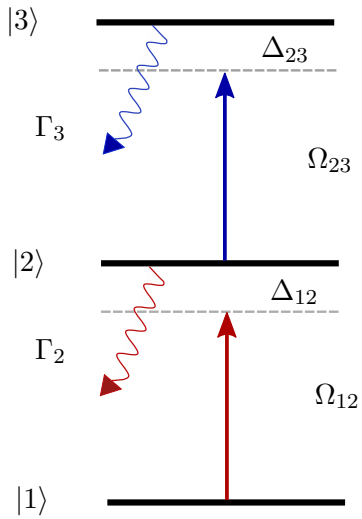

Figure 2.1: **Three-level ladder system:** The three ladder are ground state $|1\rangle$, intermediate state $|2\rangle$ and excited state $|3\rangle$. They are coupled by two driving fields with Rabi frequencies $\Omega_{12,23}$ frequencies of two driving fields, detuned from resonance by $\Delta_{12,23}$. The decay from the first and second excited states is given by $\Gamma_{12,23}$.

arrow in Fig.2.1, in which the resonance is detuned by $\Delta_{23} = \omega - \omega_{23}$. This thesis focuses on the 'ladder' configuration as the most straightforward case where the state $|i+1\rangle$ has higher energy than $|i\rangle$.

The total Hamiltonian in the interaction picture for this three-level system using rotating wave approximation is given by

$$\hat{\mathcal{H}}_{\text{tot}} = \frac{\hbar}{2}\begin{pmatrix} 0 & \Omega_{12} & 0 \\ \Omega_{12} & -2\Delta_{12} & \Omega_{23} \\ 0 & \Omega_{23} & -2(\Delta_{12}+\Delta_{23}) \end{pmatrix}. \tag{2.31}$$

In order to more fully understand the mechanism of this atom-light system, we should consider the dressed states under the following conditions. The first consideration is that the coupling between $|2\rangle$ and $|3\rangle$ states is stronger than the coupling of the $|1\rangle$ and $|2\rangle$ states ($\Omega_{12} \ll \Omega_{23}$). By using $\Omega_{12} = 0$ in Eq.2.31 and diagonalising, the eigenstates can be written as

$$|\pm\rangle = \left(\Delta_{23} \pm \sqrt{\Delta_{23}^2 + \Omega_{23}^2}\right)|2\rangle + \Omega_{23}|3\rangle, \tag{2.32}$$

and the eigenvalues are

$$E_{\pm} = -\frac{\hbar}{2}\left(2\Delta_{12} + \Delta_{23} \pm \sqrt{\Delta_{23}^2 + \Omega_{23}^2}\right). \tag{2.33}$$

When the lower coupling is considered to be weak, we can set $\Omega_{12} = 0$ in Eq.2.31, the two fields are at resonance $\Delta_{12} = \Delta_{23} = 0$, and the dressed states are given by

$$|\pm\rangle = \frac{1}{\sqrt{2}}(|2\rangle \pm |3\rangle). \tag{2.34}$$

where their eigenenergies are separated by $\hbar\Omega_{23}$. By increasing the Rabi frequency Ω_{23} the peak of the absorption profile of these new dressed states splits into two. This effect is known as Autler-Townes splitting [108], and is described in greater detail in Chapter 6.

2.2.4 Doppler Broadening Effect

The Hamiltonian calculations that are described in the previous section are based on the assumption that atoms are stationary. Therefore, all atoms will experience the same frequencies from the applied fields. However, due to the natural linewidth of the transition, the photons do not absorb at a single frequency. Instead, they absorb across a range of frequencies which is described by a Lorentzian distribution, which can be written as [95]

$$g_N(\Delta) = \frac{1}{2\pi}\frac{\Gamma}{\Delta^2 + \frac{\Gamma^2}{4}} \tag{2.35}$$

Here, Γ is the natural linewidth, and Δ is the detuning of the beam $\Delta = \omega - \omega_0$, where ω_0 is the resonance frequency of the transition and ω is the laser frequency. However, in the experiments that are presented in this thesis, we used thermal vapour, so the Doppler shift, which causes an atom moving at different velocities to experience different frequencies, should be considered. In a thermal ensemble of

atoms, the distribution of velocities can be described by the Maxwell-Boltzmann distribution

$$f(v) = \frac{1}{u\sqrt{\pi}} \exp(-\frac{v^2}{u^2}). \tag{2.36}$$

Eq.2.36 is a Gaussian distribution in nature, where u represents the most probable velocity $u = \sqrt{2k_{\mathrm{B}}T/m}$, T is the temperature and m is the atomic mass [95]. By considering an atom travelling at a velocity v with a wavevector k of the excitation laser, Doppler-shifting will be observed in the excitation laser frequency by $\Delta_D = \pm \boldsymbol{k}.\boldsymbol{v}$. Owing to the colinearity of all laser fields in the experiment, the Doppler detuning can be simplified as $\Delta_D = \pm k.v$ as only the velocity component along the propagation is considered. Taking this simplification into account, we are able to modify the detunings in the Hamiltonian in Eq.2.31 and the modified detunings by incorporating the Doppler effect so that it can be expressed as $\Delta_{\mathrm{modified}} = \Delta \pm k.v$, where $(\pm)$ refers to atoms moving either with or against the direction of propagation.

A Gaussian distribution is convolved with a Lorentzian distribution to produce the Doppler broadening of the transitions. This convolution of the atoms $g_D(\Delta)$ can be written as [95]

$$g_D(\Delta) = \int_{-\infty}^{\infty} f(v) g_N(\Delta - kv)\ dv. \tag{2.37}$$

A Voigt profile describes the solution to this integral. The Voigt profile can be well-approximated by a Gaussian distribution when the full-width at half-maximum (FWHM) of the Gaussian is much greater than the Lorentzian FWHM. The linewidth of an atomic transition will be affected by Doppler broadening, and it is determined by natural broadening when the atom is at rest. For example, in a Cs atom, the natural linewidth of the D2 ground state transition is 5.23 MHz [109], whereas atoms in a thermal vapour have a distribution of atomic velocities that is

determined by their temperature. Therefore, the transition linewidth will be inhomogeneously broadened due to the Doppler effect. Then, at room temperature, the linewidth of the ground state transition will be broadened to approximately 500 MHz, which is generally greater than the hyperfine splitting of the excited state. That leads to a loss in resolution in the spectra profile. However, the loss can be retrieved by applying a Doppler-free technique [110].

2.2.5 Optical Bloch Equations

We can describe our quantum atom light system using the density operator $\hat{\rho} = |\psi\rangle\langle\psi|$ which is a generalisation of the quantum state vector. Here $|\psi\rangle$ is a quantum state of an atom which can be described by a superposition of the basis states

$$|\psi\rangle = \sum_i c_i |i\rangle. \tag{2.38}$$

where c_i is the complex coefficient that determines the probability amplitude of being in a basis state $|i\rangle$. The diagonal matrix elements ρ_{ii} represent the evolution of the population of each state, and the off-diagonal matrix elements ρ_{ij} represent the coherence between these states. The Liouville-von Neumann equation [111] is the coherent time evolution of the density matrix, which is equivalent to the time-dependent Schrödinger equation for the state vector; this equation is given by

$$i\hbar \frac{d\hat{\rho}}{dt} = [\hat{\mathcal{H}}_{tot}, \hat{\rho}], \tag{2.39}$$

The term $[\hat{\mathcal{H}}_{tot}, \hat{\rho}]$ describes the commutator between the total Hamiltonian $\hat{\mathcal{H}}_{tot}$ of the atom-light system and the density matrix $\hat{\rho}$. In this semi-classical description, spontaneous emission has not been taken into account. To consider spontaneous emissions, the Liouville-von Neumann equation must be adjusted by adding a decay term, $\hat{\mathcal{L}}$, which is found by the Lindblad master equation for the time evolution of the density matrix [112]

$$\frac{d\hat{\rho}}{dt} = -\frac{i}{\hbar}[\hat{\mathcal{H}}_{tot}, \hat{\rho}] + \hat{\mathcal{L}}. \tag{2.40}$$

Here, $\hat{\mathcal{L}}$ represents the decay and dephasing in the system. The Optical Bloch Equations (OBE) are derived by solving the Lindblad master equation for the time evolution of the density matrix. The decay operator $\hat{\mathcal{L}}$ is split into two components, $\hat{L}_{\text{atom}}$ which describes the atomic decay, and $\hat{L}_{\text{dephasing}}$ which describes the dephasing due to the finite linewidth of the driving fields only affecting coherences that correspond to the off-diagonal density matrix elements. Therefore, the total operator is equal to the sum of these two parts $\hat{\mathcal{L}} = \hat{L}_{\text{atom}} + \hat{L}_{\text{dephasing}}$. In our three-level ladder configuration, we assume that each state decays to the state that is directly below it, the excited state $|3\rangle$ decays to the intermediate state $|2\rangle$ at rate Γ_3, the intermediate state $|2\rangle$ decays to the ground state $|1\rangle$ at rate Γ_2, and there is no decay out of the ground state $|1\rangle$, which is the lowest energy state ($\Gamma_1 = 0$). So the phenomenological decay matrix $\hat{\mathcal{L}}$ for a three-level system can be written as [113]

$$\hat{\mathcal{L}} = \begin{pmatrix} \Gamma_2\rho_{22} & -\gamma_{12}\rho_{12} & -\gamma_{13}\rho_{13} \\ -\gamma_{12}\rho_{21} & \Gamma_3\rho_{33} - \Gamma_2\rho_{22} & -\gamma_{23}\rho_{23} \\ -\gamma_{13}\rho_{31} & -\gamma_{23}\rho_{32} & -\Gamma_3\rho_{33} \end{pmatrix}. \tag{2.41}$$

The decay terms of the coherences can be written as

$$\gamma_{12} = \frac{\Gamma_2}{2} + \gamma_c, \tag{2.42a}$$

$$\gamma_{23} = \frac{\Gamma_2 + \Gamma_3}{2} + \gamma_p, \tag{2.42b}$$

$$\gamma_{13} = \frac{\Gamma_3}{2} + \gamma_p + \gamma_c \tag{2.42c}$$

where γ_p and γ_c are the dephasing decay terms due to the finite linewidth of the first and second fields, respectively. Substituting the three-level total Hamiltonian that is given in Eq.2.31 into the Lindblad master equation in Eq. 2.40 generates

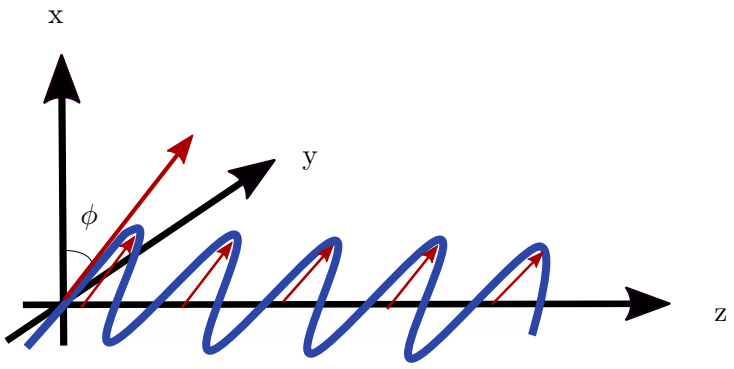

Figure 2.2: **Propagation probe beam in the plane:** Probe beam propagating in the z direction, which is linearly polarised in a plane at the angle ϕ with respect to the x axis.

the time evolution of the density matrix. By expanding this matrix equation as a system of coupled first-order differential equations, we can obtain the motion equations for the density matrix elements. Together, they are known as Optical Bloch Equations and can be written as

$$\dot{\rho}_{11} = \frac{i\Omega_c}{2}(\rho_{12} - \rho_{21}) + \Gamma_2\rho_{22}, \tag{2.43a}$$

$$\dot{\rho}_{22} = \frac{i\Omega_p}{2}(\rho_{23} - \rho_{32}) - \frac{i\Omega_c}{2}(\rho_{12} - \rho_{21}) - \Gamma_2\rho_{22} + \Gamma_3\rho_{33}, \tag{2.43b}$$

$$\dot{\rho}_{33} = -\frac{i\Omega_p}{2}(\rho_{23} - \rho_{32}) - \Gamma_3\rho_{33}, \tag{2.43c}$$

$$\dot{\rho}_{12} = \frac{i\Omega_p}{2}\rho_{13} - \frac{i\Omega_c}{2}(\rho_{22} - \rho_{11}) - (i\Delta_c + \gamma_{12})\rho_{12}, \tag{2.43d}$$

$$\dot{\rho}_{23} = -\frac{i\Omega_p}{2}(\rho_{33} - \rho_{22}) - \frac{i\Omega_c}{2}\rho_{13} - (i\Delta_p + \gamma_{23})\rho_{23}, \tag{2.43e}$$

$$\dot{\rho}_{13} = \frac{i\Omega_p}{2}\rho_{12} - \frac{i\Omega_c}{2}\rho_{23} - (i(\Delta_p + \Delta_c) + \gamma_{13})\rho_{13}, \tag{2.43f}$$

where the dot indicates the first derivative, the solution of the steady-state probe coherence element of the density matrix (ρ_{23}) can be obtained by setting $d\hat{\rho}/dt = 0$ in Eq.2.40, this will be used in Chapter 6.

2.3 Polarisation Spectroscopy Theory

In the two-level atom system, a linearly polarised probe beam travelling in a plane at angle ϕ with respect to the x axis propagates along the z axis as illustrated in Fig.2.2. The probe beam counterpropagates with a circularly polarised pump beam in the atomic medium. The probe and pump beams are derived from the same laser, and the pump beam will induce a birefringence in the medium. The electric field of this probe beam before the atomic medium can be written in terms of the circularly polarised components as [114]

$$\boldsymbol{E} = \begin{pmatrix} E_x \\ E_y \end{pmatrix} = E_0 \left[\frac{e^{-i\phi}}{2} \begin{pmatrix} 1 \\ i \end{pmatrix} + \frac{e^{i\phi}}{2} \begin{pmatrix} 1 \\ -i \end{pmatrix} \right]. \tag{2.44}$$

The linearly polarised probe beam propagates in the birefringent medium of length L. The electric field's components will experience a different degree of absorption and dispersion. The electric field of the probe beam after the birefringent medium is given by [114]

$$\boldsymbol{E} = E_0 \left[\frac{e^{-i\phi}}{2} \begin{pmatrix} 1 \\ i \end{pmatrix} e^{-ik_+ L} e^{-\alpha_+/2} + \frac{e^{i\phi}}{2} \begin{pmatrix} 1 \\ -i \end{pmatrix} e^{-ik_- L} e^{-\alpha_-/2} \right]. \tag{2.45}$$

Here E_0 is the initial field amplitude, $k_\pm = (\omega/c)n_\pm$; where ω and c are the frequency of the field and the speed of light, respectively. $k_\pm$ and $n_\pm$ are the wavevectors and the refractive indices for circularly polarised light that drives $\sigma^\pm$ transitions, and $\alpha_\pm$ are the corresponding absorption coefficients. The change in the polarisation of the probe beam brought about by the birefringence in the medium can be analysed using a crossed polariser which decomposes the probe beam into horizontal S_1 and vertical S_2 linear polarisation components. When we have an atomic transition with the natural linewidth Γ, the difference in absorption coefficients between the circular polarisation components $\Delta\alpha = \alpha_+ - \alpha_-$ is given by [115]

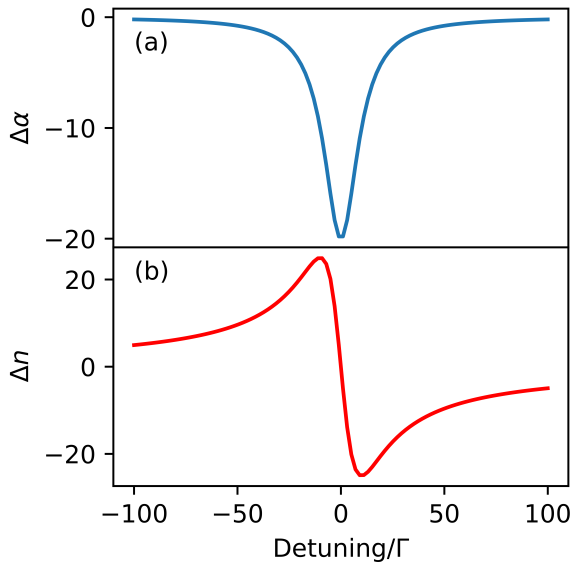

Figure 2.3: **Lorentzian and dispersive lineshapes:** (a) The difference in absorption coefficients between the circular polarisation components has a Lorentzian lineshape. (b) The difference in the refractive index has a dispersive lineshape.

$$\Delta\alpha = \frac{\Delta\alpha_0}{1 + (\frac{2\Delta}{\Gamma})^2}, \tag{2.46}$$

that has a Lorentzian profile as shown in Fig.2.3(a), where Δ and $\Delta\alpha_0$ represent the laser detuning and the maximum difference in absorption coefficients, respectively. According to the Kramers-Kronig relation [116], the difference in the refractive index can be written as [115]

$$\Delta n = \frac{c\Delta\alpha_0}{\omega} \frac{\frac{2\Delta}{\Gamma}}{1 + (\frac{2\Delta}{\Gamma})^2}. \tag{2.47}$$

the form of which has a dispersive profile as shown in Fig.2.3(b), where ω is the frequency of the beam. The sum of the linear polarisation components $S_1 + S_2$ is proportional to $\Delta\alpha$. The difference in absorption coefficient between the circular polarisation components is given by:

$$\frac{S_1 + S_2}{2} \propto \Delta\alpha, \tag{2.48}$$

and the difference between the linear polarisation components $S_1 - S_2$ is proportional to Δn, the difference in refractive index between the circular polarisation components.

$$\frac{S_1 - S_2}{2} \propto \Delta n. \tag{2.49}$$

This will be relevant in the excited state polarisation spectroscopy in Chapter 6.

2.4 Conclusions

In this chapter, we have summarised the theory that forms the foundation of the concepts which will be later described in this thesis. We have provided details about the development of atomic structure—including fine and hyperfine splitting—and explained how the strength of the coupling between two atomic states could be described by the transition dipole moment. The semi-classical description of the atom-light interaction is presented for a two-atom system before extending the model to a three-atom system and illustrating how the thermal velocity of the atoms leads to the Doppler effect. This description allows the Optical Bloch equations to be outlined. This chapter is concluded by an outline of the theory of polarisation spectroscopy, which will be applied in Chapter 6.

Chapter 3

Experimental Methods

In this chapter, we aim to provide technical details of how the experiments in this thesis were implemented and the methods that were employed. The atomic system uses three excitation lasers to reach Rydberg states, as a basis for the experiments. The THz photons, which are conventionally difficult to detect are converted into optical photons which are easily detected, the lasers and THz sources that are used to accomplish this, will be describe in detail. Then we will demonstrate how the THz field will be detected from this configuration, what is the data that will be measured and how the data will be collected. The rest of this chapter will provide details of the experimental layouts that are used in this work, as well as requirements of the vapour cell design to achieve the results.

3.1 Atomic System

The Cs atomic system that is the basis of the experiments in this thesis is shown in Fig.3.1(a). We used IR lasers in three steps to excite the atoms to Rydberg levels, the probe laser (852 nm) excites atoms from $6S_{1/2}$ to $6P_{3/2}$, then the coupling laser (1470 nm) promote the atoms from $6P_{3/2}$ to $7S_{1/2}$. From this state, using the Rydberg laser (840 nm - 885 nm), we can access nP Rydberg states in the range (n=14 - n=12). From the Rydberg state in which the atoms are excited, there will

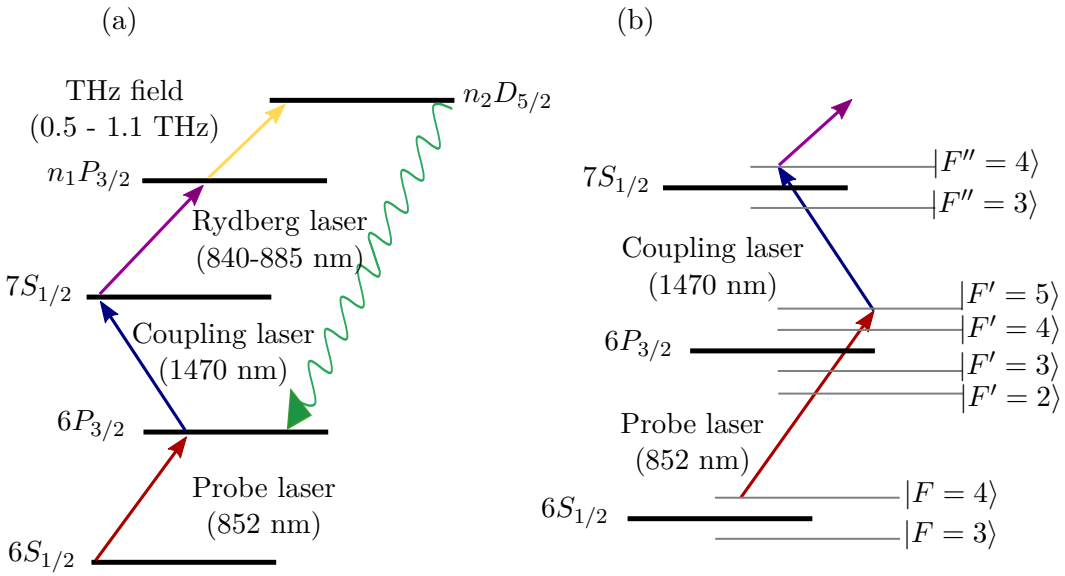

Figure 3.1: **Schematic of the atomic system of caesium involved in this thesis:** (a) The energy levels relevant to the atomic imaging system. The red, blue and purple arrows correspond to the laser excitations, the yellow arrow represents the THz field that couples the two Rydberg states $n_1P_{3/2}$ and $n_2D_{5/2}$. The green arrow is the decay pathway of the optical fluorescence that is emitted from the $n_2D_{5/2}$ state to $6P_{3/2}$ state. (b) The hyperfine structure of the atomic states that is used to lock the first and second lasers in the excitation diagram by using polarisation spectroscopy in ground and excited state transitions. In the lower states the hyperfine states are more separated and when we get up to Rydberg states the hyperfine states are closed together.

be another nearby states, which their transitions are typically in the microwave or THz range.

By applying a THz field in the range (0.5 THz - 1.1 THz) the transition can be driven between these Rydberg states. The neighbouring Rydberg states of alkali atoms are characterized by having electric dipole transitions with extremely large dipole moments in the THz frequency range, causing interaction with a resonant THz frequency. In this thesis we look at two particular states for imaging, for our system we found that the optimum transitions for imaging is $14P_{3/2} \rightarrow 13D_{5/2}$ at (0.55 THz), and $12P_{3/2} \rightarrow 11D_{5/2}$ at (1.1 THz) [94]. Employing a resonant THz field results in transference of the atoms from the $n_1P_{3/2}$ Rydberg state to $n_2D_{5/2}$ THz state, where $n_1 = 14$, $n_2 = 13$ in THz field (0.55 THz) and $n_1 = 12$, $n_2 = 11$ with THz field (1.1 THz). We will discuss these sources in detail later. Coupling

these two states opens a dominant decay channel.

The atomic population that is driven in to the Rydberg state will decay through the random probabilistic process of spontaneous emission. The most probable route is a direct decay down to the $6P_{3/2}$ state, which emits an optical green fluorescence which can be detected. For a 0.55 THz coupled transition $14P_{3/2} \rightarrow 13D_{5/2}$, the strong optical fluorescence corresponding to $13D_{5/2} \rightarrow 6P_{3/2}$ decay occurs at 535 nm [94]. While a 1.1 THz field coupled $12P_{3/2} \rightarrow 11D_{5/2}$ transition, the strong optical fluorescence occurs at 550 nm corresponding to $11D_{5/2} \rightarrow 6P_{3/2}$ decay [94]. This is our signal that can be measured with the spectrometer if we are looking at the wavelengths (what colour it is), and if we want to measure the intensity of the fluorescence (how bright it is) we can use the camera. In this technique, Rydberg atoms are used to convert difficult to detect THz photons to easier to detect visible photons. To perform this technique we use Group 1 metals, predominately Rb and Cs, which have one valence electron. This simplifies our theoretical model, making the required laser frequencies easier to predict. All the experiments presented in this thesis are performed with vapour cells made of quartz, in which atomic vapour is enclosed, allowing optical access to occur. Caesium (Cs) atoms have been preferred to conduct our experiments in Chapter 4 and 5 due to its relatively high number density of $1\text{x}10^{10}$ cm^{-3} at room temperature [109] and single stable isotope (^{133}Cs), making our modeling simple. Throughout these two chapters, the experiments are conducted with the vapour cell with a temperature is monitored to be around $T = 50°$C. This temperature is a balance between having a large enough vapour pressure such that we can obtain measurable signal levels, while not so much density that the probe laser is completely absorbed. In Chapter 6 we use Rubidium (Rb) atom in order to obtain a narrow dispersive signal, which is ideal for laser frequency stabilisation of excited-state transitions as a step towards multispectral imaging in the THz range. The experiment in Chapter 6 is conducted with a room temperature vapour cell, where Rb has a number density of $1.53\text{x}10^{10}$ cm^{-3} at room temperature [117].

3.2 Laser Systems

The probe laser (852 nm) drives the D2 transition which is derived from a commercial External-cavity Diode Laser (ECDL) (Toptica DL100), it is frequency stabilised to the atomic transition $6S_{1/2}|F=4\rangle \rightarrow 6P_{3/2}|F'=5\rangle$ as shown in Fig.3.1(b), using polarisation spectroscopy on the ground state transition [118, 114]. The coupling laser (1470 nm) is produced from a commercial ECDL (Toptica DLPro) and is frequency stabilised to the atomic transition $6P_{3/2}|F'=5\rangle \rightarrow 7S_{1/2}|F''=4\rangle$ using excited state polarisation spectroscopy[115].

In this thesis the experiments were performed by using two different THz frequency sources, therefore, for the final step to reach to Rydberg states, two laser system have been used:

• a MOGLabs cateye diode laser system at 843 nm which is cavity stabilising using (PDH locking) [119]. That was used for experiments in Chapters 4 and 5 to couple to the $14P_{3/2}$ state.

• an MSquared SolsTiS titanium:sapphire laser. The wide tunability of this laser system (700 nm-1100 nm) allows us to access different Rydberg states. Each different Rydberg state provides a different transition of a different THz frequency. For this work, we tuned this laser to 883 nm by a wavemeter reading which is not frequency locked, but is free running. This is demonstrated in Chapter 4 and 5 to couple to the $12P_{3/2}$ state. The lasers and the powers used in the experiments in this thesis are summarised in Table 3.1 below.

3.3 THz Source

Various THz frequencies were used in this work, they are all narrowband and continuous wave. They are generated using an amplifier multiplier chain (AMC), manufactured by Virginia Diodes Inc., a microwave signal generator (HP8672a)

Laser	Wavelength (nm)	Power into vapour cell (mW)	Beam waist at position of vapour cell (μm)
Probe	852	6.5	59
Coupling	1470	13	57
Rydberg	843	62	70
	883	$\sim$100	-

Table 3.1: The lasers and their powers and beam waists that we are used in the measurements for the experiments in this thesis. The powers and the beam waists are measured at the point of the vapour cell.

is used as an input to seed the AMC. Three different AMCs were utilized in the experiments of this thesis. A THz source (A) that has a narrow tuning range (540 GHz to 560 GHz), with a maximum power of 4 mW and input frequency is multiplied by the multiplication factor of 36 to give the eventual THz frequency, was used for the absorption coefficient experiment in Chapter 4 with the frequency set to 550 GHz. The second source (B), had a tunable range between 1010 GHz and 1060 GHz, with a maximum power of 600 μW and a multiplication factor of 72. That was tuned to 1.1 THz frequency for the experiments that required using a different transition as we will see in Chapter 4 and 5. The third source (C), had a tunable range between 500 GHz and 750 GHz, with a maximum power of 50 μW and a multiplication factor of 54. That was used for the imaging experiments in Chapter 5 with 550 GHz frequency when high power was not required. We can set the desired frequency of the three THz sources by tuning the frequency of the input microwave signal that has tuning range between 2 GHz and 18 GHz. In order to launch the THz field into free space, a diagonal horn antenna, manufactured by Virginia Diodes Inc., was used. A THz source (A) is produced a beam containing about 84% Gaussian mode [120]. The proprieties of the THz sources is summarised at Table 3.2 below.

THz source	Tuning range GHz	Maximum power μW	Multiplication factor
A	540 - 560	4000	36
B	1010 -1060	600	72
C	500 - 750	50	54

Table 3.2: The proprieties of THz sources that we are used in the measurements for the experiments in this thesis. .

3.4 Data Readout

This section will discuss the collection and analysis of the detected fluorescence resulting from an incident THz field into the Rydberg atomic vapour.

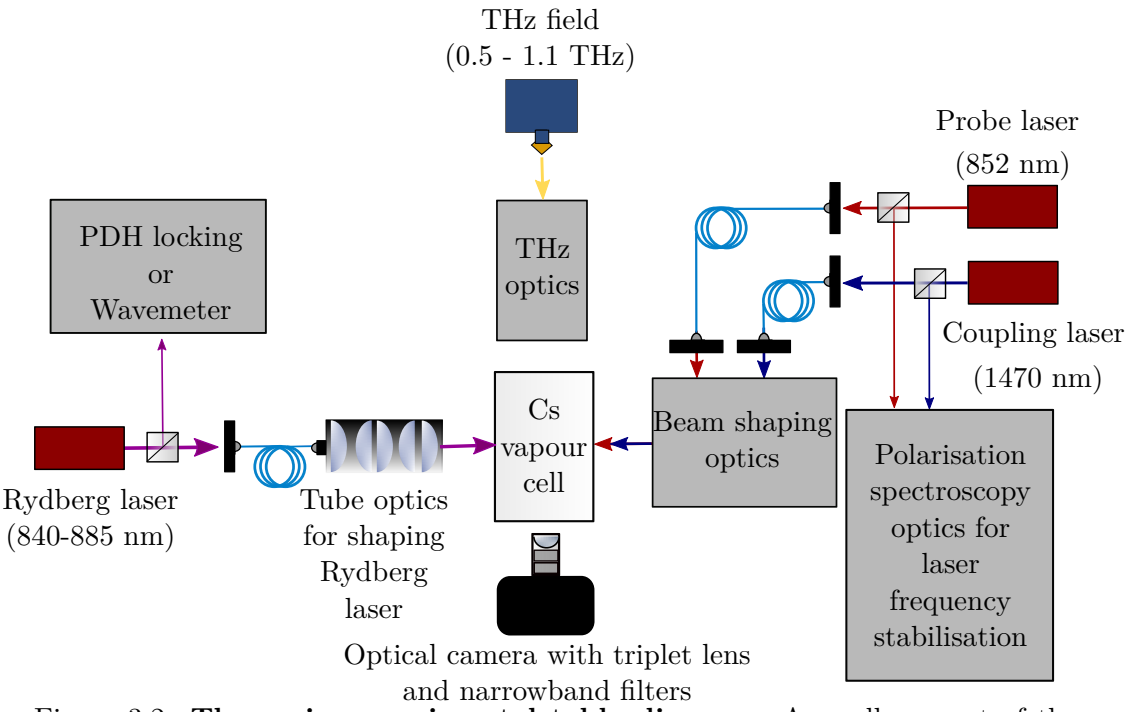

Figure 3.2: **The main experimental table diagram:** A small amount of the beam from the three lasers is used to lock the laser or wavemeter reading, the majority of the beam is sent to the main experiment. All the optics in the table are classified in the gray boxes referring to their functions. This general layout remains the same for all experiments in this thesis.

3.4.1 Camera

All the experiments were performed by using an optical camera to capture images of the fluorescence. We used an Andor iXon EMCCD camera, Also known as iXon, which provided high resolution and low noise, running with an exposure time of 200 ms. The camera used a Steinheil achromatic triplet lens (Thorlabs TRS254-040-A-ML) which is designed to be almost effectively 1:1 magnification. Bandpass filters (Semrock BrightLine 535/6 nm and 505/119 nm) with THz sources A and C, and (Semrock BrightLine 539/30 nm) filter with a THz sources B were used to eliminate the background fluorescence and the scattered IR light from the excitation lasers. The iXon was controlled by the Micro-Manager [121], where the output can be viewed in real time.

3.4.2 Setting THz Power via (UCA) Voltage

At low THz powers there is a linear relation between the fluorescence and THz power [73]. The materials analysis experiment in Chapter 4 works in a low power regime, which can be set by using a user-controlled attenuator (UCA), it is an attenuation voltage that allows us to adjust the THz power out of the source. Increasing the UCA voltage results in a reduction in THz power, the applied voltage controls the amount of attenuation (how much the power is reduced by).

At low THz power, the fluorescence response is linear. Higher THz power results in a non-linear response as seen in Fig.3.3. Afterwards, the system experiences saturation effect and if we keep increasing the power it goes back down again, and we observe a fluorescence lines splitting, resulting in less fluorescence than that without THz. The reduction in power is a result of the atomic line splitting, moving the atomic resonance with the THz field. We should therefore consider that there is a limit of how much THz intensity can be applied to our atoms and still get sensible readings when the power is reduced. To control the THz power via the UCA, we used a multifunction NI USB-6009 data acquisition card through

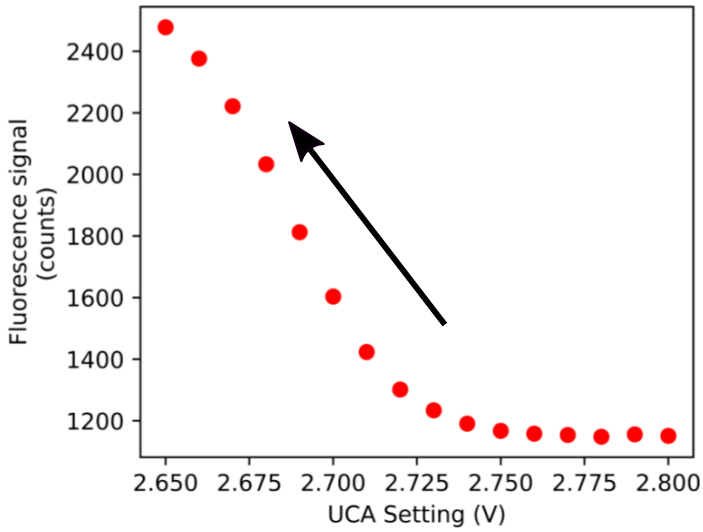

Figure 3.3: **The fluorescence signal as a function of the incident THz power:** We use UCA Voltage to change the power that varying between 2.65 V and 2.8 V. The fluorescence signal starts with curved shape at the high power, then the shape starts to be linear with decreasing the THz power, at the end the signal starts to be constant when the power drops off to zero. The black arrow indicates the direction of increasing THz power.

a LabView computer program. We can change the power by changing the voltage that goes from 0 V to 5 V, where if the voltage is zero then the THz power is at maximum. The UCA response is measured to be less than 10 ms, Therefore in this work, the THz power was set by this method instead of changing the power output from the microwave source, since the microwave source was slow to respond with a delay of 80 ms [94]. For taking the data that requires turning the THz field on and off rapidly, in order to turn THz field off, the UCA was set to maximum attenuation.

3.5 Bench Layout

The bench layout for the experiments that are performed in Chapters 4 and 5 remains the same. There is only one difference between them, for imaging experiments in Chapter 5 a THz lens system is added to the bench layout, where in the material analysis experiment this lens is not required. The bench layout for

Chapters 4 and 5 experiments is shown in Fig.3.2.

We use a three commercial ECDLs IR lasers that are propagated coaxially through the vapour cell. A small amount of light from probe laser at 852 nm and coupling laser at 1470 nm is split off in order to be used in the frequency stabilisation to an atomic resonance. A small amount from Rydberg laser which propagates in the opposite direction to the probe and coupling lasers, is sent to either an ultrastable cavity to stabilise the laser using (PDH locking) or to a wavemeter which provides a wavelength reading. The majority of light from these lasers is sent into the main experiment using single mode polarisation-maintaining fibres which besides allowing the easy realignment of the table they work as spatial filters that helping to obtain a pure Gaussian mode.

3.5.1 Cell Design

The experiments in this thesis are performed by creating a 2D sheet of Rydberg atoms which is a 1 cm^2 THz imaging sensor. All the three laser beams were focused through a cuboidal vapour cell with dimensions (10 mm $\times$ 10 mm $\times$ 60 mm) which allow optical access from 4 sides. In order to achieve the required 50° C temperature and the requirement for optical access, we cannot completely enclose the cell with an insulating Teflon oven, for this reason, we conducts the experiments by using the cell design as shown in Fig.3.4, we used metal ceramic heaters (Thorlabs HT24S) that apply on two sides of the lower part of the cell, after the ceramic heaters are heated, the heat is transferred to the glass. To provide insulation for this part, a Teflon mount surrounds the cell. In order to minimise condensation of Cs on the cell walls, a hole is drilled in a steel metal base to sit the Cs reservoir on, keeping it as the coldest part in the cell. In terms of the upper part, it is open to the air, and a Teflon block is used to hold and insulate a thermocouple which measures temperature at the very top of the cell.

To form a 2D sheet of Rydberg atoms with approximate dimensions (10 mm $\times$

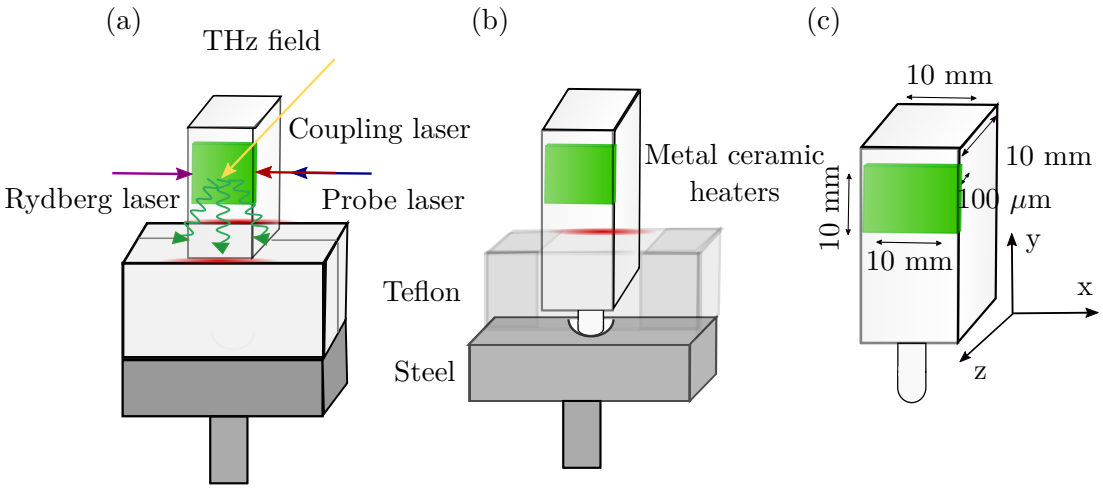

Figure 3.4: **The vapour cell design that is used to perform the experiments in this thesis:** (a) The probe, coupling and Rydberg lasers are overlap along the x axis to form a light sheet (square green region), and the THz field is propagates along z axis. In the front of the cell we can detect the emitted fluorescence. The lower part of the cell is heated by ceramic heaters in two sides (red color) and surrounded by the Teflon insulation which mounted on a steel base. (b) Longitudinal section of Teflon and the steel that is drilled in the center to let the Cs reservoir to sit in. (c) The dimensions of the vapour cell and the light sheet.

10 mm × 100 μm) inside the vapour cell, we expand the probe and coupling laser beams after they come from the fibers in the y direction by using a cylindrical telescopes, then a single cylindrical lens is placed before the cell to focus the collimated beams in the z axis direction into a flat sheet at the vapour cell position. This cylindrical lens is chosen with long focal length (300 mm) to ensure the Rayleigh range of the beam is longer than the length of the cell as shown in Fig.3.5. Therefore, the intensity of the laser remains relatively constant and uniform across the vapour cell. We are interested in the Rayleigh range of the focused beam after it has been focused by the lens, so we need to find the waist of the focused beam w_0 by knowing the incident beam waist w_0' and taking the focal length f of the lens into account [122],

$$2w_0 = \frac{4\lambda f}{\pi D}. \tag{3.1}$$

where D is the diameter of lens, $D = 2w_0'$. From 3.1, the beam waists at the

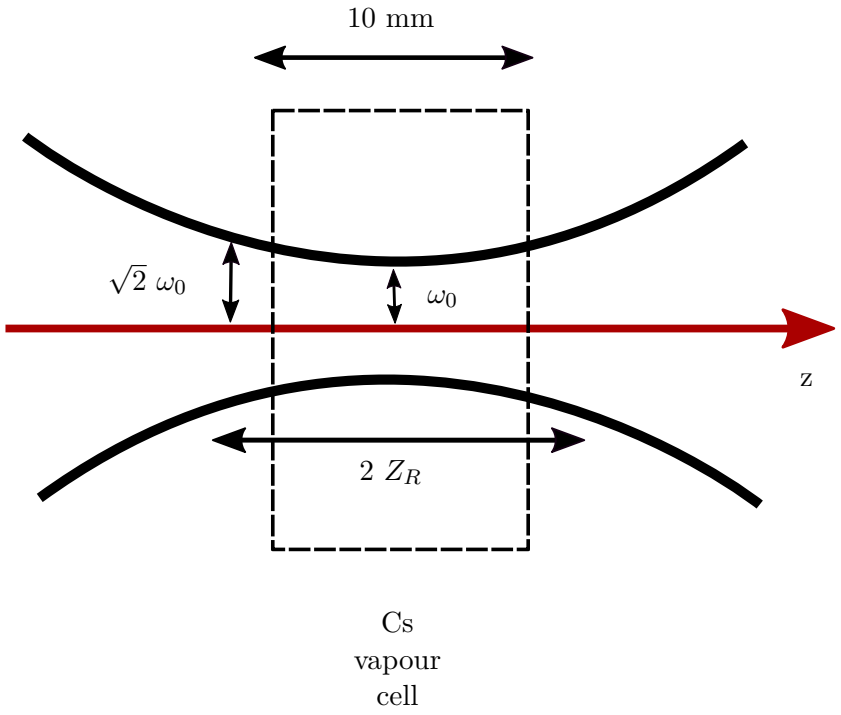

Figure 3.5: **Rayleigh range of the focused beam and the propagation distance:** Rayleigh range (2 Z_R) of the focused beam, with the beam waist ω_0 after it has been focused by the cylindrical lens. The Rayleigh range is longer than the propagation distance across the vapour cell (10 mm).

position of the cell for probe, coupling and Rydberg beams are 59 μm, 57 μm and 70 μm, respectively. In this configuration the Rayleigh range at the position of the cell for probe, coupling and Rydberg beams are 25.3 mm, 13.7 mm and 11 mm, respectively, which are all longer than the propagation distance across the vapour cell, 10 mm. For shaping the Rydberg laser beam, all the lenses are in a commercial tube (Schäfter and Kirchhoff line generator) [123], which contains all the optics that are used to expand Rydberg laser in the y direction then focus it in the z direction. By connecting the fiber to the line generation tube, a light sheet is projected incident onto the vapour cell.

3.5.2 Modes of detection

The experimental setup that is shown in Fig.3.6, is used to conduct the material analysis in Chapter 4 and the imaging work in Chapter 5. Between the two chapters

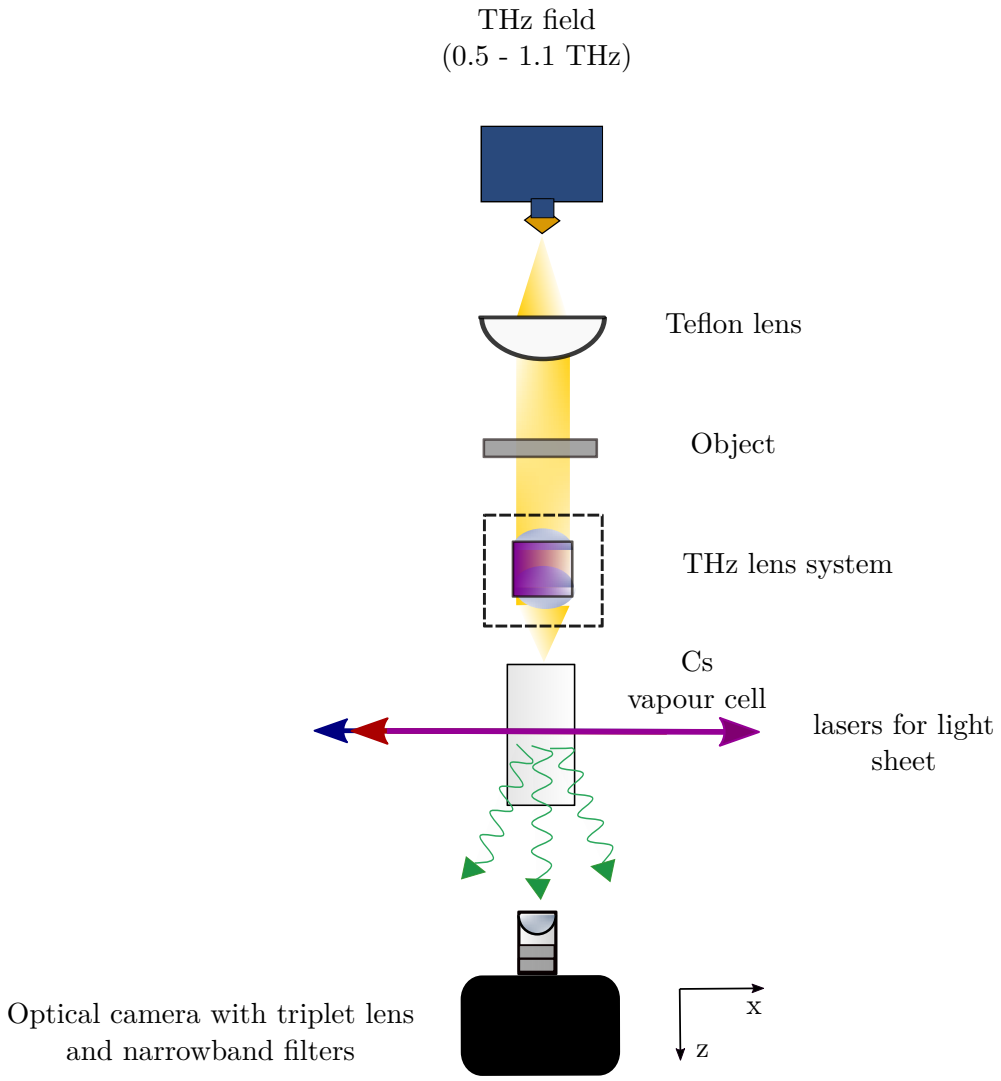

Figure 3.6: **Material analysis and imaging Experimental set-up:** This experimental setup is used for both, material analysis experiment in Chapter 4 and imaging experiment in Chapter 5. The THz field propagates perpendicular to the IR laser beams and is collimated using Teflon lens and the object is layed between the Teflon lens and the cell which is illuminated by the collimated THz beam and imaged in the 2D light sheet. An optical camera is placed in the opposite direction of the incident THz field to capture the fluorescence that is emitted from the cell. The black dashed square indicate the THz lens system which is added to the imaging experimental setup to focus the THz field in the vapour cell.

the setups differ slightly, for the materials analysis the THz lens system which is indicated in black dashed square is not required. The THz lens system is a commercial lens that we obtained from i2S [124]. This lens is designed to be 1:4 magnification depending on where we place it with respect to the object.

The 2D light sheet of Rydberg atoms works as a THz sensor. An image of the incident THz field can be captured in a single shot, by propagating the THz field along the z axis perpendicular to the IR laser beams at the position of the light sheet in the vapour cell. The THz beam is collimated by using a single Teflon lens with a focal length 75 mm which illuminates the target object uniformly. The transmitted THz beam will be focused into the vapour cell by using THz lens system, then the target will be imaged onto the 2D sheet THz imager. By placing an optical camera on the opposite side to the incident THz field the fluorescence that is emitted by the atoms in the vapour cell is captured and the target object will be re-imaged in this optical camera as an image in a single shot.

3.6 Conclusion

In this chapter we have outlined the technical details that were used to conduct the experiments in the following chapters of this thesis. We have described the atomic system that all the experiments are based on and how we use that to detect the THz field. The lasers and the THz sources that are employed to implement the experiments are provided. Detailed explanations of the bench layout and the cell design have been presented. The data that we want to measure and the methods for collecting these data are provided in detail. A setup has been described which will be used for both experiments in this thesis: a materials analysis in Chapter 4 and a THz imaging experiments in Chapter 5.

Chapter 4

Materials Analysis Using THz Imaging

In this chapter, we present an approach to measure the absorption coefficients of polymer materials at 550 GHz using the atomic detection method outlined in the previous chapter. Using our THz imaging system, we are able to extract a measure of THz intensity and apply the Beer-Lambert Law to extract an absorption coefficient. We additionally performed the same experiment with a commercial THz power meter. The results of both methods are presented and compared in this chapter. Furthermore, we measured the absorption of a single thin piece of polymer for the same materials at a frequency of 1.1 THz, and the results are discussed and compared with those obtained at 0.55 THz.

4.1 Introduction

Interactions between matter and THz radiation have been the focus of many research studies with a view toward developing non-destructive and non-contact testing techniques [125, 126]. As a prominent characteristic of THz radiation is its ability to penetrate materials [127] without ionising them, there is an ongoing effort towards utilising it to investigate the properties of various materials. Non-

destructive THz testing methods can, for example, identify an unknown material or illuminate defects at depths that infrared methods cannot reach, without the requirement of a liquid interface as for ultrasound methods [128, 129]. A wide variety of materials have high transmissivity in the THz frequency range, and so THz technology has already been exploited for their investigation, for instance: plastic [130, 131, 3], semiconductors [132], ceramics [133, 134, 135], wood [136, 137, 138], chemical mixtures [139] and gases [140].

Crucial to the development of THz testing techniques and THz technology as a whole is the ability to accurately manipulate THz radiation beams using optical components. With this aim, polymers have demonstrated significant importance for this use owing to their broadband transmission in the THz frequency range [141, 142, 126, 143, 144], meaning they can be used for lenses [145], gratings [146], 3D printed optics [147], mirrors [148], fibers [149] and prisms [150]. This work is partly motivated by scattered literature where there is often little agreement between new and prior research and a lack of transparent reporting, for example, according to Ref. [151] HDPE has an absorption coefficient of $\alpha = 0.225$ cm^{-1}, while the absorption coefficient of the same material is $\alpha = 1.66$ cm^{-1} in [152]. Most investigations into the properties of polymer materials in the THz region have been performed by using terahertz time-domain spectroscopy (THz-TDS) [142, 153, 154, 151, 155], however, some use frequency-domain spectroscopy (THz-FDS) [156, 157, 158], based on processing techniques such as Fast Fourier transform (FFT) or phase fringe extraction has also been reported. THz-TDS uses short pulses of THz wave to probe the properties of a material, whereas THz-FDS and our system use continuous THz wave. THz-TDS and THz-FDS have a wide THz bandwidth of 5 - 6 THz as standard for THz-TDS and reaches to 4 THz for THz-FDS [157], while our system works on one THz frequency and there is progress to have two THz frequencies at the same time. THz-FDS has an advantage over THz-TDS, the price can be significantly lower due to the simplicity of the system architecture. The THz-FDS system is all-fiber coupled and moving optics are

not required. Since our system is still in development, the price point is hard to compare. In a recent study the measurement speed in THz-FDS was measured to be 200 Hz, which is comparable to the speed of most commercial THz-TDS systems [156]. However, our system is a high speed imaging system which can acquire images at 3 kHz [73].

4.2 THz Radiation Transmission Through a Material

When monochromatic light of intensity, I_0, passes through a material with thickness, l, it will be attenuated, resulting in a transmitted intensity I given by the Beer–Lambert Law [159]

$$I = I_0 e^{-\alpha l}, \tag{4.1}$$

where α is the absorption coefficient of the material. By measuring the amount of transmitted light for varying material thicknesses, it is possible to calculate the absorption coefficient at the frequency of interest. By plotting $\ln(I_0/I)$ against the thickness, the gradient can be extracted, which corresponds to the coefficient, (α).

4.3 Extracting THz Intensity from Fluorescence

Most of the information about the atomic system can be found in the fluorescence that is emitted from the atomic vapour cell. In this chapter, we desire to measure the absorption coefficient of materials. In order to perform that, we can collect information about this fluorescence by looking at the fluorescence response of the atoms as a function of THz intensity (or power). By defining the signal from the fluorescence as the pixel value, we can measure the intensity of the fluorescence (how bright it is). In this work, we are only interested in the relative change in the fluorescence intensity between two values in the linear absorption regime; the

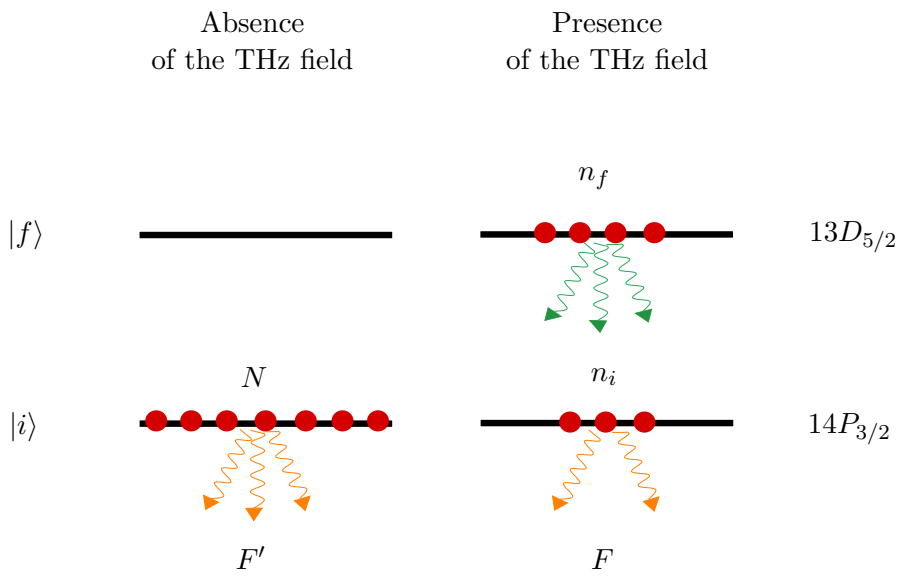

Figure 4.1: **THz imaging system using atomic vapour with THz field on and with THz off:** Two Rydberg states of caesium relevant to the atomic imaging system. To distinguish between the two states, we call the initial state $|i\rangle$, and the second state THz state $|f\rangle$. N is the total number of the atoms, n_i and n_f correspond to the number of excited atoms in $|i\rangle$ and $|f\rangle$ states, respectively. If the THz field is absent, all the atoms are in the $|i\rangle$ state, and when the THz field is present, a percentage of atoms will be excited to the $|f\rangle$ state.

exact intensity value is unimportant. The data was collected using a camera, as described in the methods chapter.

In an ideal experiment, we expect the fluorescence not to fluctuate over time. However, our system is complex, we have temperature fluctuations, laser frequency and intensity fluctuations, mechanical instability, etc. So we need to find a method that is insensitive to these sources of noise and a robust way to characterise how fluorescence is related to the THz intensity. Fluorescence from atoms at a specific energy state f_k can be represented as the number of atoms in that specific state n multiplied by the probability p of an atom in that state emitting a signal photon. In a thermal vapour we have a huge number of atoms that all will be contributing to the signal, the total fluorescence F from this ensemble can thus be written as

$$F = \sum_k f_k = \sum_k (n_k p_k)\,, \tag{4.2}$$

in which the sum spans all relevant atomic states. The total number of atoms can also be defined as

$$N = \sum_k n_k. \tag{4.3}$$

We assume that there are only two states relevant to our system as shown in Fig.4.1, namely the initial i and final f state. It is assumed that the incident THz field excites a proportion of the total atoms N and raises them into the final state, where $n_f = IN$ and I is related to the intensity of the THz field, but it is not a direct measure. As there are only two states, the population of the initial state can be defined as

$$n_i = N(1 - I). \tag{4.4}$$

Moreover, it is impossible to transfer 100% of the population into the final state ($I < 1$), and thus some of the population will always be left behind in the initial state. This is because we are in thermal vapour and we have a lot of coherent dephasing and damping. Therefore, the total fluorescence signal F in the presence of the THz field can be written as

$$F = n_i p_i + n_f p_f \tag{4.5}$$

$$= N(1 - I)p_i + NIp_f \tag{4.6}$$

From Eq.4.6, the relationship between the intensity of the THz field and the total fluorescence signal F can be expressed as

$$I = \frac{F - Np_i}{N(p_f - p_i)} \tag{4.7}$$

$$= \frac{p_i}{p_f - p_i}\left[\frac{F}{Np_i} - 1\right]. \tag{4.8}$$

Eq.4.8 shows that THz intensity I is directly proportional to the total fluorescence F but this is not the case. Although p_i and p_f are constant factors, N often varies between measurements. This variation is a result of fluctuations in laser power and frequency, cell temperature etc. For this reason, F cannot be used as a direct measure of I without considering the changes in N. In the case where the THz field is absent all of the population will be in the initial state, $I = 0$, the fluorescence signal is given by

$$F' = N' p_i. \tag{4.9}$$

If it is assumed that F and F' are recorded in a short time frame, then the atom number cannot alter too much between the measurements. In this case, we can express that as $N \approx N'$ then Eq.4.9 can be written as

$$F' = N p_i. \tag{4.10}$$

By inserting this Eq.4.10 into Eq.4.8 the intensity I can be written as

$$I = \frac{p_i}{p_f - p_i} \left[\frac{F}{F'} - 1 \right]. \tag{4.11}$$

This result eliminates the dependence of I on N and enables any fluctuations in fluorescence resulting from atom number changes during the series of measurements to be negated. In the experiment F when THz is on and F' when THz is off are measured by capturing the fluorescence signal from the cell with an optical camera, as shown in Fig.4.2. The figure shows three images of the fluorescence signal. The one in the center is the raw data when THz field is turned on. The one on the left is the raw data when THz was off and the one on the right is extracting THz intensity from the fluorescence signals using Eq.4.11. In reality, each measurement of fluorescence (image) will include dark counts related to the camera. For cases where the signal is low, these dark counts size can be comparable to the signal size

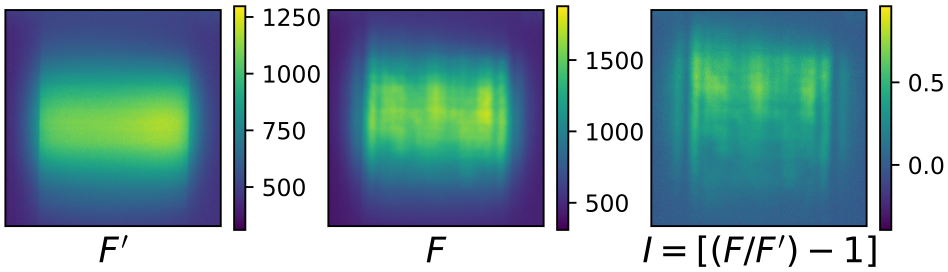

Figure 4.2: **Images of the fluorescence signal:** Three images of the fluorescence signal. The one on the left and in the centre are the raw data, which are the photographs of fluorescence from the cell. When THz is off, the fluorescence signal is given by F' and F when the THz field is turned on. The image on the right is the THz intensity, I, which is calculated by inserting the raw data F' and F into Eq.(4.12).

and thus need to be considered during data analysis, by subtracting dark counts from F and F'. This means our intensity I can be written as

$$I \propto \left[\frac{F - \text{dark}}{F' - \text{dark}} - 1 \right]. \tag{4.12}$$

4.4 Experiments

The measurements are performed with two different THz transmission set-ups as illustrated in 4.3(a) for the atomic detection method and 4.3(b) for the THz power meter method. The atomic detection method has many different parameters that can be changed, such as temperature, laser power etc. We desire to ensure the fluorescence signal is in a linear regime with respect to the power, as we mentioned in Chapter 3, for low THz powers, fluorescence is linearly related to the THz power [73]. We cannot compare the experiment with the theory as the theory is a highly complex system, we cannot model the response of the vapour exactly in the linear regime. Also the system contains materials and we cannot model the molecular

resonance to the THz. Instead, two different experiments have been compared in this chapter.

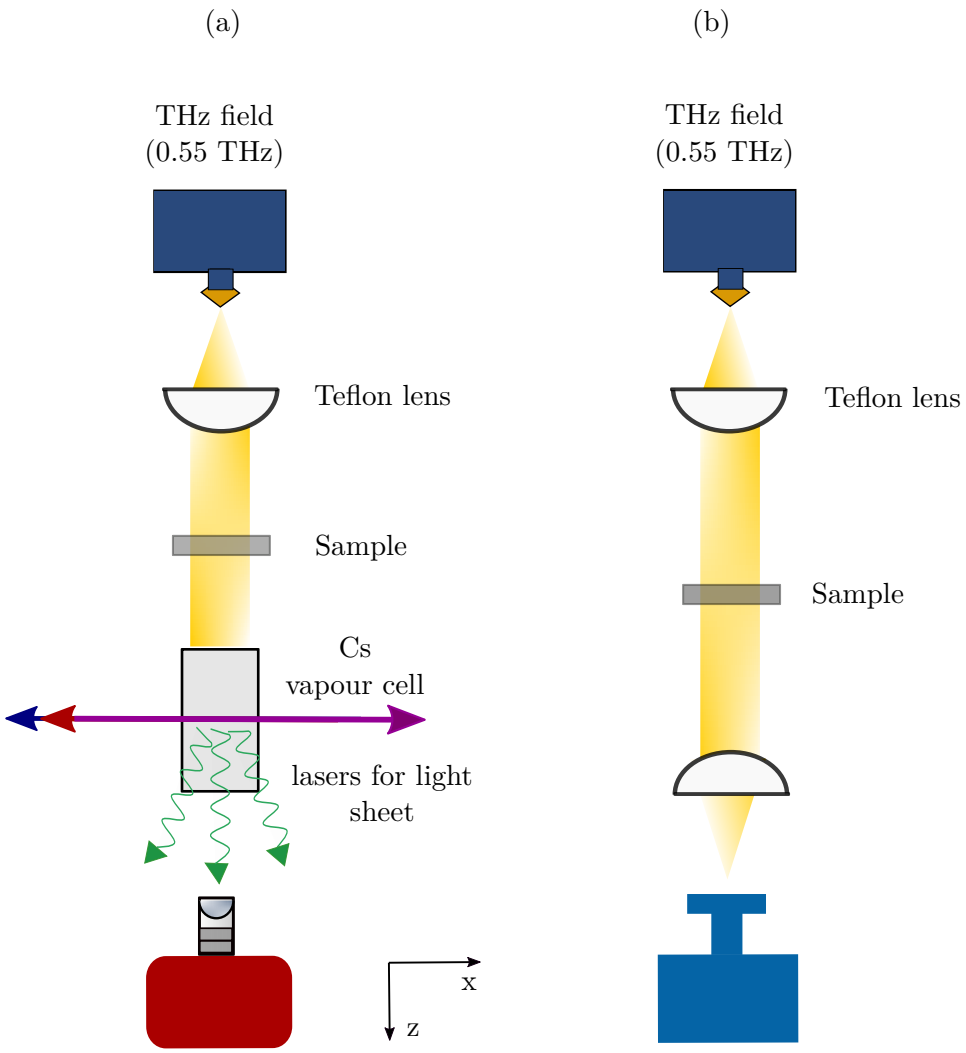

Figure 4.3: **Experimental layout:** (a) Experimental layout used in the atomic detection experiment: The THz field propagates perpendicularly to the IR laser beams and is collimated using a Teflon lens, and the sample is laid between the Teflon lens and the cell. Three lasers are used to form the light sheet at the centre of the vapour cell, an optical camera is placed to measure the intensity of the fluorescence that is emitted from the cell. (b) Experimental layout used in the THz power meter experiment. The field is collimated using a Teflon lens and is focused on the power meter using the second Teflon lens. The sample is placed between the two Teflon lenses. The power meter replaces the vapour cell and optical camera.

4.4.1 Atomic Detection Method

This experiment was performed in transmission geometry, as we outlined in Chapter 3. The schematic layout of materials analysis using the atomic detection method is shown in Fig.4.3(a). This uses three commercial IR lasers, the probe laser (6.5 mW at 852 nm), the coupling laser (13 mW at 1470 nm) and the Rydberg laser (62 mW at 843 nm), these three lasers are stabilised as explained in Chapter 3. The majority of light from these lasers is sent into the vapour cell to create a 2D light sheet.

The continuous-wave THz field propagates in the z axis perpendicular to the lasers for the light sheet and the field is generated using the THz source A, described in Chapter 3 at 0.55 THz. The sample of thickness, l, is placed in the imaging plane, and the collimated THz field passes through the sample with the incident intensity I_0, this intensity interacts with the sample, and some of it will be absorbed, and then the transmitted intensity I will be directed towards the vapour cell and detected by the atomic detection light sheet. The reflection from the surfaces is neglected.

The transmitted THz will interact with the vapour to create green fluorescence which can be imaged in a single shot by placing an optical camera on the opposite side of the incident THz field. The transmitted intensity is then calculated by averaging over the region of interest of the image pixels, as shown in the figure later in Section 4.5.

Six different sample polymers have been investigated in this study, Nylon6, Teflon, polyvinyl chloride (PVC), high-density polyethylene (HDPE), polypropylene and Tufnol. The samples were formed into disks with a diameter of 76 mm. For each polymer, first, a measurement without any polymer material was recorded to give a measurement of the incident intensity, I_0. Each material was tested using different thicknesses that increased gradually, and for each thickness, we obtained an image with the THz off and then with the THz field on, and the measurements

for fluorescence signal, F' and F were recorded. As described in Chapter 3, our experiment works in a low power THz regime—the fluorescence signal F is obtained when the THz is on by setting the UCA voltage to the appropriate value between (2.6 V - 2.74 V), which lies in the low power regime region but is still sufficient to perform the experiment.

4.4.2 THz Power Meter Method

The experimental set-up for materials analysis using the THz power meter method is shown in Fig.4.3(b). This approach is based on measuring the power of the THz radiation transmitted through the polymer materials. The THz source A that was used in the atomic detection experiment was also used in this experiment. The diverging THz beam is launched into free space from a diagonal horn antenna; it is collimated using a Teflon lens and focused on the THz power meter with a second Teflon lens. The sample is placed between these two Teflon lenses and in the opposite direction of the incident THz field a commercial thermal THz power meter (VDI Erickson, PM5) is used to detect the transmitted THz power. This THz power meter is highly sensitive to any change in temperature, it has a minimum detectable power of 1 μW and a response time between (0.15 s - 12 s) depending on the input power, with 90% of the response [160].

The two Teflon lenses enable coupling of $P_0 = 0.70 \pm 0.01$ mW of power into the THz power meter, which was used to conduct the measurements. This experiment was performed at room temperature, and as the THz power meter is very sensitive to the temperature, the power measured by the power meter drifted by 0.01 mW. Due to the slow response time of the power meter it was necessary to wait around 15s between each measurement to allow the THz power meter to reach a stable state. The reason to wait 15 s, because the response rate of the thermal power meter is limited only reach 90% of the response after 12 s [160], so for each measurement, we allow it to stabilise for 15 s to ensure we capture 100% of the accurate signal.

The same polymer materials with the same thicknesses were used as were used in the atomic detection method. For each thickness, the transmitted THz power was recorded P. A background reading P_{bgd} was then taken with the THz source turned off. This was subtracted from the reading P. Five measurements were taken for each sample thickness, and the results were analysed and compared with the previous method.

4.5 Measurement and Results

Six different polymer materials were examined at 0.55 THz using two complementary experimental methods. For the atomic detection method, the fluorescence intensity emitted from the vapour cell decreases with increasing the polymer thickness. Fig.4.4(a) shows the images for the THz transmission that are extracted from the raw data for PVC material using Eq.4.12. The image on the left of the figure represents the maximum intensity without any material I_0, and the image on the right represents the maximum attenuated intensity by this polymer. Those images in between show increasing signal attenuation.

The measured data for the PVC material was plotted as shown in Fig.4.4(b); each data point represents the average intensity of the fluorescence for the images that are illustrated in Fig.4.4(a) normalised to the maximum average intensity against the thickness. It is possible to see that the average intensity of the fluorescence decreases exponentially with increasing thickness according to the Beer-Lambert law in Eq.4.1. All polymer materials used in this work display very similar behaviour.

Using Eq.4.1 allows us to plot $\ln(I_0/I)$ against the thickness and then calculate the absorption coefficients α of the polymer samples via a straight line fit.

Fig.4.5 shows a plot of $\ln(I_0/I)$ against the thickness l for Teflon Fig.4.5(a) and Nylon6 Fig.4.5(b), used to calculate the absorption coefficient (gradient). The atomic detection method is indicated by red dots, and the THz power meter method

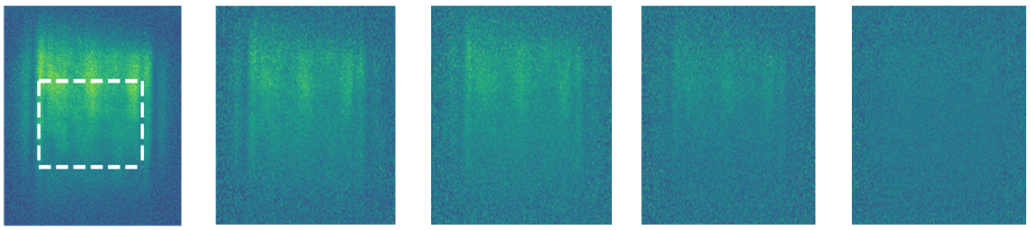

(a)

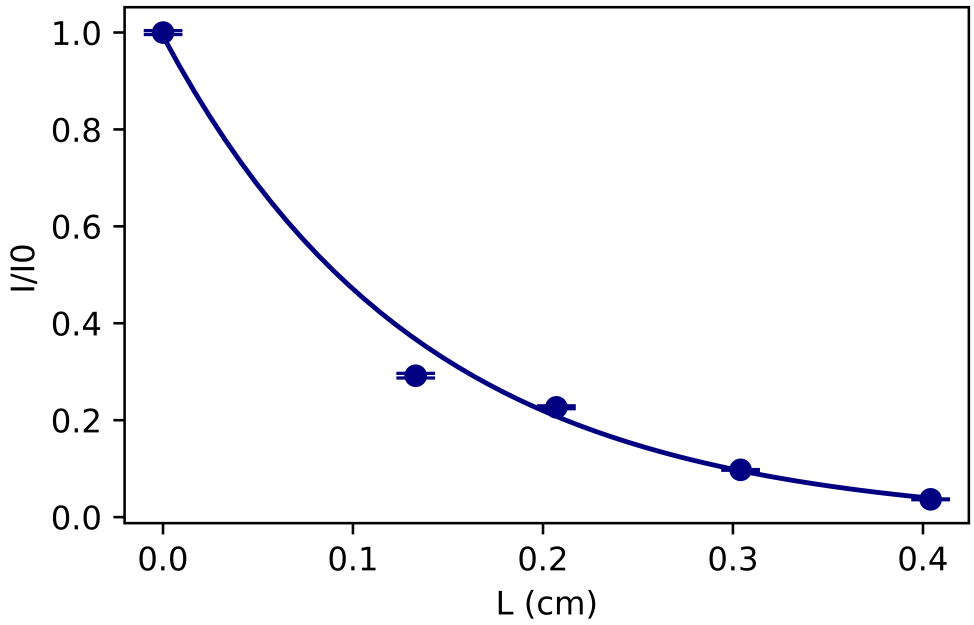

(b)

Figure 4.4: **The measured data for PVC polymer material using the atomic detection method:** (a) The THz transmission images for PVC materials that are extracted from the raw data using Eq.4.12, which shows the fluorescence intensity, allows the observer to see how the fluorescence decreases with increasing the thickness from left to right, the highlighted white dashed line is the region of interest over which the pixels are averaged. (b) The average intensity of the fluorescence from the images in (a) normalised to the maximum average intensity with varying thicknesses, which decreases exponentially with increasing the thickness. The exponential is the guide to the eye and not fit to the data. The errorbars are the statistical deviation of five measurements.

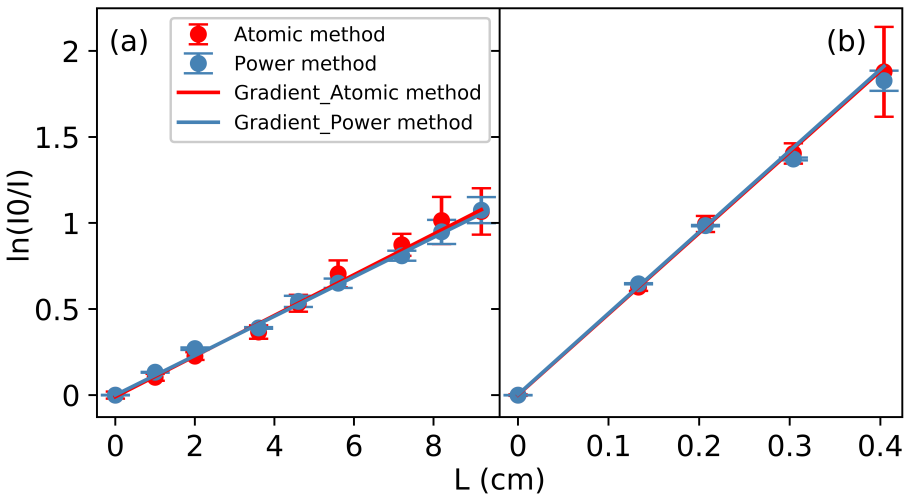

Figure 4.5: **The absorption coefficients of Teflon and Nylon6 materials:** (a) and (b) The absorption coefficients (gradients) of Teflon and Nylon6 materials, respectively, were obtained using the atomic method and THz power meter method showing how the plots are perfectly aligned on top of each other. For Teflon the gradient is (0.151 ± 0.007) cm^{-1} by using the atomic method and (0.147 ± 0.001) cm^{-1} by using the THz power meter method, where for Nylon6 the gradient is (7.5 ± 0.2) cm^{-1} by using the atomic method and (7.56 ± 0.02) cm^{-1} by using the THz power meter method. The slope changes depending on the absorption of THz radiation, which is lower for the highly-transparent material (Teflon) than the opaque material (Nylon6). The error bars are the statistical deviation of five measurements.

by blue dots. The gradient of the plot according to the THz power meter method is the same within error as the gradient of the atomic detection method.

We can see how the gradient changes between the two materials—it is higher in the material which is more opaque to the THz radiation (Nylon6) with gradient of (7.5 ± 0.2) cm^{-1} using the atomic method and (7.56 ± 0.02) cm^{-1} using the THz power meter method, than the more transparent material (Teflon) with gradient of (0.151 ± 0.007) cm^{-1} using the atomic method and (0.147 ± 0.001) cm^{-1} using the THz power meter method. The experimental error (as represented by the error bars in Fig.4.5) is derived from the statistical deviation of five measurements. To determine the absorption coefficients of the samples, they were obtained from the weighted linear best fits of the measured data.

The absorption coefficients of the measured samples are summarised in Table 4.1 and compared with the literature. In Table 4.1 we compared the measured absorption coefficients of the six polymer materials from the atomic detection method with the THz power meter method, and we can see they were in good agreement. The measured α value from the Teflon material was similar to that reported by [142] in the literature. However, the measured values for Nylon6, PVC, polypropylene and HDPE were somewhat greater than reported in the literature, maybe due to our measurements not including the reflection from the surfaces which are $\approx 2\%$ for Teflon [142] and $\approx 5\%$ for the PVC [126]. We see the three polymers, polypropylene, Teflon and HDPE, are highly transparent to THz radiation at 0.55 THz, whilst the other three polymers, Nylon6, PVC and Tufnol, are opaque to THz radiation at this frequency.

However, the uncertainty is lower in the THz power meter method than in the atomic detection method. Also, it is possible to see that the opaque materials have greater levels of uncertainty than the transparent materials. This could be because the low visibility of THz radiation reduced the range of available thicknesses, thereby reducing the accuracy of the analysis. Furthermore, the reduced signal amplitude measured in the more highly attenuating materials leads to a reduction in the signal-to-noise ratio.

In the absorption coefficient measurements, the polymer samples were all taken from the same manufactured batch. We found that they give different results when they should be identical. We suggest this could be because of the polymer chain direction or the strain history of the polymer. These reasons are speculative, without substantial evidence, but offer a reasonable conjecture. We would like to undertake further controlled measurements on the mechanical effects on absorption in the polymer materials that were used in the material analysis experiment. Where the optical proprieties of these polymer materials depend on their strain history, how such materials have been stored, how they have been machined, and even how they have been manufactured could influence the measurement [161].

The magnitude of the power used when the THz power meter method was performed-0.70 mW, was higher than the power used when the atomic detection measurements were conducted, (about 200 μW - $>$ 5 μW). Even under the perfect conditions the minimum detectable power of the power meter is (1 μW) [160], where our atomic method the minimum detectable power is (190 ± 30) fW $s^{-1/2}$ per $(40 \times 40)\mu m^2$ pixel [73]. This means the minimum detectable power in the power meter is much larger than the minimum detectable power in the atomic method. Therefore, our atomic detection method could be used with weaker THz sources or more strongly absorbing materials. In terms of time, with the power meter method, the THz source needed to remain on for a long time (15 s) until the reading became steady. For the atomic method, we simply took a 200 ms exposure.

Sample	$\alpha(\mathrm{cm}^{-1})$ Atomic detection method	Percentage error(%)	$\alpha(\mathrm{cm}^{-1})$ THz power meter method	Percentage error (%)	Published Values and Sources
Nylon6	7.5 ± 0.2	2.7	7.56 ± 0.02	0.3	7 [143], 6.5 [126]
PVC	7.8 ± 0.3	3.8	8.04 ± 0.14	1.7	6 [126]
Polypropylene	0.282 ± 0.004	1.4	0.281 ± 0.002	0.7	0.23 [162], 1.15 [143]
Teflon	0.151 ± 0.007	4.6	0.147 ± 0.001	0.7	0.15 [142], 0.13 [162], 1.3 [143]
HDPE	0.36 ± 0.01	2.8	0.373 ± 0.002	0.5	0.2 [142], 2.2 [143]
Tufnol	12.4 ± 0.3	2.4	12.07± 0.08	0.7	

Table 4.1: Comparison of the absorption coefficients from six different polymer materials via the atomic detection method against a THz power meter method and values reported in the literature.

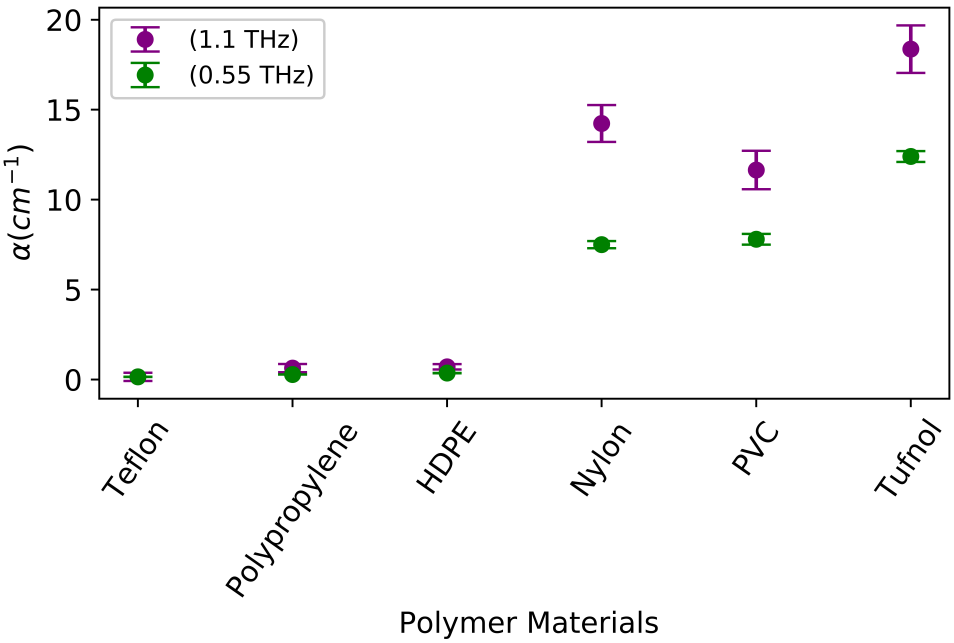

Figure 4.6: **Comparison of the absorption coefficient of six polymer materials:** All the polymer materials that we tested are more absorbing at 1.1 THz frequency (purple dots) than 0.55 THz frequency (green dots), with the exception of Teflon, which had the same absorption at 1.1 THz and 0.55 THz.

4.6 Comparison of the Absorption Coefficient of the Polymer Materials at 0.55 THz and 1.1 THz

This experiment was performed using the experimental set-up for the atomic detection method in Fig.4.3(a). To conduct the measurements at 1.1 THz, it was necessary to change the imaging transition from $14P_{3/2} \rightarrow 13D_{5/2}$, to $12P_{3/2} \rightarrow 11D_{5/2}$ at 1.1 THz and replace the Rydberg laser as has been outlined in Chapter 3. This experiment was conducted using THz source B. The filter for the optical camera had to be changed to accommodate the different wavelengths of output fluorescence. All of the other methods are kept the same such as the data analysis etc.

Most of the polymer materials are much more absorptive at 1.1 THz than at 0.55 THz [142, 152]. Because of this, gathering enough data points to fit a gradient and extract an absorption coefficient at 1.1 THz was difficult. Therefore, in this

study, we investigated the absorption coefficient of our six polymer materials at 1.1 THz frequency using only the thinnest sample from the material set. We use thicknesses of 0.13 cm for the Nylon6, 0.15 cm for the PVC, 0.4 cm for the polypropylene and the HDPE, 1.25 cm for the Teflon and 0.11 cm for the Tufnol. The absorption coefficient of these materials are calculated using Beer–Lambert Law in Eq.4.1 and compared with the results that were obtained at 0.55 THz in Table 4.1. The comparison of the absorption coefficient for the six materials at our two THz frequencies is shown in Fig.4.6. We can see the materials are more absorbing at 1.1 THz (purple dots) than they are at 0.55 THz (green dots). Except for Teflon, which has the same absorption coefficient at 0.55 THz and 1.1 THz. From Table 4.2, the Teflon transmits 83% from the incident THz wave at a 1.1 THz frequency and has the lowest transmission difference between the two THz frequencies, which is 2% , whereas the Nylon6 absorbs most of the incident THz wave and transmits only 16% at 1.1 THz frequency. It also has the highest difference in transmission between 0.55 THz and 1.1 THz frequencies - 21% . This result for Nylon6 will be significant in Chapter 5. The PVC, polypropylene and Tufnol materials have the same transmission difference between the two THz frequencies of 12% . However, the HDPE has a lower transmission than them both by 2% . The absorption coefficient and the differences in the transmission of these material samples at 0.55 THz and 1.1 THz are summarised in Table 4.2. These results are consistent with the literature that says most the materials are more absorbing at 1.1 THz than 0.55 THz [142, 152].

Sample	Thickness l (cm)	Transmission at 0.55 THz $(I/I_0)\%$	$\alpha(\text{cm}^{-1})$ at 0.55 THz	Transmission at 1.1 THz $(I/I_0)\%$	$\alpha(\text{cm}^{-1})$ at 1.1 THz*
Nylon6	0.13	37	7.5 ± 0.2	16	14.23 ± 1.02
PVC	0.15	29	7.8 ± 0.3	17	11.64 ± 1.07
Polypropylene	0.4	89	0.282 ± 0.004	77	0.64 ± 0.23
Teflon	1.25	85	0.151 ± 0.007	83	0.151 ± 0.200
HDPE	0.4	85	0.36 ± 0.01	75	0.71± 0.15
Tufnol	0.11	25	12.4 ± 0.3	13	18.34 ± 1.32

Table 4.2: Comparisons of the absorption coefficient and the difference in transmission of thin polymer samples at 0.55 THz and 1.1 THz.
* The errors are propagated through Eq.4.1.

4.7 Conclusions

The absorption coefficient of various polymer materials at 0.55 THz have been measured. We described a method with a new THz detector to test the polymer materials based on caesium atom using the Beer–Lambert Law for the absorption coefficient and calibrated our imaging system to detect THz intensity. Due to the sensitivity of THz atomic detection to any variation in the system, we used a commercial thermal THz power meter as a comparison experiment, and both results are in good agreement. The atomic method used less THz power than the power meter method, and the reflection losses from the surfaces are neglected in this analysis. We measured the absorption of the thinnest sample from each of the six polymer materials at 1.1 THz and compared them with their absorption at 0.55 THz. From this result, we have chosen the polymer materials to make our sample that will be imaged at two different THz frequencies in Chapter 5.

Chapter 5

Applications of Atom-based THz Imaging

In this chapter, we demonstrate the effectiveness of our THz imaging technique that is outlined in Chapter 3. Using our system, which is based on caesium Rydberg atoms, we conduct experiments that show how our system can be useful in real world applications. These experiments focus on non-destructive testing (NDT) of electronic components and on progress towards fingerprint detection for security applications. We also display an imaging sample containing two different polymer materials at two different frequencies. We calculate the spatial resolution of the system for 0.55 THz and 1.1 THz.

5.1 Introduction

THz imaging systems are being developed across multiple sectors, including manufacturing [3, 1] and biological [20] and medical [4] fields. The most distinctive characteristic of THz radiation is its ability to penetrate through various types of dielectric materials, such as packaging, textiles, paper and plastics—which are optically opaque and prohibit optical imaging [36]. While THz radiation is similar to microwaves in this particular property, the wavelength of THz waves is much

shorter, which allows for a much higher spatial resolution [163]. THz radiation is also relatively safe, due to its low photon energy, making it non-ionising. This enables THz systems to be applied in different fields without the need for the stringent safety protocols that are inherent to other applications of radiation technologies, such as with X-rays in diagnostic medicine [164]. Furthermore, the capabilities of a THz system make it an effective tool to be used in non-destructive testing (NDT) [165, 166, 167], a common approach to characterise the internal structure of objects without destroying them. For example, for safety in construction engineering, THz can be used to detect cracks in cement-based materials [168], defects in foam materials [169], in authentication [170], detection of debonding defects in ceramic matrix composites (CMC) [171] and defect detection in encapsulated devices such as semiconducting chips [172, 173, 174]. Through the development of THz systems, the quality and performance of high-voltage cables also can be tested [175].

One crucial aspect of THz radiation is that water and other polar liquids strongly attenuate THz radiation [20, 176]. This effect is due to the hydrogen bonds between the water molecules that resonate strongly at THz frequencies and absorb the majority of any incident THz radiation. This has been utilised in in-vivo THz measurements of human skin, which can only be conducted in reflection mode owing to the high signal attenuation in the THz frequency range caused by water within the tissue [177, 178].

5.2 Towards Fingerprint Detection Using THz Imaging

Since the early days of policing and crime detection, the fingerprint has been recognised as a unique and secure biometric trait. It has been considered the most efficient method for biometric authentication [179]. Over several decades, much research has been conducted on fingerprint recognition [180]. This research has been widely applied for a variety of purposes, such as in the investigation of

forensic evidence, inspection of national border crossings and financial markets [181, 182, 183, 184]. Nowadays, fingerprint recognition systems are applied in different fields, such as in the mobile market [185] and companies, to monitor employee working hours. Recently, several studies have been undertaken to investigate how THz radiation interacts with the complex structure of human skin. However, fingerprint detection in the THz spectral region has not yet been explored extensively [186, 187]. Due to THz radiation being highly attenuated by water, it is not possible to perform THz in vivo fingerprint imaging experiments in the transmission configuration (as has been more fully explained in Chapter 3) where, in the lower frequencies of the THz band, radiation penetration of living human skin is limited to a few hundred microns depending on the THz frequency [188, 189]. Thus, to date, in vivo THz imaging experiments on humans have always been performed in a reflection geometry [190, 191, 192, 177].

The experiments presented in this work were conducted in a similar reflection configuration. The schematic for detecting a finger is shown in Fig. 5.1. THz source C at 0.55 THz frequency has been used in this experiment. The THz beam propagates from the horn and is collimated using a Teflon lens. A gold plane mirror is placed on the opposite side of the THz source at an angle causing the THz beam to be reflected and hit the object surface at an angle at the imaging plane. We use a 7 mm thick Teflon plate as a window to place a finger behind. Teflon is used as it is highly transparent at THz frequencies as seen in the previous chapter. The diffuse scattering of the THz field from the finger's surface is focused by the imaging system and imaged upon the vapour cell. The optical fluorescence from the vapour cell is re-imaged by an optical camera that is placed on the opposite side to the incident THz field. In this configuration, without finger present we can still see the specular reflection of THz from the front and back surfaces of the Teflon plate, which can be seen in Fig.5.2(a). By pressing the finger on the back of the Teflon, we can see the reflection of the shape of the finger from the back of the Teflon plate, as shown in Fig.5.2(b).

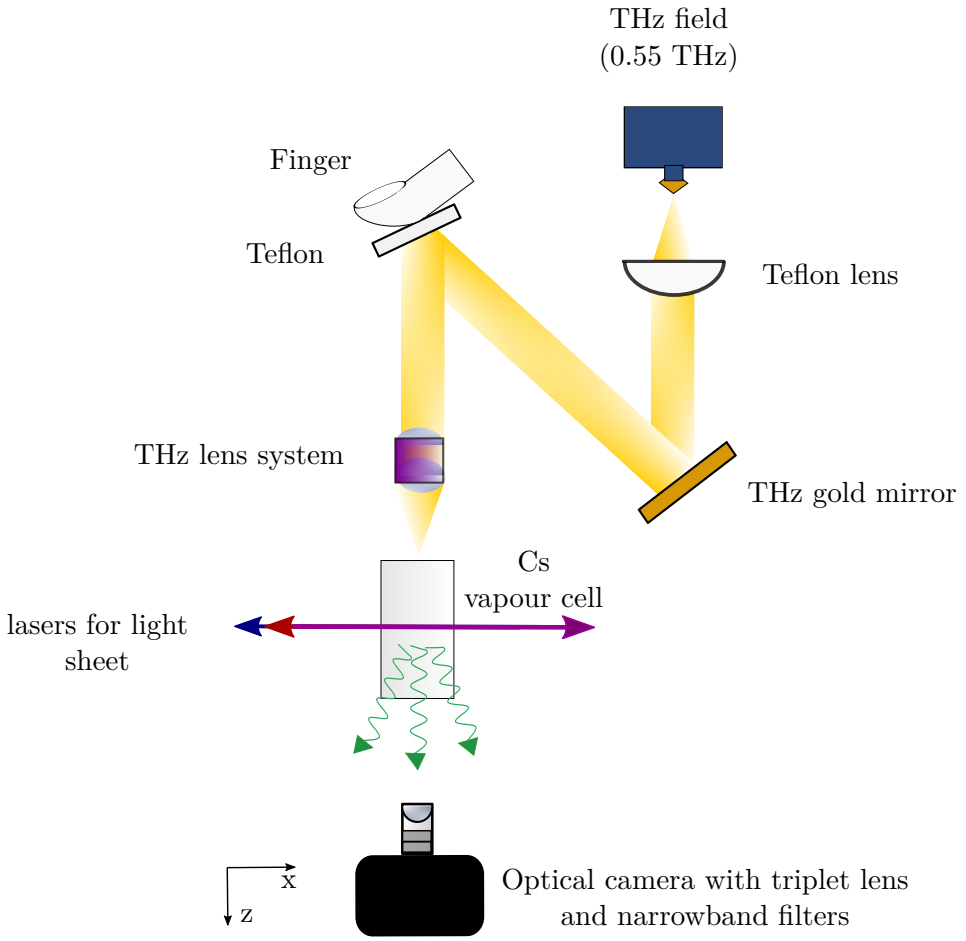

Figure 5.1: **Experimental set-up for reflection mode imaging:** By collimating the THz field with a Teflon lens and reflecting it with a gold plane mirror as THz radiation is reflected by the metal, the field will be incident at an angle on the target object. The imaging system will image the diffuse scatter from the object onto the atomic vapour cell. The optical camera is placed on the opposite side where the THz field is incident and captures the fluorescence from the vapour cell.

The alignment of reflection mode is more challenging than that for transmission mode since it requires the THz field to be reflected at the imaging plane. Another disadvantage of this mode is that it required a lot of power; this is because most of the THz power is lost through scattering effects before the field is able to interact with the atomic vapour.

Although our imaging system cannot detect the fingerprints, it can image the human skin behind THz transparent materials.

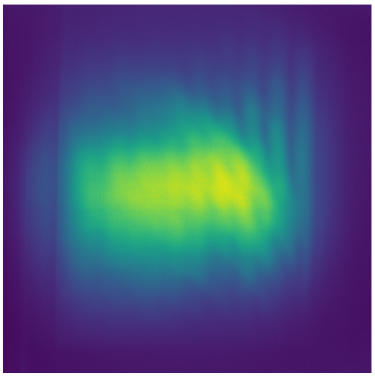

(a)

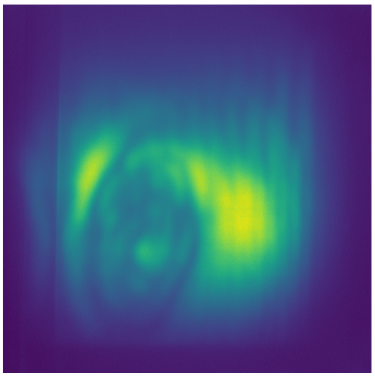

(b)

Figure 5.2: **Imaging a finger in reflection mode:**(a) The scattering of the THz radiation from the surface of Teflon. (b) The image of a finger that is placed behind the piece of Teflon.

5.3 Spatial Resolution

The spatial resolution of the system can be determined by imaging a point source and calculating the system's point spread function (PSF), and that has been done for our system in [73]. In this thesis, for interest, we used the edge method [193, 194] to compare the resolution with the previous result. With this method, we block half of the THz beam by placing a sheet of metal in the imaging plane. In this case, instead of seeing a reasonably even fluorescence on our light sheet detector in the

vapour cell, we see a very dark form on one side and then bright on the other side; this is shown in Fig.5.3(a), at 0.55 THz on the left and 1.1 THz on the right. We can observe that the blocked half for 1.1 THz is darker than that for 0.55 THz due to the Rydberg fluorescence (background) being brighter in the 0.55 THz frequency transition than in the 1.1 THz transition.

In order to calculate the spatial resolution it is necessary to convert the 2D array of images in Fig.5.3(a) into a 1D array by performing column integration against x. This is essentially a sum of all the pixel values in the y axis ($\sum(N_y)$) where N_y is the pixel numbers in all rows for y axis. This integration gives the edge of the image, as shown in Fig.5.3(b) for both frequencies. Instead of plotting the actual sum of y axis pixel values, we plot the differential of these pixel numbers with respect to the position ($\mathrm{d}\sum(N_y)/\mathrm{dx}$) against x. This step results in no change in the blocked region, but we can see that it is not perfect since some fringes may be observed. There next begins to be a rapid change, which is a perfect peak in theory, but in reality this is a slope, which, when differentiated, becomes a peak, as shown in Fig.5.3(c) for both frequencies. We can calculate the width of this peak to determine the resolution in pixels, which can then be converted into millimetres.

5.3.1 Calculating the Peak Width

Knowing the width of the vapour cell effectively allows us to calculate the width of the peak through the magnification provided by the optical system (M2), as shown in Fig.5.4. This system includes the triplet camera lens that is discussed in Chapter 3. From our data, the width of the image is 740 pixels which corresponds to a width of the vapour cell of 10 mm; hence,

$$1 \text{ Pixel} = \frac{\text{cell size}}{N} = 0.0135 \text{ mm}. \tag{5.1}$$

Eq.5.1 will be referred to as the 'converter', where N is the number of pixels between the edges of the cell. The pixel size of the camera that we used (an Andor iXon

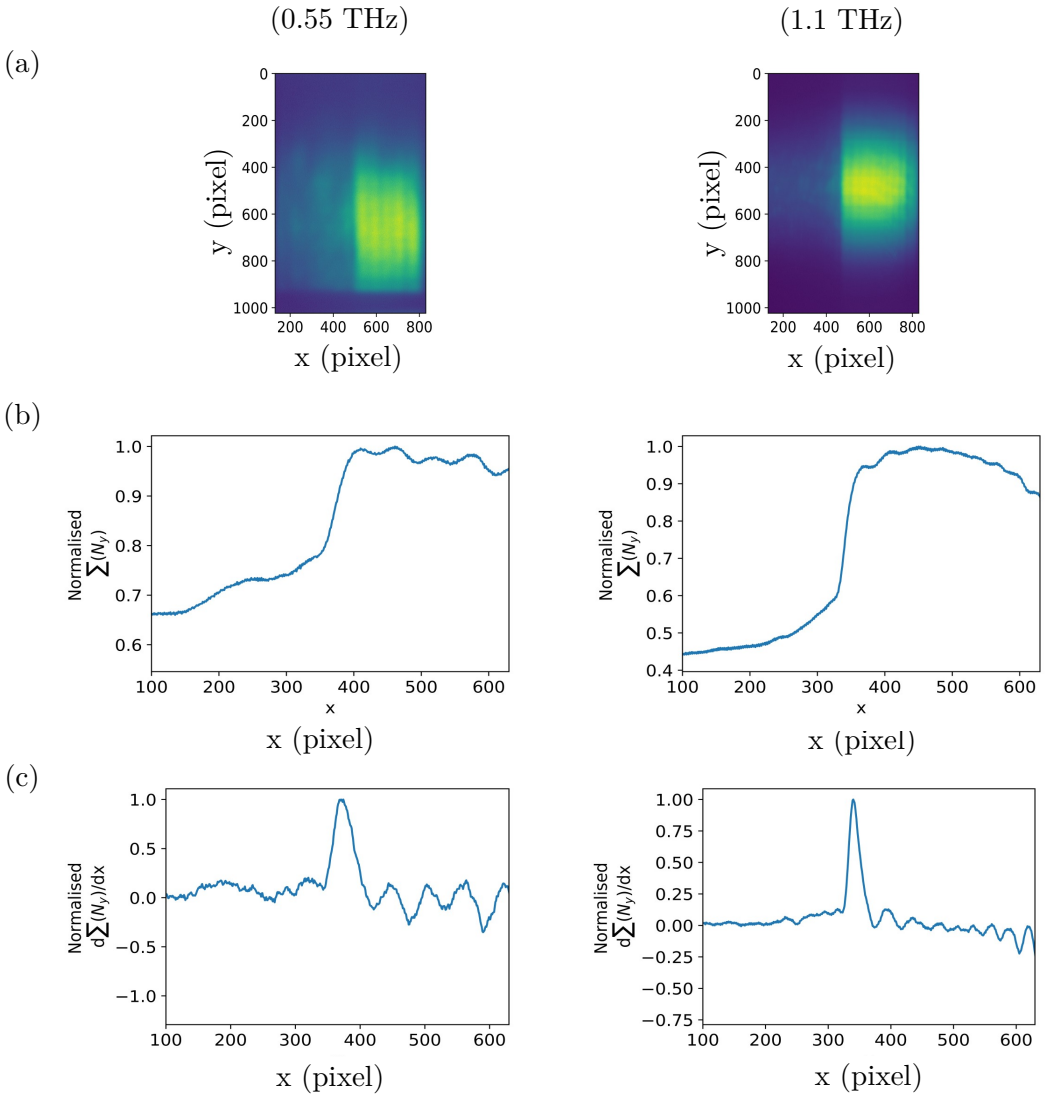

Figure 5.3: **Spatial resolution measurements for 0.55 THz (left) and 1.1 THz (right):** (a) The images formed by blocking half of THz beam using a metal set square tool. (b) The plots of the normalised data to the maximum value sum over all the pixel values in y axis ($\sum(N_y)$) against x for both frequencies. (c) The plots of normalised data differentiate the sum over all the pixel values in y axis ($d\sum(N_y)/dx$) with respect to x against x for both frequencies.

EMCCD) is 13 μm, and that confirms what we discussed in Chapter 3 about the triplet camera lens being designed to have almost 1:1 magnification. Therefore, by using this converter and calculating the width in pixels, we can determine the width in mm.

It is necessary to calculate the peak full width half maximum (FWHM) for Fig.5.3(c), but the obtained data are relatively noisy on the right side. It is necessary to work out the averages of the profile wings to obtain a baseline, but these wings are not at the same level, therefore we have taken the average of the left wing for both peaks in Fig.5.3(c). By adding the baselines, we can take the FWHM, which is the width in pixels. We can then use the pixel size converter to determine the FWHM measurements in mm.

Two different THz sources have been used in the imaging experiments, so we need to calculate the width for both lineshapes that we obtained by pixel then convert them to mm.

The FWHM between the peak and the baseline using 0.55 THz is (31 $\pm$ 3) pixels, by using Eq.5.1 we can write the width of the lineshape in mm as

$$\text{Width}_{(0.55)} = \text{FWHM}_{(0.55)} \times \text{converter} = 0.42 \pm 0.04 \text{ mm}. \tag{5.2}$$

The FWHM by using 1.1 THz is (22 $\pm$ 3) pixels, we can convert the width of the lineshape as a result of using this source to mm, by using Eq.5.1:

$$\text{Width}_{(1.1)} = \text{FWHM}_{(1.1)} \times \text{converter} = 0.29 \pm 0.04 \text{ mm}. \tag{5.3}$$

The lineshape for 1.1 THz frequency is higher and narrower than that for 0.55 THz frequency due to its shorter wavelength. We seen improvement in resolution because the diffraction limit has reduced to half, but we might have needed our THz lens to be bigger to catch all the light.

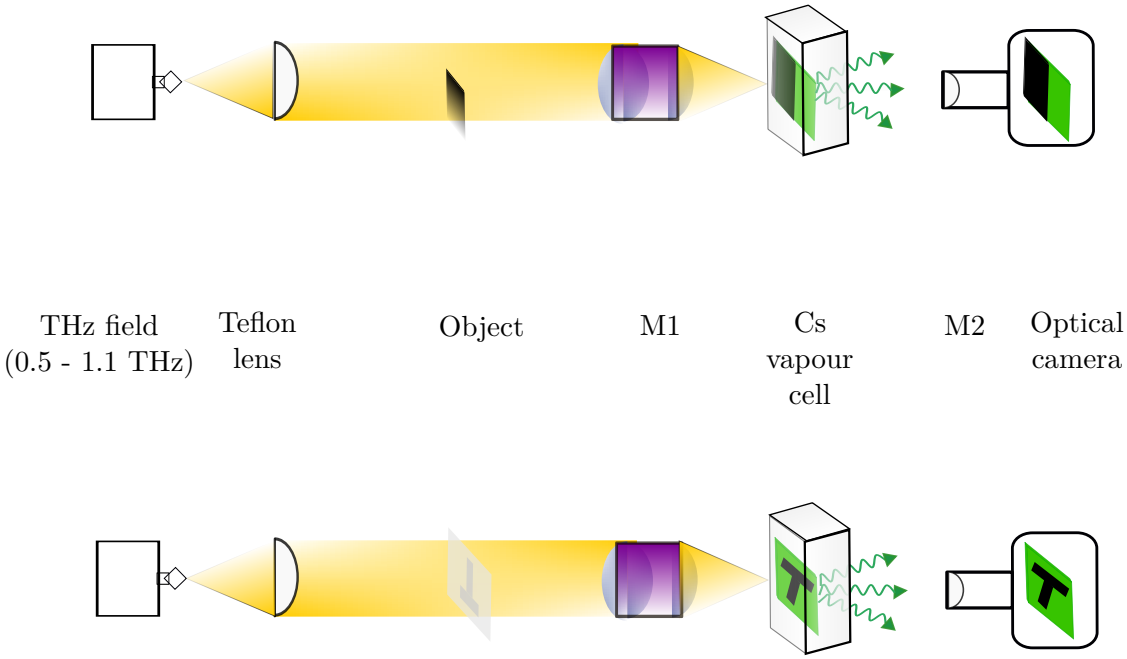

Figure 5.4: **The calibration of the spatial resolution experiment set-up with the imaging letter "T" sample experiment that has the same set-up:** We used a THz field source and Teflon lens to collimate the beam during both experiments. After the beam is collimated, the object in the top figure, which is sheet of metal, is placed in the imaging plane and block half of the beam. The object in the low figure, which is the letter "T" sample is placed in the imaging plane. both objects are imaged by the optical system (M1) on the light sheet detector in the vapour cell. The objects will be re-imaged in the optical camera using the second optical system (M2).

Our previous calculations of the width using the FWHM have been done based on the magnification of the camera lens M2, by knowing the width size of the vapour cell. However, there is another magnification in the system M1 that should be taken into account. Our spatial resolution of the system can be described as

$$\text{Spatial resolution} = \frac{\text{Width}}{\text{M1}} \tag{5.4}$$

To calculate the magnification factor M1, we must determine the size of the object and corresponding image produced by the system. Fig.5.4 shows the calibration of the spatial resolution experiment set-up with the experiment which has the same set-up; the imaging letter "T" sample experiment. Through the calibration we calculate the magnification factor M1 to be 0.54 ± 0.02 at 0.55 THz and 0.50 ± 0.02

at 1.1 THz. We would not normally expect the magnification between 0.55 THz and 1.1 THz to differ significantly. However, the difference shown maybe due to the misplacement of the lens, where the magnification would change depending on the lens distance from the cell. This is the conversion factor that we used to calculate the spatial resolution, for more details see Appendix A.

Therefore, the spatial resolution can be obtained by substituting the magnification factor M1 and the width from Eq.5.2 for 0.55 THz, and Eq.5.3 for 1.1 THz into Eq.5.4. Thus, using this simple edge method, we can find the spatial resolution of 0.78 ± 0.07 mm at 0.55 THz and 0.58 ± 0.08 mm at 1.1 THz. The spatial resolution that we calculated for 0.55 THz is smaller than the one in [73], because we used a better lens M1 in this work.

5.4 Comparison of THz Imaging and Optical Imaging of Electronic Components

THz imaging is a powerful tool that can be used for measuring the properties of particular materials, for example inspecting layers and viewing packaged products with transmission imaging [195, 34]. The ability of THz waves to penetrate many non-conductive materials makes them an up-and-coming inspection tool for non-destructive testing (NDT) [196, 197, 167]. This is a critical measurement technique that is used in many manufacturing processes. It offers a convenient inspection method for product quality control and process monitoring to determine the extent of damage and irregularities in materials without causing damage to the original component. THz technology can be considered an effective technique for non-destructive testing in industrial inspection and include examination and detection of defects in the internal structures of the small electronic components such as integrated circuit (IC) [172]. In non-contact inspection, although optical techniques currently dominate the field, inspections are limited to materials that are transparent to visible or near-infrared light. Devices and tools that make use

of THz radiation could offer the potential to inspect items normally beyond the reach of optical techniques [198]. Most of the optically opaque materials possess good or moderate transparency at the THz frequency range [199, 200], making THz radiation an ideal choice for NDT and non-contact applications.

Identifying counterfeit electronic components is one of the current challenges in the electronic component market because counterfeit components may cause serious problems which affect the brand reputation and bring the prices of the electronics components down [201]. THz techniques can readily discern the differences between authentic and counterfeit electronic parts [172, 170]. Since counterfeiters derive such high gains from their products, these products undergo constant refinement, which makes it increasingly difficult to distinguish authentic components from counterfeit examples. There has been increased attention in the detection of the integrated circuit chip package defects of the electronic components using the traditional methods [202, 203]. However, these traditional methods are dependent on scanning electron microscopy techniques, which requires time to undertake and analyse the collected data. While an electronic device is being packaged and used, damage and defects could occur to the internal structure [204]. Deformation, cracks, warpage, delamination, and voids can be found within their packaging materials. The accumulation of these defects over time leads to the failure of the device or even complete destruction—with potential catastrophic consequences—making industrial inspection a critical process. In order to detect these defects, THz imaging has become one of the principal approaches [174]. Whereas X-ray can penetrate through an integrated circuit packages, the defects cannot be detected at these frequencies [205]. A few studies have been carried out to image integrated circuit chip package, and the imaging results are undergoing resolution enhancement techniques [172, 206]. Our imaging system can image the internal structure of the electronic components and show if there are any difference between them within the 200 ms exposure time.

The practical example of seeing through an electronic component package is shown

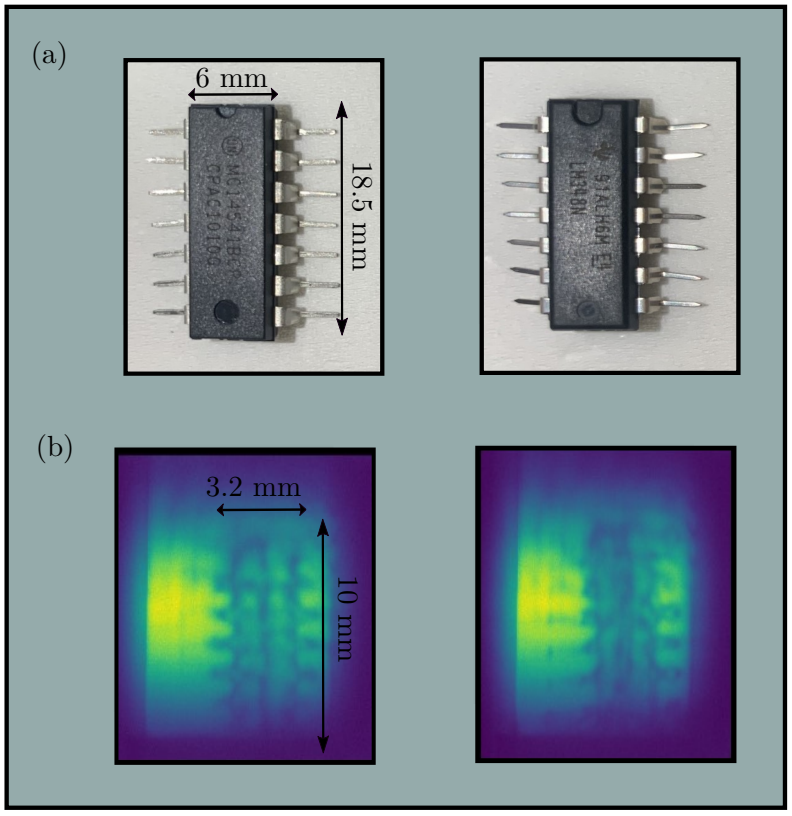

Figure 5.5: **Comparing two different operational amplifiers in two different imaging systems:** (a) Optical imaging for two different op-amps images shows we cannot see the internal structure. (b) THz imaging for the same op-amps that are displayed in (a), we can see that THz imaging shows the difference in the internal structure.

in Fig.5.5. This experiment used our THz imaging system in transmission mode, as described in Chapter 3. This experiment is performed by using THz source C, at 0.55 THz. Our electronic component object is a commercial operational amplifier (op-amp). Fig.5.5(a) illustrates optical imaging of two op-amps; the one on the left has the production series MC14541BCP and the one on the right has the production series LM348N, both having the same dimensions (1.85 × 0.6) cm. The black plastic packaging material of the op-amp is transparent and has low absorption at 0.55 THz frequency, while the THz field is reflected by the metal of the op-amp, and is partially absorbed by the semiconductors [125]. As a result of these differences in transmittance of the THz radiation, the transmitted THz beam is imaged on the vapour cell, and the images of optical fluorescence are

captured, as shown in Fig.5.5(b). Transmission THz imaging can provide us with more information about the internal structures. It is possible to see the outline of the op-amp, silicon chip and the pins package, as well as the metal connectors that lead to these pins. In the THz images, the image on the left appears different from the one on the right, whereas they look exactly the same by optical imaging. For example, the body of the op-amp on the right appears more opaque at THz frequency than the left, and more internal structure is seen on the left. Although this can also be accomplished with X-ray radiation, THz radiation is non-ionising, and operators are not subject to as many safety hazards.

5.5 Imaging a Sample Containing two Different Polymer Materials at two Different THz Frequencies

From Chapter 4, we have seen that many common materials have different absorption properties between two THz frequencies, such as being almost transparent for 0.55 THz and opaque at 1.1 THz. We want to see the contrast on a sample that contains two polymer materials at two different THz wavelengths. For this purpose, we fabricated a sample from two different polymers. We used a 1 mm thick piece of Polypropylene material as a base, which is highly transparent to THz radiation at 0.55 THz frequency, with absorption coefficient of $\alpha = 0.28$ cm^{-1} as we outlined in Chapter 4. We milled out a section in the shape of the letter "T" and filled this void with a piece of Nylon material that is opaque to THz radiation at 1.1 THz, the optical image of this sample is shown in the centre of the top of Fig.5.6. This sample has a uniform thickness of 1 mm. The dimensions of the Polypropylene material are (5 $\times$ 5) cm, whereas for the letter "T", which is made from Nylon material, are (1 $\times$ 0.9) cm. The dimensions for the letter "T" have been chosen so that the image would fit in the vapour cell.

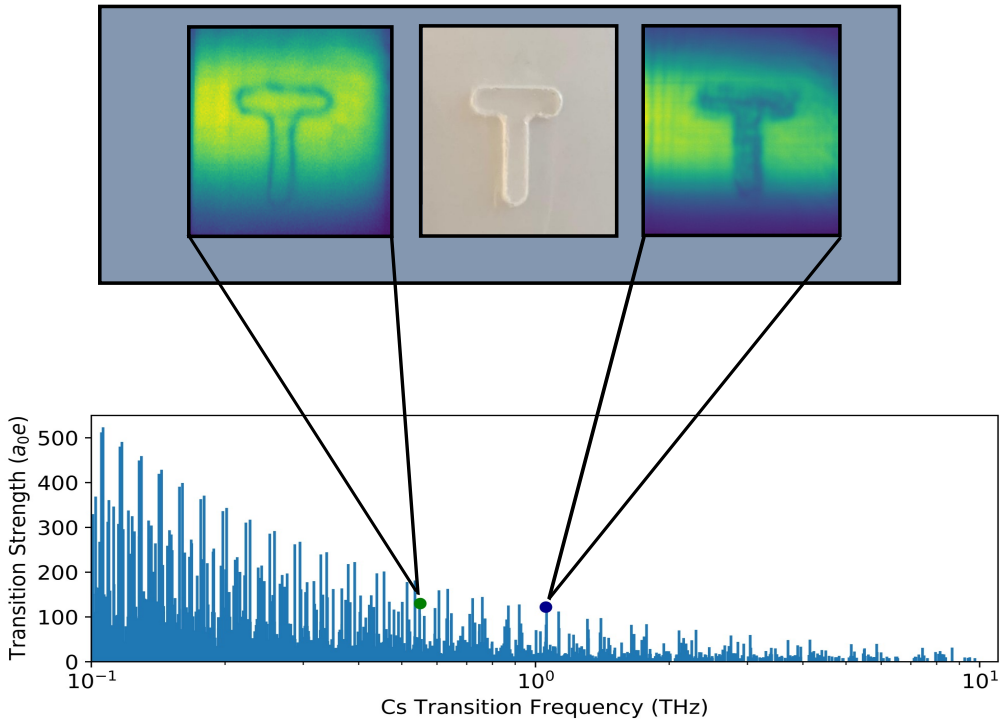

Figure 5.6: **Imaging a mixed-material sample at two different THz frequencies:** The top figure shows in the center the optical image of the sample, which is made from Polypropylene base and the letter "T" is filled in from Nylon material. The image on the left shows the THz image of this sample at 0.55 THz, and the right image shows the THz image of the same sample at 1.1 THz. The lower figure shows resonant transitions between Rydberg states for caesium in the THz frequency range. The transitions that we used for 0.55 THz and 1.1 THz frequencies are indicated with green and blue dots, respectively. The transition frequencies and transition strength were calculated using Alkali Rydberg Calculator in Python (ARC) [207].

We performed this experiment by using the imaging experiment set-up in transmission mode that is described in Chapter 3. The experiment was conducted using two THz sources, THz source C, which has a frequency of 0.55 THz and THz source B, which has a frequency of 1.1 THz. The sample is placed in the imaging plane, which is illuminated by the THz beam after passing a collimating Teflon lens. The transmitted THz beam is then imaged onto the light sheet after being focused by the imaging system. The images can be captured by the optical camera, as shown in Fig.5.6. The top of the figure shows three images of the Polypropylene-nylon sample. The one in the centre is an optical image. The one on the left displays a

THz image of this sample at 0.55 THz, while the one on the right displays the THz image of the same sample at 1.1 THz. The lower figure is the resonant caesium transitions between Rydberg states in the THz frequency band. The two transitions for 0.55 THz and 1.1 THz that are employed in this experiment are calculated from Alkali Rydberg Calculator in Python (ARC) [207], and pointed out as a green dot and a blue dot, respectively.

In the polypropylene-nylon sample we have seen similar transmission levels for both materials at 0.55 THz; however, there is a clear, sharp dark outline as shown in Fig.5.6 (left). While imaging the same sample at 1.1 THz results in different levels of transmission and a very high contrast between the materials, as Polypropylene still transmits THz radiation at 1.1 THz frequency, but Nylon highly absorbs THz radiation at this frequency, and we can see the letter "T" is dark as shown in Fig.5.6 (right).

5.6 Conclusions

In this chapter, we have presented experimental results that demonstrate the effectiveness of our THz imaging system based on Rydberg atoms for real-world applications. We have shown that our THz imaging system can image human skin placed behind a piece of polymer. We have also shown different electronic devices many look the same by optical imaging , any differences can be distinguished by imaging their internal structures through THz imaging without causing internal damage. A sample made from two different polymer materials was imaged at two different frequencies and the images have been characterised. The spatial resolutions for these two frequencies have been calculated and corrected by the magnification factor. Our system is diffraction limited spatial resolution, which is limited by the THz imaging optics. These imaging results for the two different polymer materials provide the necessary motivation for the next chapter, which is

multispectral THz imaging.

Chapter 6

Progress Toward Multispectral Imaging in THz Frequency Range

In this chapter, we investigate polarisation spectroscopy of an excited state transition in a room-temperature rubidium vapour as a step towards multispectral imaging in the THz range. In polarisation spectroscopy, anisotropy is induced in the atomic medium via application of circularly polarised coupling beam resonant with the $5S_{1/2} \rightarrow 5P_{3/2}$ transition, which is then probed by scanning a beam across the $5P_{3/2} \rightarrow 6S_{1/2}$ transition. By performing polarimetry on the probe beam, we observe a dispersive spectral feature. We determined the excitation polarised spectra as a function of the coupling power for both isotopes and concluded that Autler-Townes splitting results in a sub-feature at high powers. This sub-feature is theoretically modelled, which shows it is enhanced by Doppler averaging. This spectroscopy technique results in a narrow dispersive signal, which can be ideal for laser frequency stabilisation of excited-state transitions, for example in the THz imaging system. The chapter concludes by showing the Rb atomic system that uses three excitation lasers to reach Rydberg states, which can then be used to perform THz imaging (similar to the method described for Cs in Chapter 3). The Rb vapour emits a different wavelength than that emitted by Cs atoms which is useful because from the THz multispectral imaging we can obtain more information

for imaging samples containing different materials.

6.1 Multispectral Imaging

Each material has a spectral response, which is a specific means by which to measure its ability to transmit, reflect, and absorb light. The spectral response can give additional information about an object composed of different materials with similar colours but different properties which the human eye fails to capture. Multispectral imaging (MSI) is a technique of spectral sensing that captures images and includes spectral information at specific wavelengths in narrow spectral bands. In order to separate the wavelengths, filters or instruments sensitive only to certain wavelengths are used [208]. The development of multispectral imaging started as a remote sensing technique [209, 210, 211], but in the past few years, the use of multispectral images has enabled greater contrast between different materials and is now used for a variety of imaging purposes, including medical diagnoses, [212, 213, 214], art conservation [215], the food industry [216], in the quality assessment process for products, controlling agricultural and water resources [217, 218] , and archaeology [219]. Multispectral imaging systems are becoming faster and more portable, enabling quick investigations and analyses of crime scene details [220].

There are different methods to capture images in multispectral imaging systems. Rotating a disc containing fixed wavelength filters in time with the camera's shutter speed or multiple sensors can be combined [221]. The disadvantages of these methods are that the apparatus needed is often bulky and relatively expensive. Another technique to achieve multispectral imaging is to place tuneable bandpass filters within the camera's optical path, such as a liquid crystal tuneable filter [222] or optical filters [223]. Some researchers have performed multispectral imaging using two regular digital cameras, with an appropriate pair of colour filters chosen for each [224].

Previously, detailed studies have been performed on the multispectral imaging sys-

tem in the optical frequency range, and it has developed to cover the visible, and near-infrared frequency range [225, 226]. However, multispectral imaging in the THz frequency range is challenging because changing the frequency of devices is inconvenient and time consuming. Therefore, several studies have been conducted in multispectral imaging in the THz frequency range. For instance, dual-THz frequency imaging using a tuneable quantum cascade laser (QCL) has been demonstrated. Here the image was created by raster scanning the sample, and by switching between two frequencies-3.05 and 3.24 THz, at each sample position [227]. Also this imaging system at five frequencies of 3.05, 3.18, 3.24, 3.30, and 3.35 THz, was used to determine the attenuation coefficients of pentaerythritol tetranitrate (PETN), along with several other polycrystalline materials [228].

In Chapter 5, we obtained an image with different contrast when we measured the sample at two different frequencies. However, it required replacing the THz source and the Rydberg laser, which means this method is inconvenient and time-consuming. Therefore, we wish to perform multispectral imaging by having a dual-species THz imager, as shown in Fig.6.1.

There are two atomic species (Cs and Rb) in the same cell [93], and two different sets of IR pump lasers; each set will excite different species to create two sheets of Rydberg atoms within the vapour cell. The Cs and Rb vapour cell will be illuminated by two co-propagating THz fields. The two THz fields are combined using a beam splitter then propagate perpendicularly to the IR pump lasers. Each THz field will interact with a different sheet of Rydberg atoms, leading to two different optical fluorescence emissions. Interaction between the THz field and the Cs sheet of Rydberg atoms causes the atoms to respond by emitting green fluorescence; blue-turquoise fluorescence is emitted by atoms when the other THz field interacts with the sheet of Rb atoms. These fluorescences can be separated using a dichroic mirror after the cell to create a real-time dual-frequency imaging system. Using this system would allow us to capture an image of the two different incident THz fields using two different optical cameras.

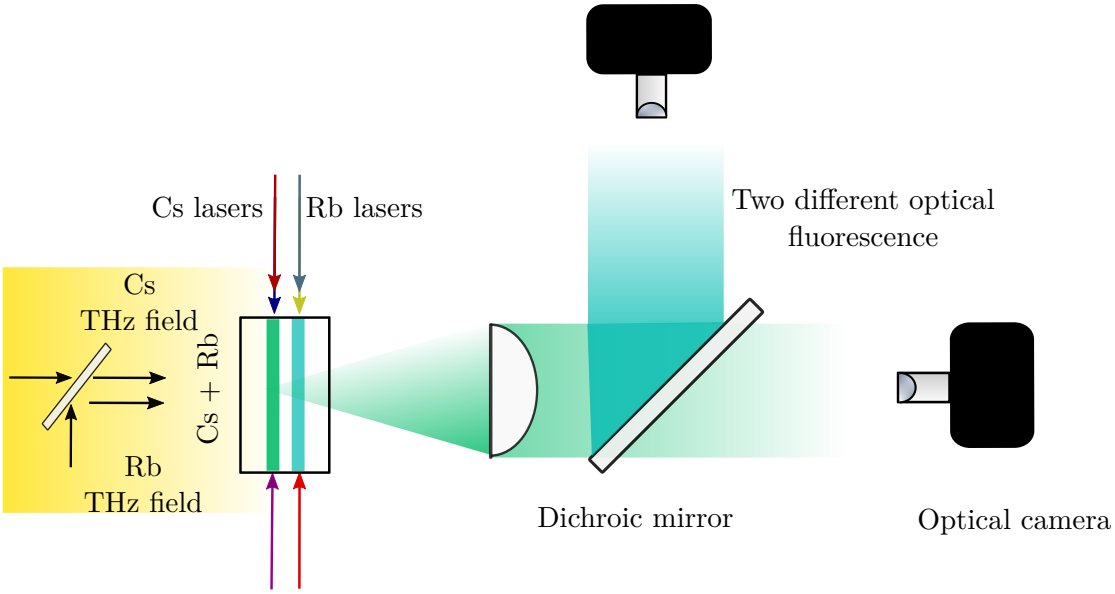

Figure 6.1: **Multispectral THz imager experimental set-up:** Two sheets of Rydberg atoms are excited by IR pump lasers within the vapour cell, containing two atomic species, Cs and Rb. Two THz fields, are combined by beam splitter, then propagate perpendicularly to the IR pump beams; each THz field will interact with a different atomic species. The atoms respond by emitting two different optical fluorescences. The THz field, which interacts with the Cs vapour, will emit a green fluorescence, and the other THz field, which interacts with the Rb vapour, will emit blue-turquoise fluorescence, which can then be separated by a dichroic mirror, and the image of the two different incident THz fields can be captured using two different optical cameras.

In this chapter, we present progress towards multispectral imaging in the THz frequency range. Excited state polarisation spectroscopy in Rb, which has a narrow dispersive signal, will be used for laser frequency stabilisation of excited-state transition in the multispectral imaging experiments based on Cs and Rb atoms.

6.2 Excited State Polarisation Spectroscopy in Rb

6.2.1 Experiment

The experimental layout for studying the polarisation spectroscopy of an excited state transition is shown in Fig. 6.2(a). A circularly polarised coupling beam at

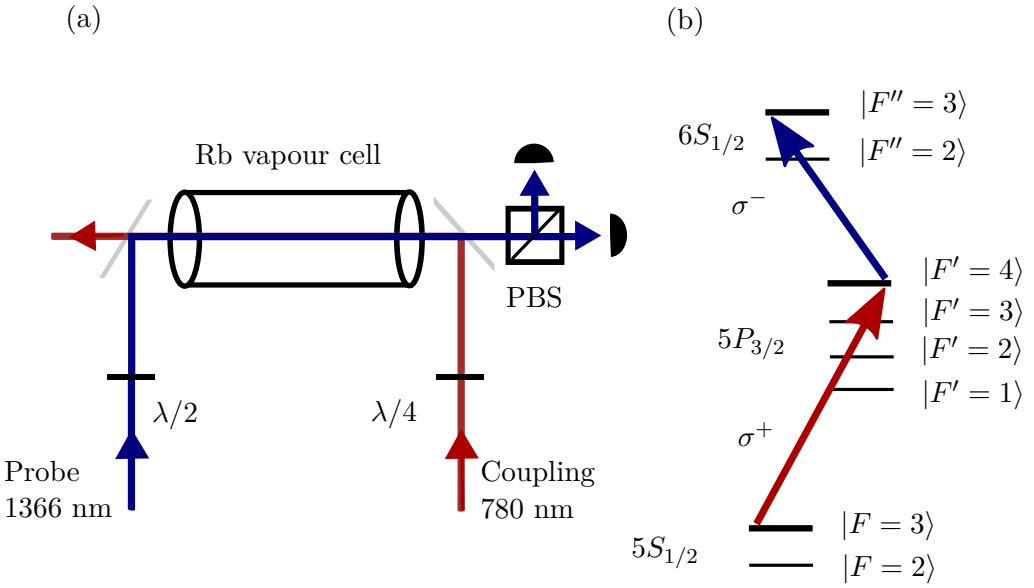

Figure 6.2: **Experimental setup and level diagram:** (a) Experimental setup: A linearly-polarised probe beam (blue arrow) counter-propagates with a circularly polarised coupling beam (red arrow). A dichroic mirror is used to overlap the beams and direct them through a rubidium vapor cell. A polarising beam splitter (PBS) analyses the rotation of the probe beam that is detected after the cell using a differencing photodiode (DPD). We assume that a quantisation axis is defined in the direction of probe beam propagation. (b) Schematic of the hyperfine structure of the atomic states in ^{85}Rb relevant to the excited-state polarisation spectroscopy. The ground state, $5S_{1/2}\ |F=3\rangle$, is coupled to the intermediate state, $5P_{3/2}\ |F'=4\rangle$, by a coupling laser with wavelength $\lambda_c = 780$ nm. The intermediate state is then coupled to the excited state $6S_{1/2}\ |F''=3\rangle$ by a probe laser with $\lambda_p = 1366$ nm. The component of the probe which drives σ^- transitions is preferentially absorbed because there are no σ^+ allowed transitions from the $5P_{3/2}\ |F'=4, m'_F=4\rangle$. Figure taken from [229].

$\lambda_c = 780$ nm (1.2 mm 1/e^2 beam radius) counter-propagates with a weak, linearly polarised probe beam at $\lambda_p = 1366$ nm (1.6 mm 1/e^2 beam radius). The beams are combined using dichroic mirrors, they are directed through the vapour cell containing ^{85}Rb and ^{87}Rb in natural abundance. Fig. 6.2(b) shows the relevant atomic energy levels. This experiment uses a three-level system for ^{85}Rb. The ground state, $5S_{1/2}\ |F=3\rangle$, is coupled to the intermediate state, $5P_{3/2}\ |F'=4\rangle$, using a coupling laser. The intermediate state is then coupled to the excited state $6S_{1/2}\ |F''=3\rangle$ using a probe laser. Using ground state polarisation spectroscopy, the frequency of the coupling laser is stabilised to the $5S_{1/2}|F=3\rangle \rightarrow 5P_{3/2}|F'=4\rangle$

transition, and the probe laser frequency is scanned across the $5P_{3/2}|F' = 4\rangle \rightarrow 6S_{1/2}|F'' = 3\rangle$ transition. The probe beam, after passing through the vapour cell, is split by a polarising beam splitter (PBS) which is oriented at 45° to the plane of polarisation of the beam. The resulting signal from the PBS is a pair of orthogonally polarised beams, each one is directed to a photodiode, producing signals S_1 and S_2. In the absence of birefringence within the system, we expect that $S_1 = S_2$. The probe laser frequency is calibrated with a Fabry-Perot etalon (not shown), which has a free spectral range of 1 GHz. Throughout our measurements, we used a probe beam power of 27 μW and coupling powers of up to 5 mW.

6.2.2 Result and discussion

Fig. 6.3 shows four signals resulting from coupling power of 200 μW and 27 μW probe power. The top of the figure (a) and (b), show the photodiode signals S_1 and S_2. Each signal contains a Lorentzian shape as a result of the difference in absorption between left and right circularly polarised beam as well as a dispersive shape resulting from the difference in dispersion between left and right circularly polarised beam. The sum of these signals $(S_1 + S_2)/2$ is the transmission of the probe beam which results in a Lorentzian profile shown in Fig. 6.3(c) for ^{85}Rb, while, subtraction of these signals $(S_1 - S_2)/2$, results in a dispersive lineshape, as shown in Fig. 6.3(d). An explanation for the polarisation spectrum feature can be given as follows; we assume that a quantisation axis is defined in the direction of probe beam propagation, the coupling beam which is circularly polarised induces anisotropy in the atomic medium by driving σ^+ transitions and preferentially pumping population into states with higher m_F.

We consider the linearly polarised probe beam in the excited state transition to be a superposition of left and right circular polarisation, this beam is used to couple states with $|F' = 4\rangle$ to $|F'' = 3\rangle$; consequently, the component of the beam which drives σ^- transitions is preferentially absorbed because there are no allowed σ^+ transitions from $|F' = 4, m'_F = 4\rangle$ state to $|F'' = 3, m''_F = 3\rangle$ state. The

difference in absorption coefficients between left and right circularly polarised beam ($\Delta\alpha = \alpha^+ - \alpha^-$) is proportional to the sum of the two signal S_1 and S_2 which has a Lorentzian profile

$$\frac{S_1 + S_2}{2} \propto \Delta\alpha. \tag{6.1}$$

As described by the Kramers-Kronig relation [230], there is a concomitant change in refractive index together with the change in absorption coefficients, where the difference in refractive indices between a left and right circularly polarised beam ($\Delta n = n^+ - n^-$) is proportional to the difference between the two signals S_1 and S_2 which produces the dispersion shaped signal

$$\frac{S_1 - S_2}{2} \propto \Delta n. \tag{6.2}$$

This dispersive signal is a convenient, modulation-free signal and this technique can be used for laser frequency stabilisation. In Fig. 6.3 it can be observed that there is a smaller feature at approximately +70 MHz, which corresponds to excitation via the $|F' = 3\rangle$ state. This observed hyperfine splitting is due to the $F'' = 3$ state, which is scaled by the ratio of the wavelengths of the beams 1- λ_c/λ_p [231].

We study the development of the excited state polarisation spectroscopy signal as a function of coupling power as shown in Fig. 6.4 (a-e). In response to an increase in coupling power, the dispersive signal broadens and increases in size, thereafter a second sub-Doppler dispersive signal which has the opposite sign to the original signal, is observed on resonance. As coupling power increases further, the magnitude of the sub-feature and the linewidth of the main signal increase. As the ground state transition is saturated, power broadening and Autler-Townes splitting (ATS) occurs in the intermediate state which causes this sub-feature.

The effect of Doppler averaging on the polarisation spectroscopy signal can be investigated using numerical modelling. This is achieved by describing the atoms

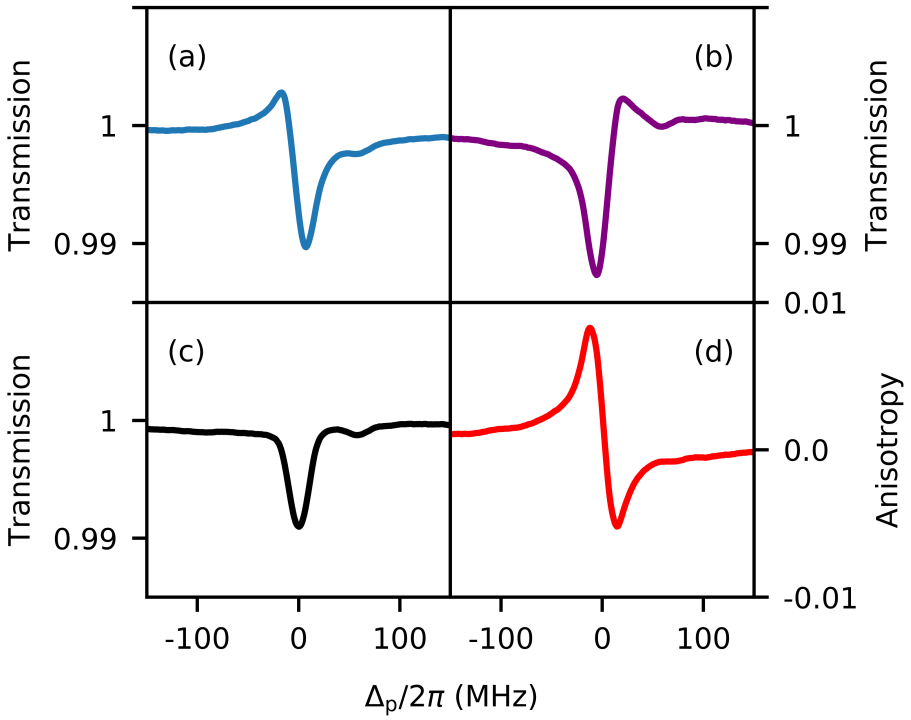

Figure 6.3: **Absorptive and dispersive lineshapes for two components of excited-state spectroscopy:** (a) and (b) Probe transmission signals recorded individually from each photodiode S_1 (blue line) and S_2 (purple line), (c) the average transmission $(S_1 + S_2)/2$ of these two signals. (d) The difference of the Probe transmission signals $(S_1 - S_2)/2$ is a dispersive profile, the detuning is with respect to $F'' = 4$. A small peak at around +70 MHz can be observed which is due to the $F'' = 3$ hyperfine state. Figure taken from [229].

using a simplified three-level scheme and finding the steady-state solution by using the optical Bloch equations. The optical Bloch equations are derived from solving Lindblad master equation as a function of the time evolution of the density matrix [111] as outlined in Chapter 2.

As demonstrated by the experimental spectra, when probing the excited state transition we see that the real part of the steady-state probe coherence between the intermediate and excited state $\mathrm{Re}(\rho_{23})$ is equivalent to the difference in the refractive index. The refractive index difference is, in turn, proportional to the probe dispersion signal, which is our experimental signal. The solution of the steady-state probe coherence element of the density matrix (ρ_{23}) between the intermediate state

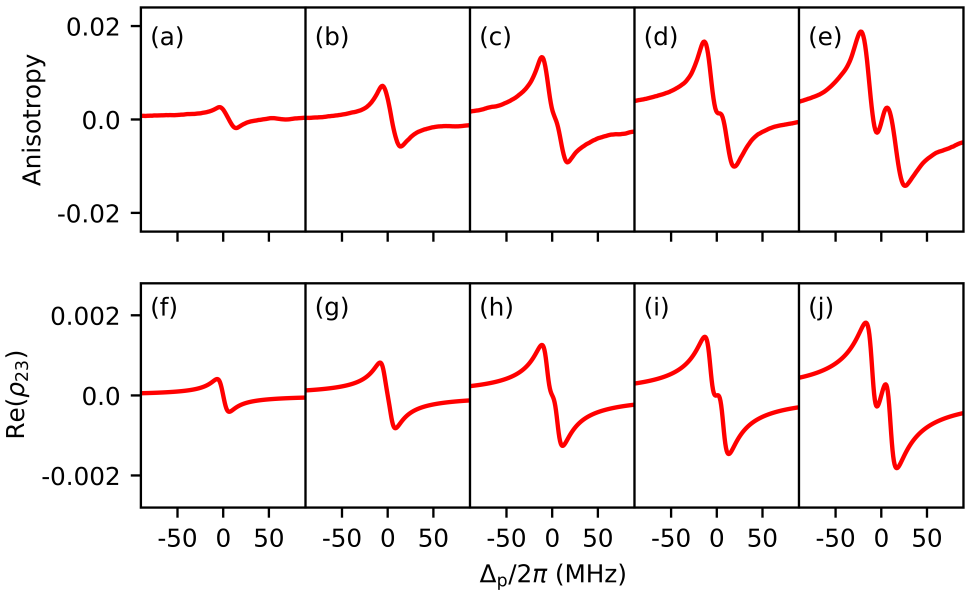

Figure 6.4: **Excited-state polarisation spectroscopy as a function of coupling power:** (a-e) Excited-state polarisation spectroscopy signals with varying coupling power experimentally and (f-j) theoretically by solving the real part of the steady-state probe coherence in optical Bloch equations. The experiment and theory qualitatively look similar and due to Autler-Townes splitting of the intermediate state a sub-feature appears at a critical value by coupling laser Rabi frequency. Experimental parameters: Probe laser Rabi frequency $\Omega_p/2\pi$= 2.7 MHz, and coupling laser $\Omega_c/2\pi$= (a) 6.9 MHz (50 μW), (b) 13.9 MHz (0.2 mW), (c) 21.9 MHz (0.5 mW), (d) 27.8 MHz (0.8 mW) and (e) 43.9 MHz (2.0 mW). Theoretical parameters: Probe laser Rabi frequency $\Omega_p/2\pi$= 2.7 MHz, and coupling laser $\Omega_c/2\pi$= (f) 2.8 MHz, (g) 4.6 MHz, (h) 7.3 MHz, (i) 9 MHz and (j) 12.7 MHz. Figure taken from [229].

and excited state can be obtained, by solving Eq. 2.43e of motion for the density matrix element ($\dot{\rho}_{23}$), with $\dot{\rho}_{23}$=0 and using the result from [232]

$$\rho_{23} = \frac{\frac{i{\Omega_c}^2\Omega_p\gamma_{12}}{4}}{\Gamma_1{\Delta_c}^2 + \Gamma_1{\gamma_{12}}^2 + \gamma_{12}{\Omega_c}^2}\left[1 + \frac{\gamma_c(1+\frac{i\Delta_c}{\gamma_{12}})}{\gamma_{23}+i\Delta_p}\right] \times \left[\gamma_{13} + i(\Delta_p+\Delta_c) + \frac{\frac{{\Omega_c}^2}{4}}{\gamma_{23}+i\Delta_p}\right]^{-1} \tag{6.3}$$

where Ω_c is the Rabi frequency of the coupling laser between the ground and intermediate states with detuning Δ_c and Ω_p is the Rabi frequency of the probe laser between the intermediate and the excited states with detuning Δ_p. γ_{12},γ_{13}

and γ_{23} are the decay terms of the coherences, as outlined in Eqs.2.42 and γ_{p} and γ_{c} are the terms describing dephasing due to the finite linewidth of the probe and coupling field respectively. We set $\Gamma_1 = 0$ by assuming there is no decay out from the lowest level.

In a thermal vapour, due to the Doppler effect, each atomic velocity class will experience a different laser detuning Δ_{p} and Δ_{c}. To include the effect of inhomogenous Doppler broadening into our model, we can modify the probe detuning and coupling detuning in our total Hamiltonian Eq. 2.31 as,

$$\Delta_{\mathrm{p}} \rightarrow \Delta_{\mathrm{p}} - k_{\mathrm{p}} \cdot v \tag{6.4a}$$

$$\Delta_{\mathrm{c}} \rightarrow \Delta_{\mathrm{c}} + k_{\mathrm{c}} \cdot v \tag{6.4b}$$

where k_{p} and k_{c} are the wave vectors of the probe and coupling beams, respectively, and v represents the atomic velocity in the direction of the probe beam propagation. We can model the optical response of the system by summing the contributions of each velocity class of atoms which are scaled according to the Maxwell-Boltzmann distribution at room temperature.

This model can be used to calculate and plot the steady-state probe coherence, as a function of probe detuning, which is parameterised by the coupling laser Rabi frequency, as shown in Fig. 6.4. The results of the numerical simulation are shown in Fig. 6.4(f-j). We found that the resulting dispersive signal is qualitatively consistent with experimental data.

The coupling Rabi frequency can be written,

$$\Omega_c = \frac{d_{23}}{\hbar}\sqrt{\frac{4P}{c\epsilon_0 \pi w^2}} \tag{6.5}$$

where P represents the peak beam power, w is the beam waist of the coupling laser, and d_{23} is the dipole moment between the intermediate state and excited state. In

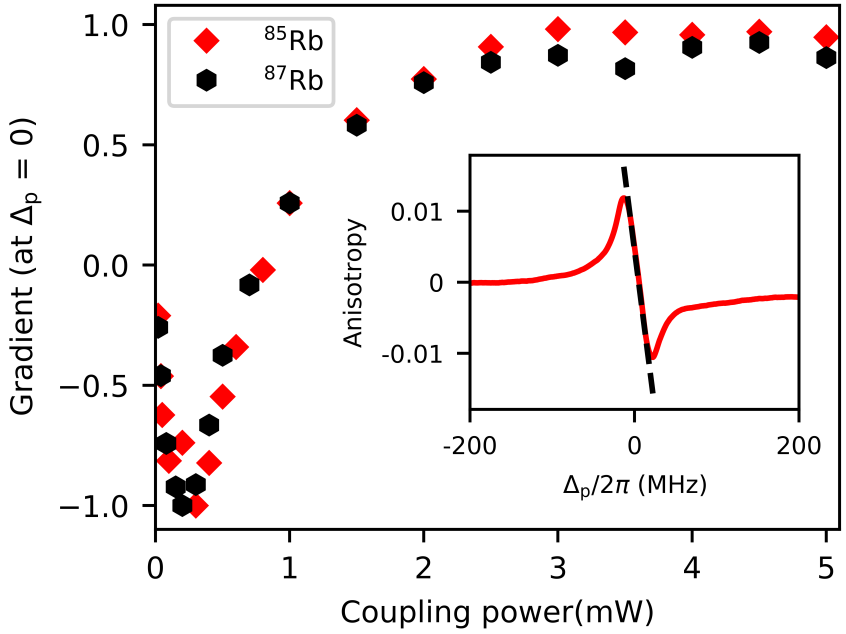

Figure 6.5: **Gradient of the polarisation spectroscopy signals for ^{85}Rb and ^{87}Rb:** On-resonance gradient, normalised to the maximum gradient of the polarisation spectroscopy signals for ^{85}Rb and ^{87}Rb when Δ_p is on resonance with varying coupling power. The inset figure is the dispersive signal from ^{85}Rb at coupling power of 0.2 mW, and the dashed line shows the on-resonance gradient. Figure taken from [229].

the experiment, the Rabi frequencies are found to be consistently higher than those indicated by the modelling; however, the model assumes the largest possible value of the dipole moment and dominated by the closed transition, $5P_{3/2}|m_{F'} = 4\rangle \rightarrow 6S_{1/2}|m_{F''} = 3\rangle$. However, in the actual experiment, in addition to the closed transition there will be on average a smaller effective dipole moment due to the population being distributed across all of the m_F states and the dipole moment will be an average over these states. Moreover, since the beams have a Gaussian intensity profile, the Rabi frequency varies spatially across the beam, resulting in inhomogeneous broadening since each atom experiences a different Rabi frequency.

To determine the conditions in which ATS occurs and the sub-feature appears, we recorded the gradient of the signal as a function of coupling power at two-photon resonance, i.e. at $\Delta_p = 0$ as shown in Fig. 6.5. Initially, the on-resonance gradi-

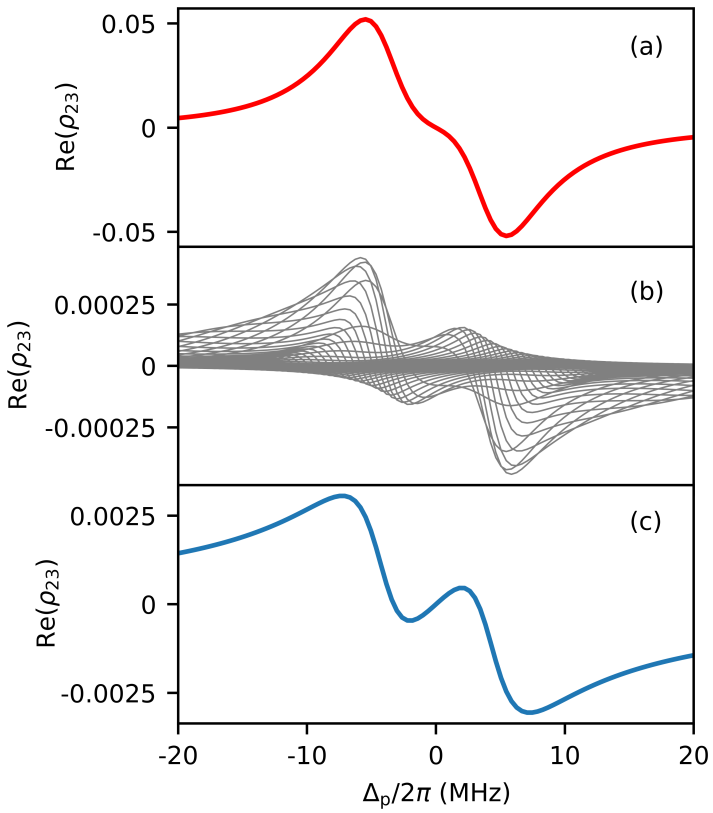

Figure 6.6: **The theoretical modelling of the excited-state polarisation spectroscopy signal depending on Doppler averaging:** The theoretical modelling of Doppler averaging on excited-state polarisation spectroscopy signal as a function of probe laser detuning Δ_p with different atomic velocity classes. The steady-state probe coherence Re(ρ_{23}) is proportional to the dispersion signal. (a) is the lineshape for v = 0. (b) non-zero velocity classes, $v_{max} = 200$ m/s and each velocity class separated by 2 m/s. (c) is the Doppler-averaged lineshape, where the contributions of non-zero velocity classes enhance the sub-feature. Figure taken from [229].

ent increases as the coupling power increases, up to a maximum around 0.3 mW. Thereafter, as splitting occurs, the slope decreases and then changes sign and increases, then levels off at higher powers. We can see that the on-resonance feature changes sign at around 0.8 mW of coupling power. Further, Fig. 6.5 shows very similar trends for ^{85}Rb and ^{87}Rb, similar to what Carr *et al* saw [115].

To demonstrate how the appearance of the sub-feature is related to Doppler averaging, we have shown how different velocity classes contribute to the overall signal.

Fig. 6.6 demonstrates the importance of using Doppler averaging when modelling this sub-feature. If all atoms are at rest, the dispersive signal has an on resonance gradient with a negative sign, as shown in Fig. 6.6(a) for certain values of coupling Rabi frequency.

When considering the effect of the contribution from varying velocity classes, as shown in Fig. 6.6(b), by integrating over all velocity classes, the Doppler-averaged shape and the evolution of the sub-feature can be determined, which produces the lineshape seen in Fig. 6.6(c). In our model of atomic distribution, we summed over the velocity classes separated by 2 m/s with a maximum velocity of $v_{\max} = 200$ m/s. This cut-off point was determined as increasing velocity greater than this resulted in no further changes to the signal shape. In the simulation, we applied the following parameters, probe laser Rabi frequency $\Omega_p/2\pi$= 3.7 MHz, a coupling laser Rabi frequency $\Omega_c/2\pi$= 12.8 MHz, dephasing decay due to the finite linewidth of the probe and coupling field, respectively, $\gamma_{\mathrm{p}}/2\pi = \gamma_{\mathrm{c}}/2\pi = 0.5$ MHz, the decay terms of the coherences $\gamma_{12}/2\pi = 3$ MHz, $\gamma_{13}/2\pi = 2.8$ MHz, $\gamma_{23}/2\pi = 5.3$ MHz and a temperature T= 293 K.

Based on our model, we conclude that the onset of the narrow sub-feature due to ATS is enhanced by the contribution of atoms with non-zero velocity and occurs at a lower coupling power in thermal atoms than in cold atoms. These findings concur with similar results in other pump-probe experiments, different lineshapes and narrow sub-features generated by Doppler averaging have been observed [233, 234, 235].

6.3 THz Imaging System based on Rb Atoms

The ^{85}Rb atomic system that will be used in future experiments to achieve multispectral imaging in the THz frequency range is shown in Fig.6.7. It is similar to the atomic system for Cs that we used in this thesis and outlined in Chapter 3. This atomic system uses three IR lasers in three steps to excite the atoms to Rydberg

levels. The probe laser (780 nm) excites atoms from $5S_{1/2}$ to $5P_{3/2}$, then the atoms are promoted from $6P_{3/2}$ to $7S_{1/2}$ by a coupling laser (1366 nm). Using the Rydberg laser (767 nm) we can excite the atoms to $17P_{3/2}$ state. Applying a resonant THz field will allow us to couple two Rydberg states. Using the method developed in [94], we can identify the optimum transition for imaging in this system which is $17P_{3/2} \rightarrow 16D_{5/2}$ at a frequency of 0.65 THz. The interaction of the THz field with the excited atoms leads to the emission of a blue turquoise fluorescence due to the difference between Cs and Rb atomic structures, as shown in the inset picture of Fig.6.7. The strong optical fluorescence that is emitted from $16D_{5/2}$ state at 491 nm [94], corresponds to $16D_{5/2} \rightarrow 5P_{3/2}$ decay.

In the multispectral imaging experiments, we want to illuminate a dual-species Cs-Rb cell by two different THz fields, (0.55 THz for Cs and 0.65 THz for Rb), that will allowed us to obtain two different wavelengths for imaging, 535 nm and 491 nm, respectively.

6.4 Conclusions

In this chapter, we have presented an introduction of multispectral imaging. We have investigated excited state polarisation spectroscopy in Rb as progress toward multispectral THz imaging, and developed excited state polarisation spectroscopy as a function of coupling power in room-temperature rubidium vapor. Via experimentation, we determined the characteristics of a sub-feature, subsequently applying a theoretical model to demonstrate enhancement of this feature via Doppler averaging. The narrow dispersion signal generated is ideal for laser frequency stabilisation, due to its sharp derivative and simple experimental setup. In further application of these findings, we plan to apply this technique to terahertz imaging experiments. The Rb atomic system which will be used to obtain multispectral THz imaging in the future experiments is displayed.

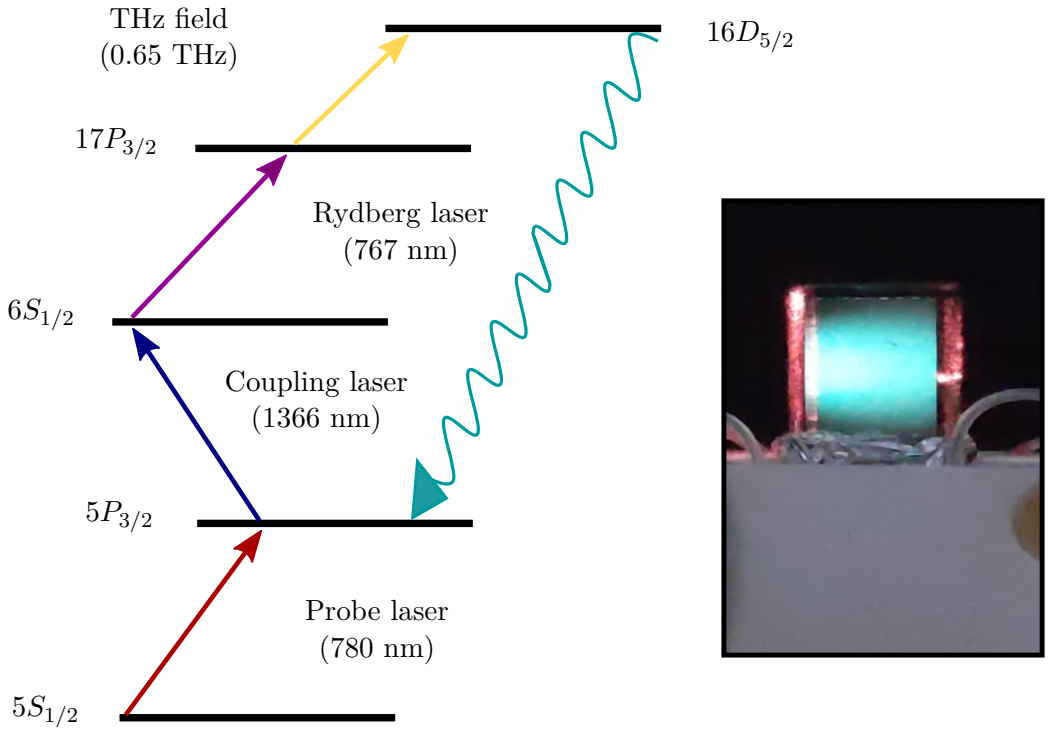

Figure 6.7: **THz imaging system based on Rb atom:** Schematic of the atomic system of ^{85}Rb used in THz imaging. The red, blue and purple arrows correspond to the laser excitations. A probe laser with wavelength $\lambda = 780$ nm coupled the ground state $5S_{1/2}$ to the intermediate state, $5P_{3/2}$, a coupling laser with wavelength $\lambda = 1366$ nm coupled the intermediate state to the excited state $6S_{1/2}$. The excited state then coupled to the Rydberg states $17P_{3/2}$ by Rydberg laser with wavelength $\lambda = 767$ nm. The yellow arrow represents the THz field that couples the two Rydberg states $17P_{3/2}$ and $16D_{5/2}$. The blue turquoise arrow is the decay pathway of the optical fluorescence that is emitted from the $16D_{5/2}$ state to $5P_{3/2}$ state. The inset picture is the image of the cell with blue-turquoise fluorescence taken by Dr.Shuying Chen.

Chapter 7

Conclusion and Outlook

This thesis studies a THz imaging system using atomic vapour. IR lasers excite Caesium atomic vapour to a targeted Rydberg state, creating a 2D THz sensor that converts an incident THz field into a detectable green fluorescence. This thesis uses a 2D sheet of excited Rydberg atoms as a new THz detector to analyse polymer materials using the Beer-Lambert Law to determine the absorption coefficient. This imaging system is calibrated to measure the THz intensity from the fluorescence emitted by the atomic vapour. In addition, the same experiment is performed using a commercial thermal THz power meter as a comparison experiment as the THz atomic detection technique is sensitive to any environmental changes in the system. The results of both experiments show good agreement.

This thesis also demonstrated some real-world applications of an atom-based THz imaging system; we showed that through THz imaging one can distinguish seemingly identical electronic components by imaging their internal structures. This system provided sufficient imaging contrast to distinguish between different materials in an image; in the case of a sample made from two different polymer materials when imaged at two different frequencies. This result was a motivation to pursue multispectral THz imaging. We made progress towards multispectral THz imaging by investigating excited-state polarisation spectroscopy in Rb. This technique was studied as a function of coupling power. In this technique, the 780 nm coupling

power beam induces a birefringence that is probed by the 1366 nm probe beam, resulting in narrow dispersive signals with excellent signal-to-noise ratios. Furthermore, by stabilising the frequency of the coupling beam using ground state polarisation spectroscopy, this technique can be used to frequency stabilise the probe beam in an excited state transition to perform imaging THz experiments.

There are still unanswered questions, in the measurements described in Chapter 4, the polymer samples were all taken from the same manufactured batch. We found that they give different results when they should be identical. Such experiments could be done by pressing these polymer materials and then squashing them, and repeating absorption coefficient measurements. However, we do not have the required equipment to do this experiment.

In the measurements described in Chapter 4, we found our absorption coefficient measurements are higher than the literature. We suggest that not all of the light is lost due to absorption, but is partially lost to reflection. Further work would measure the reflection loss from the surfaces of the material samples used in the materials analysis experiment. One approach could make measurements of samples with total thickness l, divided into n number of plates. Each plate, of thickness l/n, would provide additional reflection surfaces. This would allow us to determine the reflection losses. By measuring the transmission for each, then plotting it against the number of plates. If the transmission remains the same that means there is no reflection loss as we expected. When the reflection loss happens once, it will be constant for all measurements, which is the benefit of normalising the data. If the transmission is reduced, we can infer the reflection loss. This can be accounted for in Eq.7.1 [141]

$$T = (1 - R)e^{-\alpha l} \tag{7.1}$$

where T is the transmission and R is the Fresnel reflection formula. The reflection losses scales linearly with the number of plates (and therefore number of reflection

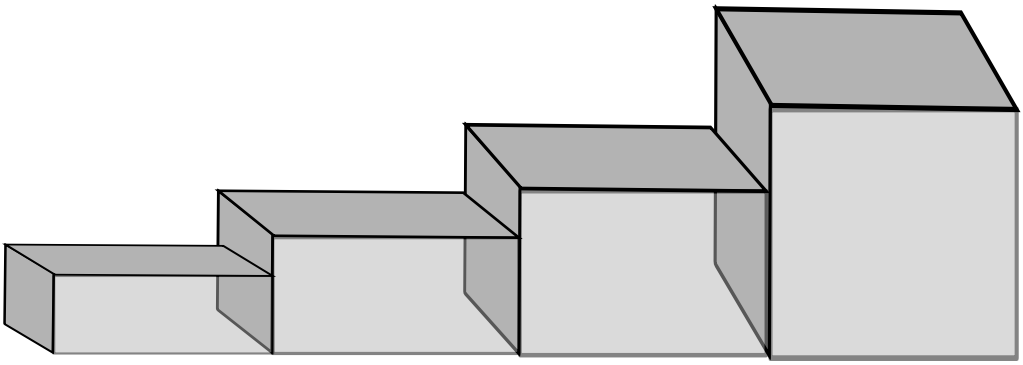

Figure 7.1: **Sample of polymer material with different thickness** One piece of polymer material with different thickness in steps to perform materials analysis experiment automatically using a motorised translation stage.

surfaces). However, we do not have enough data to perform these measurements.

Noise fluctuations in the atomic based imaging system can be reduced by automating the experiment. This can be done by using a motorised stepping stage on which the sample can be situated, and for each material, using a single sample containing different thicknesses as in Fig.7.1. By doing this, we will avoid opening the encased optical table to swap materials during the experiment, thereby reducing the cell temperature fluctuation.

Future work will attain multispectral imaging using a dual-species (Cs-Rb) vapour cell, providing a greater number of THz frequencies to image at. Such work will be a step forward in THz imaging in a variety of applications such as wind turbine inspection [236] and pharmaceutical industry's quality control [237]. We hope the principle of this technology and the dual-species imager could be applied in a wide range of applications in far future such as security screening [238] and industrial applications [239].

Bibliography

[1] SS Dhillon, MS Vitiello, EH Linfield, AG Davies, Matthias C Hoffmann, John Booske, Claudio Paoloni, M Gensch, Peter Weightman, GP Williams, et al. The 2017 terahertz science and technology roadmap. *Journal of Physics D: Applied Physics*, 50(4):043001, 2017.

[2] Leonardo Viti and Miriam Serena Vitiello. Tailored nano-electronics and photonics with two-dimensional materials at terahertz frequencies. *Journal of Applied Physics*, 130(17):170903, 2021.

[3] Mira Naftaly, Nico Vieweg, and Anselm Deninger. Industrial applications of terahertz sensing: state of play. *Sensors*, 19(19):4203, 2019.

[4] Shuting Fan, Yuezhi He, Benjamin S Ung, and Emma Pickwell-MacPherson. The growth of biomedical terahertz research. *Journal of Physics D: Applied Physics*, 47(37):374009, 2014.

[5] Y Watanabe, K Kawase, T Ikari, H Ito, Y Ishikawa, and H Minamide. Component spatial pattern analysis of chemicals using terahertz spectroscopic imaging. *Applied Physics Letters*, 83(4):800–802, 2003.

[6] Leili Afsah-Hejri, Parvaneh Hajeb, Parsa Ara, and Reza J Ehsani. A comprehensive review on food applications of terahertz spectroscopy and imaging.

Comprehensive Reviews in Food Science and Food Safety, 18(5):1563–1621, 2019.

[7] Uroš Puc, Andreja Abina, Melita Rutar, Aleksander Zidanšek, Anton Jeglič, and Gintaras Valušis. Terahertz spectroscopic identification of explosive and drug simulants concealed by various hiding techniques. *Applied optics*, 54(14):4495–4502, 2015.

[8] Corinna L Koch Dandolo, Maxime Lopez, Kaori Fukunaga, Yoshimi Ueno, Ruven Pillay, David Giovannacci, Yann Le Du, Xueshi Bai, Michel Menu, and Vincent Detalle. Toward a multimodal fusion of layered cultural object images: complementarity of optical coherence tomography and terahertz time-domain imaging in the heritage field. *Applied Optics*, 58(5):1281–1290, 2019.

[9] Q Cassar, CL Koch-Dandolo, Jean-Paul Guillet, M Roux, F Fauquet, JB Perraud, and P Mounaix. Characterization of varnish ageing and its consequences on terahertz imagery: Demonstration on a painting presumed of the french renaissance. *Journal of Infrared, Millimeter, and Terahertz Waves*, 41(12):1556–1566, 2020.

[10] Mikiya Kato, Saroj R Tripathi, Kosuke Murate, Kazuki Imayama, and Kodo Kawase. Non-destructive drug inspection in covering materials using a terahertz spectral imaging system with injection-seeded terahertz parametric generation and detection. *Optics express*, 24(6):6425–6432, 2016.

[11] Michael C Kemp, Antony Glauser, and Colin Baker. Recent developments in people screening using terahertz technology: seeing the world through terahertz eyes. *Terahertz for Military and Security Applications IV*, 6212:224–233, 2006.

[12] Steven R Murrill, Eddie L Jacobs, Steven K Moyer, Carl E Halford, Steven T Griffin, Frank C De Lucia, Douglas T Petkie, and Charmaine C Franck. Tera-

hertz imaging system performance model for concealed-weapon identification. *Applied optics*, 47(9):1286–1297, 2008.

[13] Liangliang Zhang, Hua Zhong, Chao Deng, Cunlin Zhang, and Yuejin Zhao. Terahertz wave reference-free phase imaging for identification of explosives. *Applied Physics Letters*, 92(9):091117, 2008.

[14] Jiayu Zhao, Wei Chu, Lanjun Guo, Zhi Wang, Jing Yang, Weiwei Liu, Ya Cheng, and Zhizhan Xu. Terahertz imaging with optical resolution by femtosecond laser filament in air. In *International Conference on Ultrafast Phenomena*, pages 09–Wed. Optica Publishing Group, 2014.

[15] Sheng-Hui Ding, Qi Li, Rui Yao, and Qi Wang. High-resolution terahertz reflective imaging and image restoration. *Applied optics*, 49(36):6834–6839, 2010.

[16] HA Hafez, X Chai, A Ibrahim, S Mondal, D Férachou, X Ropagnol, and T Ozaki. Intense terahertz radiation and their applications. *Journal of Optics*, 18(9):093004, 2016.

[17] Tzu-Fang Tseng, Szu-Chi Yang, Yuan-Ta Shih, Yuan-Fu Tsai, Tzung-Dau Wang, and Chi-Kuang Sun. Near-field sub-thz transmission-type image system for vessel imaging in-vivo. *Optics Express*, 23(19):25058–25071, 2015.

[18] E Pickwell and VP Wallace. Biomedical applications of terahertz technology. *Journal of Physics D: Applied Physics*, 39(17):R301, 2006.

[19] Kirill I Zaytsev, Konstantin G Kudrin, Valeriy E Karasik, Igor V Reshetov, and Stanislav O Yurchenko. In vivo terahertz spectroscopy of pigmentary skin nevi: Pilot study of non-invasive early diagnosis of dysplasia. *Applied Physics Letters*, 106(5):053702, 2015.

[20] OA Smolyanskaya, NV Chernomyrdin, AA Konovko, KI Zaytsev, IA Ozheredov, OP Cherkasova, MM Nazarov, J-P Guillet, SA Kozlov, Yu V Kistenev,

et al. Terahertz biophotonics as a tool for studies of dielectric and spectral properties of biological tissues and liquids. *Progress in Quantum Electronics*, 62:1–77, 2018.

[21] Udo Kaatze and Christof Hübner. Electromagnetic techniques for moisture content determination of materials. *Measurement Science and Technology*, 21(8):082001, 2010.

[22] Daniel M Mittleman. Twenty years of terahertz imaging. *Optics express*, 26(8):9417–9431, 2018.

[23] JR Gao, JN Hovenier, ZQ Yang, JJA Baselmans, A Baryshev, M Hajenius, TM Klapwijk, AJL Adam, TO Klaassen, BS Williams, et al. Terahertz heterodyne receiver based on a quantum cascade laser and a superconducting bolometer. *Applied Physics Letters*, 86(24):244104, 2005.

[24] M Hangyo, M Tani, and T Nagashima. Terahertz time-domain spectroscopy of solids: a review. *International journal of infrared and millimeter waves*, 26(12):1661–1690, 2005.

[25] Peter R Smith, David H Auston, and Martin C Nuss. Subpicosecond photoconducting dipole antennas. *IEEE Journal of Quantum Electronics*, 24(2):255–260, 1988.

[26] Martin Van Exter and Daniel R Grischkowsky. Characterization of an optoelectronic terahertz beam system. *IEEE Transactions on Microwave Theory and Techniques*, 38(11):1684–1691, 1990.

[27] Qi Wu and X-C Zhang. Free-space electro-optic sampling of terahertz beams. *Applied Physics Letters*, 67(24):3523–3525, 1995.

[28] Q Wu and X-C Zhang. 7 terahertz broadband gap electro-optic sensor. *Applied Physics Letters*, 70(14):1784–1786, 1997.

[29] Juraj Darmo, Vincas Tamosiunas, Gernot Fasching, Josef Kröll, Karl Unterrainer, Mattias Beck, Marcella Giovannini, Jerome Faist, Christian Kremser, and Paul Debbage. Imaging with a terahertz quantum cascade laser. *Optics express*, 12(9):1879–1884, 2004.

[30] Stefano Barbieri, Jesse Alton, Colin Baker, Thomas Lo, Harvey E Beere, and David Ritchie. Imaging with thz quantum cascade lasers using a schottky diode mixer. *Optics Express*, 13(17):6497–6503, 2005.

[31] Paul Dean, Muhammad U Shaukat, Suraj P Khanna, Subhasish Chakraborty, Mohammad Lachab, Andrew Burnett, Giles Davies, and Edmund H Linfield. Absorption-sensitive diffuse reflection imaging of concealed powders using a terahertz quantum cascade laser. *Optics Express*, 16(9):5997–6007, 2008.

[32] Marcel JE Golay. The theoretical and practical sensitivity of the pneumatic infra-red detector. *Review of Scientific Instruments*, 20(11):816–820, 1949.

[33] TS Hartwick, DT Hodges, DH Barker, and FB Foote. Far infrared imagery. *Applied Optics*, 15(8):1919–1922, 1976.

[34] Binbin B Hu and Martin C Nuss. Imaging with terahertz waves. *Optics letters*, 20(16):1716–1718, 1995.

[35] Ian S Gregory, WR Tribe, Colin Baker, BE Cole, MJ Evans, L Spencer, M Pepper, and Mohamed Missous. Continuous-wave terahertz system with a 60 db dynamic range. *Applied Physics Letters*, 86(20):204104, 2005.

[36] Wai Lam Chan, Jason Deibel, and Daniel M Mittleman. Imaging with terahertz radiation. *Reports on progress in physics*, 70(8):1325, 2007.

[37] Marta Di Fabrizio, Annalisa D'Arco, Sen Mou, Luigi Palumbo, Massimo Petrarca, and Stefano Lupi. Performance evaluation of a thz pulsed imaging system: point spread function, broadband thz beam visualization and image reconstruction. *Applied Sciences*, 11(2):562, 2021.

[38] Adrian Dobroiu, Masatsugu Yamashita, Yuichi N Ohshima, Yasuyuki Morita, Chiko Otani, and Kodo Kawase. Terahertz imaging system based on a backward-wave oscillator. *Applied optics*, 43(30):5637–5646, 2004.

[39] Rüdeger Köhler, Alessandro Tredicucci, Fabio Beltram, Harvey E Beere, Edmund H Linfield, A Giles Davies, David A Ritchie, Rita C Iotti, and Fausto Rossi. Terahertz semiconductor-heterostructure laser. *Nature*, 417(6885):156–159, 2002.

[40] Benjamin S Williams, Sushil Kumar, Qing Hu, and John L Reno. High-power terahertz quantum cascade lasers. In *2006 Conference on Lasers and Electro-Optics and 2006 Quantum Electronics and Laser Science Conference*, pages 1–2. IEEE, 2006.

[41] RA Lewis. A review of terahertz detectors. *Journal of Physics D: Applied Physics*, 52(43):433001, 2019.

[42] Heiko Richter, Michael Greiner-Bär, SG Pavlov, AD Semenov, Martin Wienold, Lutz Schrottke, M Giehler, R Hey, HT Grahn, and H-W Hübers. A compact, continuous-wave terahertz source based on a quantum-cascade laser and a miniature cryocooler. *Optics express*, 18(10):10177–10187, 2010.

[43] Paul Dean, Yah Leng Lim, Alex Valavanis, Russell Kliese, Milan Nikolić, Suraj P Khanna, Mohammad Lachab, Dragan Indjin, Zoran Ikonić, Paul Harrison, et al. Terahertz imaging through self-mixing in a quantum cascade laser. *Optics letters*, 36(13):2587–2589, 2011.

[44] Nick Rothbart, Heiko Richter, Martin Wienold, Lutz Schrottke, Holger T Grahn, and Heinz-Wilhelm Hübers. Fast 2-d and 3-d terahertz imaging with a quantum-cascade laser and a scanning mirror. *IEEE Transactions on Terahertz Science and Technology*, 3(5):617–624, 2013.

[45] David Shrekenhamer, Claire M Watts, and Willie J Padilla. Terahertz single pixel imaging with an optically controlled dynamic spatial light modulator. *Optics express*, 21(10):12507–12518, 2013.

[46] Rayko Ivanov Stantchev, Xiao Yu, Thierry Blu, and Emma Pickwell-MacPherson. Real-time terahertz imaging with a single-pixel detector. *Nature communications*, 11(1):1–8, 2020.

[47] A Tessmann, I Kallfass, A Leuther, H Massler, M Schlechtweg, and O Ambacher. Metamorphic mmics for operation beyond 200 ghz. In *2008 European Microwave Integrated Circuit Conference*, pages 210–213. IEEE, 2008.

[48] Hua Qin, Jiandong Sun, Shixiong Liang, Xiang Li, Xinxin Yang, Zehao He, Cui Yu, and Zhihong Feng. Room-temperature, low-impedance and high-sensitivity terahertz direct detector based on bilayer graphene field-effect transistor. *Carbon*, 116:760–765, 2017.

[49] W Knap, F Teppe, Y Meziani, N Dyakonova, J Lusakowski, F Boeuf, T Skotnicki, D Maude, S Rumyantsev, and MS Shur. Plasma wave detection of sub-terahertz and terahertz radiation by silicon field-effect transistors. *Applied Physics Letters*, 85(4):675–677, 2004.

[50] R Tauk, Frederic Teppe, S Boubanga, Dominique Coquillat, Wojciech Knap, YM Meziani, C Gallon, F Boeuf, T Skotnicki, C Fenouillet-Beranger, et al. Plasma wave detection of terahertz radiation by silicon field effects transistors: Responsivity and noise equivalent power. *Applied Physics Letters*, 89(25):253511, 2006.

[51] Ruonan Han, Yaming Zhang, Dominique Coquillat, Hadley Videlier, Wojciech Knap, Elliott Brown, et al. A 280-ghz schottky diode detector in 130-nm digital cmos. *IEEE Journal of Solid-State Circuits*, 46(11):2602–2612, 2011.

[52] Ruonan Han, Yaming Zhang, Dominique Coquillat, Julie Hoy, Hadley Videlier, Wojciech Knap, Elliott Brown, et al. 280-ghz schottky diode detector in 130-nm digital cmos. In *IEEE Custom Integrated Circuits Conference 2010*, pages 1–4. IEEE, 2010.

[53] Alan WeiMin Lee and Qing Hu. Real-time, continuous-wave terahertz imaging by use of a microbolometer focal-plane array. *Optics letters*, 30(19):2563–2565, 2005.

[54] Alan WM Lee, Benjamin S Williams, Sushil Kumar, Qing Hu, and John L Reno. Real-time imaging using a 4.3-thz quantum cascade laser and a 320/spl times/240 microbolometer focal-plane array. *IEEE Photonics Technology Letters*, 18(13):1415–1417, 2006.

[55] Alan WM Lee, Qi Qin, Sushil Kumar, Benjamin S Williams, Qing Hu, and John L Reno. Real-time terahertz imaging over a standoff distance (> 25 meters). *Applied Physics Letters*, 89(14):141125, 2006.

[56] François Simoens and Jérôme Meilhan. Terahertz real-time imaging uncooled array based on antenna-and cavity-coupled bolometers. *Philosophical Transactions of the Royal Society A: Mathematical, Physical and Engineering Sciences*, 372(2012):20130111, 2014.

[57] Naoki Oda, Hajime Yoneyama, Tokuhito Sasaki, Masahiko Sano, Seiji Kurashina, Iwao Hosako, Norihiko Sekine, Takayuki Sudoh, and Tomoko Irie. Detection of terahertz radiation from quantum cascade laser using vanadium oxide microbolometer focal plane arrays. In *Infrared Technology and Applications XXXIV*, volume 6940, pages 982–993. SPIE, 2008.

[58] F Simoens, T Durand, J Meilhan, P Gellie, W Maineult, C Sirtori, S Barbieri, H Beere, and D Ritchie. Terahertz imaging with a quantum cascade laser and amorphous-silicon microbolometer array. In *Millimetre Wave and Terahertz Sensors and Technology II*, volume 7485, pages 151–160. SPIE, 2009.

[59] François Simoens, Jérôme Meilhan, and Jean-Alain Nicolas. Terahertz real-time imaging uncooled arrays based on antenna-coupled bolometers or fet developed at cea-leti. *Journal of Infrared, Millimeter, and Terahertz Waves*, 36(10):961–985, 2015.

[60] Erik Ojefors, Ullrich R Pfeiffer, Alvydas Lisauskas, and Hartmut G Roskos. A 0.65 thz focal-plane array in a quarter-micron cmos process technology. *IEEE Journal of Solid-State Circuits*, 44(7):1968–1976, 2009.

[61] Erik Öjefors, Neda Baktash, Yan Zhao, Richard Al Hadi, Hani Sherry, and Ullrich R Pfeiffer. Terahertz imaging detectors in a 65-nm cmos soi technology. In *2010 Proceedings of ESSCIRC*, pages 486–489. IEEE, 2010.

[62] Richard Al Hadi, Hani Sherry, Janusz Grzyb, Yan Zhao, Wolfgang Forster, Hans M Keller, Andreia Cathelin, Andreas Kaiser, and Ullrich R Pfeiffer. A 1 k-pixel video camera for 0.7–1.1 terahertz imaging applications in 65-nm cmos. *IEEE Journal of Solid-State Circuits*, 47(12):2999–3012, 2012.

[63] François Simoens, Jérôme Meilhan, Laurent Dussopt, Jean-Alain Nicolas, Nicolas Monnier, Gilles Sicard, Alexandre Siligaris, and Bruno Hiberty. Uncooled terahertz real-time imaging 2d arrays developed at leti: present status and perspectives. In *Micro-and Nanotechnology Sensors, Systems, and Applications IX*, volume 10194, pages 523–535. SPIE, 2017.

[64] Georgios C Trichopoulos, H Lee Mosbacker, Don Burdette, and Kubilay Sertel. A broadband focal plane array camera for real-time thz imaging applications. *IEEE Transactions on Antennas and Propagation*, 61(4):1733–1740, 2013.

[65] Georgios C Trichopoulos, Kagan Topalli, and Kubilay Sertel. Imaging performance of a thz focal plane array. In *2011 IEEE international symposium on antennas and propagation (APSURSI)*, pages 134–136. IEEE, 2011.

[66] Francois Simoens, Patrick Agnese, Alain Beguin, Jacques Carcey, Jean-Charles Cigna, Jean-Louis Pornin, Patrice Rey, Aurelie Vandeneynde, Louis Rodriguez, Olivier Boulade, et al. Submillimeter bolometers arrays for the pacs/herschel spectro-photometer. In *Millimeter and submillimeter detectors for astronomy II*, volume 5498, pages 177–186. SPIE, 2004.

[67] Barry N Behnken, Gamani Karunasiri, Danielle R Chamberlin, Peter R Robrish, and Jérôme Faist. Real-time imaging using a 2.8 thz quantum cascade laser and uncooled infrared microbolometer camera. *Optics letters*, 33(5):440–442, 2008.

[68] Robert W Boyd and CH Townes. An infrared upconverter for astronomical imaging. *Applied Physics Letters*, 31(7):440–442, 1977.

[69] Matteo Clerici, Daniele Faccio, Lucia Caspani, Marco Peccianti, Eleonora Rubino, Luca Razzari, François Légaré, Tsuneyuki Ozaki, and Roberto Morandotti. Ccd-based imaging and 3d space–time mapping of terahertz fields via kerr frequency conversion. *Optics Letters*, 38(11):1899–1901, 2013.

[70] Shuzhen Fan, Feng Qi, Takashi Notake, Kouji Nawata, Yuma Takida, Takeshi Matsukawa, and Hiroaki Minamide. Diffraction-limited real-time terahertz imaging by optical frequency up-conversion in a dast crystal. *Optics express*, 23(6):7611–7618, 2015.

[71] Shuzhen Fan, Feng Qi, Takashi Notake, Kouji Nawata, Takeshi Matsukawa, Yuma Takida, and Hiroaki Minamide. Real-time terahertz wave imaging by nonlinear optical frequency up-conversion in a $4-\text{dimethylamino}-\text{N}'-\text{methyl}-4'-\text{stilbazoliumtosylate}$. *Applied Physics Letters*, 104(10):101106, 2014.

[72] C. G. Wade, N. Šibalić, N. R. de Melo, J. M. Kondo, C. S. Adams, and K. J. Weatherill. Real-time near-field terahertz imaging with atomic optical fluorescence. *Nature Photonics*, 11(1):40–43, Jan 2017.

[73] Lucy A Downes, Andrew R MacKellar, Daniel J Whiting, Cyril Bourgenot, Charles S Adams, and Kevin J Weatherill. Full-field terahertz imaging at kilohertz frame rates using atomic vapor. *Physical Review X*, 10(1):011027, 2020.

[74] Thomas F Gallagher. Rydberg atoms. *Reports on Progress in Physics*, 51(2):143, 1988.

[75] T Gallagher. Cambridge monographs on atomic, molecular and chemical physics. *Rydberg atoms*, 1994.

[76] Mark Saffman, Thad G Walker, and Klaus Mølmer. Quantum information with rydberg atoms. *Reviews of modern physics*, 82(3):2313, 2010.

[77] M Saffman and TG Walker. Creating single-atom and single-photon sources from entangled atomic ensembles. *Physical Review A*, 66(6):065403, 2002.

[78] Kirk W Madison. *Annual Review of Cold Atoms and Molecules*. World Scientific, 2013.

[79] Hendrik Weimer, Markus Müller, Igor Lesanovsky, Peter Zoller, and Hans Peter Büchler. A rydberg quantum simulator. *Nature Physics*, 6(5):382–388, 2010.

[80] Jonathon A. Sedlacek, Arne Schwettmann, Harald Kübler, Robert Löw, Tilman Pfau, and James P. Shaffer. Microwave electrometry with rydberg atoms in a vapour cell using bright atomic resonances. *Nature Physics*, 8(11):819–824, Nov 2012.

[81] Shuying Chen, Dominic J Reed, Andrew R MacKellar, Lucy A Downes, Nourah FA Almuhawish, Matthew J Jamieson, Charles S Adams, and Kevin J Weatherill. Terahertz electrometry via infrared spectroscopy of atomic vapor. *Optica*, 9(5):485–491, 2022.

[82] Vera Bendkowsky, Björn Butscher, Johannes Nipper, James P Shaffer, Robert Löw, and Tilman Pfau. Observation of ultralong-range rydberg molecules. *Nature*, 458(7241):1005–1008, 2009.

[83] HQ Fan, S Kumar, R Daschner, H Kübler, and JP Shaffer. Subwavelength microwave electric-field imaging using rydberg atoms inside atomic vapor cells. *Optics Letters*, 39(10):3030–3033, 2014.

[84] Christopher L Holloway, Joshua A Gordon, Andrew Schwarzkopf, David A Anderson, Stephanie A Miller, Nithiwadee Thaicharoen, and Georg Raithel. Sub-wavelength imaging and field mapping via electromagnetically induced transparency and autler-townes splitting in rydberg atoms. *Applied Physics Letters*, 104(24):244102, 2014.

[85] Christopher G Wade, Matteo Marcuzzi, Emanuele Levi, Jorge M Kondo, Igor Lesanovsky, Charles S Adams, and Kevin J Weatherill. A terahertz-driven non-equilibrium phase transition in a room temperature atomic vapour. *Nature communications*, 9(1):1–7, 2018.

[86] David Alexander Anderson, Rachel Elizabeth Sapiro, and Georg Raithel. An atomic receiver for am and fm radio communication. *IEEE Transactions on Antennas and Propagation*, 69(5):2455–2462, 2020.

[87] DA Anderson, RE Sapiro, LF Gonçalves, R Cardman, and G Raithel. Optical radio-frequency phase measurement with an internal-state rydberg atom interferometer. *Physical Review Applied*, 17(4):044020, 2022.

[88] Matthew T Simons, Abdulaziz H Haddab, Joshua A Gordon, and Christopher L Holloway. A rydberg atom-based mixer: Measuring the phase of a radio frequency wave. *Applied Physics Letters*, 114(11):114101, 2019.

[89] Marcel Drabbels and LD Noordam. Infrared imaging camera based on a rydberg atom photodetector. *Applied physics letters*, 74(13):1797–1799, 1999.

[90] A Gürtler, AS Meijer, and WJ van der Zande. Imaging of terahertz radiation using a rydberg atom photocathode. *Applied physics letters*, 83(2):222–224, 2003.

[91] Charles S Adams, Jonathan D Pritchard, and James P Shaffer. Rydberg atom quantum technologies. *Journal of Physics B: Atomic, Molecular and Optical Physics*, 53(1):012002, 2019.

[92] Christopher L Holloway, Matthew T Simons, Joshua A Gordon, Perry F Wilson, Caitlyn M Cooke, David A Anderson, and Georg Raithel. Atom-based rf electric field metrology: from self-calibrated measurements to sub-wavelength and near-field imaging. *IEEE Transactions on Electromagnetic Compatibility*, 59(2):717–728, 2017.

[93] Christopher Holloway, Mathew Simons, Abdulaziz H Haddab, Joshua A Gordon, David A Anderson, Georg Raithel, and Steven Voran. A multiple-band rydberg atom-based receiver: Am/fm stereo reception. *IEEE Antennas and Propagation Magazine*, 63(3):63–76, 2020.

[94] LUCY DOWNES et al. *A high-speed THz imaging system based on THz-to-optical conversion in atomic vapour*. PhD thesis, Durham University, 2020.

[95] CJ Foot. Atomic physics, ser. *Oxford Master Series in Atomic, Optical and Laser Physics*, 5:134, 2005.

[96] B.Y Bransden and C.J Joachain. physics of atom and molecules. *Oxford University Press, New York*, 2005.

[97] Iulia Georgescu. Rubidium round-the-clock. *Nature Chemistry*, 7(12):1034–1034, 2015.

[98] Mark A Zentile, James Keaveney, Lee Weller, Daniel J Whiting, Charles S Adams, and Ifan G Hughes. Elecsus: A program to calculate the electric susceptibility of an atomic ensemble. *Computer Physics Communications*, 189:162–174, 2015.

[99] Jonathon A Sedlacek, Arne Schwettmann, Harald Kübler, Robert Löw, Tilman Pfau, and James P Shaffer. Microwave electrometry with rydberg atoms in a vapour cell using bright atomic resonances. *Nature Physics*, 8(11):819–824, 2012.

[100] TH Sander, J Preusser, R Mhaskar, J Kitching, L Trahms, and S Knappe. Magnetoencephalography with a chip-scale atomic magnetometer. *Biomedical optics express*, 3(5):981–990, 2012.

[101] Christopher G Wade, Nikola Šibalić, Natalia R de Melo, Jorge M Kondo, Charles S Adams, and Kevin J Weatherill. Real-time near-field terahertz imaging with atomic optical fluorescence. *Nature Photonics*, 11(1):40–43, 2017.

[102] Charles E Burkhardt and Jacob J Leventhal. *Topics in atomic physics*. Springer, 2006.

[103] Harold J Metcalf and Peter van der Straten. Evaporative cooling. In *Laser Cooling and Trapping*, pages 165–175. Springer, 1999.

[104] DM Brink and GR Satchler. Angular momentum, oxford library of the physical sciences. 1968.

[105] Jean-Christophe Pain. Some properties of wigner 3j coefficients: non-trivial zeros and connections to hypergeometric functions. *The European Physical Journal A*, 56(11):1–13, 2020.

[106] II Beterov, II Ryabtsev, DB Tretyakov, and VM Entin. Quasiclassical calculations of blackbody-radiation-induced depopulation rates and effective lifetimes of rydberg ns, np, and nd alkali-metal atoms with $n \leq 80$. *Physical review A*, 79(5):052504, 2009.

[107] Dieter Suter. *The physics of laser-atom interactions*. Number 19. Cambridge University Press, 1997.

[108] Stanley H Autler and Charles H Townes. Stark effect in rapidly varying fields. *Physical Review*, 100(2):703, 1955.

[109] Daniel A Steck. Cesium d line data. http://steck:us/alkalidata, November 2019.

[110] Paul Siddons, Charles S Adams, Chang Ge, and Ifan G Hughes. Absolute absorption on rubidium d lines: comparison between theory and experiment. *Journal of Physics B: Atomic, Molecular and Optical Physics*, 41(15):155004, 2008.

[111] Anthony Mark Fox, Mark Fox, et al. *Quantum optics: an introduction*, volume 15. Oxford university press, 2006.

[112] Karl Blum. *Density matrix theory and applications*, volume 64. Springer Science & Business Media, 2012.

[113] Julio Gea-Banacloche, Yong-qing Li, Shao-zheng Jin, and Min Xiao. Electromagnetically induced transparency in ladder-type inhomogeneously broadened media: Theory and experiment. *Physical Review A*, 51(1):576, 1995.

[114] CP Pearman, CS Adams, SG Cox, PF Griffin, DA Smith, and IG Hughes. Polarization spectroscopy of a closed atomic transition: applications to laser frequency locking. *Journal of Physics B: Atomic, Molecular and Optical Physics*, 35(24):5141, 2002.

[115] Christopher Carr, Charles S Adams, and Kevin J Weatherill. Polarization spectroscopy of an excited state transition. *Optics Letters*, 37(1):118–120, 2012.

[116] Robert W Boyd. The nonlinear optical susceptibility. *Nonlinear optics*, 3:1–67, 2008.

[117] Daniel A Steck. Cesium d line data. http://steck:us/alkalidata, July 2021.

[118] C Wieman and Th W Hänsch. Doppler-free laser polarization spectroscopy. *Physical Review Letters*, 36(20):1170, 1976.

[119] Eric D Black. An introduction to pound–drever–hall laser frequency stabilization. *American journal of physics*, 69(1):79–87, 2001.

[120] Virginia Diodes Inc.,. Feedhorn summary. https://www:vadiodes:com/images/appnotes/vdi_feedhorn_summary_2020.05.04. pdf, 2020., Accessed: August 2020.

[121] Arthur D Edelstein, Mark A Tsuchida, Nenad Amodaj, Henry Pinkard, Ronald D Vale, and Nico Stuurman. Advanced methods of microscope control using μmanager software. *Journal of biological methods*, 1(2), 2014.

[122] Bahaa EA Saleh and Malvin Carl Teich. *Fundamentals of photonics*. john Wiley & sons, 2019.

[123] https://www.sukhamburg.com/.

[124] https://www.i2s.fr/en/category/terahertz-cameras.

[125] D Grischkowsky, Søren Keiding, Martin Van Exter, and Ch Fattinger. Far-infrared time-domain spectroscopy with terahertz beams of dielectrics and semiconductors. *JOSA B*, 7(10):2006–2015, 1990.

[126] Radoslaw Piesiewicz, Christian Jansen, S Wietzke, Daniel Mittleman, Martin Koch, and Thomas Kürner. Properties of building and plastic materials in the thz range. *International Journal of Infrared and Millimeter Waves*, 28(5):363–371, 2007.

[127] Gombo E Tsydynzhapov, Pavel A Gusikhin, Vyacheslav M Muravev, Ivan V Andreev, and Igor V Kukushkin. New terahertz security body scanner. In *2018 43rd International Conference on Infrared, Millimeter, and Terahertz Waves (IRMMW-THz)*, pages 1–1. IEEE, 2018.

[128] Jiamin Zhang, Dong Xu, Feng Dong, Ruixiao Wang, Quan Yang, Xiaochen Wang, and Renjie Xue. Solid–liquid interface reconstruction for sandwich structure metal plate via laser-ultrasonic techniques. *Review of Scientific Instruments*, 92(12):123003, 2021.

[129] Zhi Qu, Peng Jiang, and Weixu Zhang. Development and application of infrared thermography non-destructive testing techniques. *Sensors*, 20(14):3851, 2020.

[130] S Wietzke, C Jansen, N Krumbholz, O Peters, N Vieweg, C Jördens, M Scheller, D Romeike, T Jung, M Reuter, et al. Terahertz spectroscopy: A powerful tool for the characterization of plastic materials. In *2010 10th IEEE International Conference on Solid Dielectrics*, pages 1–4. IEEE, 2010.

[131] Andries Küter, Stefan Reible, Thomas Geibig, Dirk Nüßler, and Nils Pohl. Thz imaging for recycling of black plastics. *tm-Technisches Messen*, 85(3):191–201, 2018.

[132] Matthew C Beard, Gordon M Turner, and Charles A Schmuttenmaer. Subpicosecond carrier dynamics in low-temperature grown gaas as measured by time-resolved terahertz spectroscopy. *Journal of Applied Physics*, 90(12):5915–5923, 2001.

[133] P Haring Bolivar, Martin Brucherseifer, J Gómez Rivas, Ramón Gonzalo, Iñigo Ederra, Andrew L Reynolds, M Holker, and Peter De Maagt. Measurement of the dielectric constant and loss tangent of high dielectric-constant materials at terahertz frequencies. *IEEE Transactions on Microwave Theory and Techniques*, 51(4):1062–1066, 2003.

[134] Seiji Niijima, Masashi Shoyama, Kazumi Murakami, and Kodo Kawase. Evaluation of the sintering properties of pottery bodies using terahertz time-domain spectroscopy. *Journal of Asian Ceramic Societies*, 6(1):37–42, 2018.

[135] Mikhail Mikerov, Rabi Shrestha, Peter van Dommelen, Daniel M Mittleman, and Martin Koch. Analysis of ancient ceramics using terahertz imaging and photogrammetry. *Optics Express*, 28(15):22255–22263, 2020.

[136] Tara M Todoruk, Ian D Hartley, and Matthew E Reid. Origin of birefringence in wood at terahertz frequencies. *IEEE Transactions on Terahertz Science and Technology*, 2(1):123–130, 2011.

[137] Soichi Tanaka, Keiichiro Shiraga, Yuichi Ogawa, Yoshihisa Fujii, and Shogo Okumura. Applicability of effective medium theory to wood density measurements using terahertz time-domain spectroscopy. *Journal of wood science*, 60(2):111–116, 2014.

[138] Peter Zolliker, Markus Rüggeberg, Lorenzo Valzania, and Erwin Hack. Extracting wood properties from structured thz spectra: birefringence and water content. *IEEE Transactions on Terahertz Science and Technology*, 7(6):722–731, 2017.

[139] Y Watanabe, K Kawase, T Ikari, H Ito, Y Ishikawa, and H Minamide. Component analysis of chemical mixtures using terahertz spectroscopic imaging. *Optics Communications*, 234(1-6):125–129, 2004.

[140] H Harde, J Zhao, Marcus Wolff, RA Cheville, and D Grischkowsky. Thz time-domain spectroscopy on ammonia. *The Journal of Physical Chemistry A*, 105(25):6038–6047, 2001.

[141] Yoshio Wada, Yoshiharu Urata, Hiroshi Ito, and Yasuhiro Higashi. Measuring material parameters using a tunable monochromatic terahertz wave source. *Applied Optics*, 59(32):10035–10042, 2020.

[142] Md Saiful Islam, Cristiano MB Cordeiro, Md J Nine, Jakeya Sultana, Alice LS Cruz, Alex Dinovitser, Brian Wai-Him Ng, Heike Ebendorff-Heidepriem, Dusan Losic, and Derek Abbott. Experimental study on glass and polymers:

Determining the optimal material for potential use in terahertz technology. *IEEE access*, 8:97204–97214, 2020.

[143] Yun-Sik Jin, Geun-Ju Kim, and Seok-Gy Jeon. Terahertz dielectric properties of polymers. *Journal of the Korean Physical Society*, 49(2):513–517, 2006.

[144] Benedikt Scherger, Steffen Wietzke, Maik Scheller, Nico Vieweg, Matthias Wichmann, Martin Koch, and Karin Wiesauer. Characterization of micropowders for the fabrication of compression molded thz lenses. *Journal of Infrared, Millimeter, and Terahertz Waves*, 32(7):943–951, 2011.

[145] Benedikt Scherger, Maik Scheller, Christian Jansen, Martin Koch, and Karin Wiesauer. Terahertz lenses made by compression molding of micropowders. *Applied optics*, 50(15):2256–2262, 2011.

[146] Stefan F Busch, Norman Born, Martin Koch, and Bernd Fischer. Terahertz reflection gratings made by room-temperature high-pressure molding. *Journal of Infrared, Millimeter, and Terahertz Waves*, 34(7):413–415, 2013.

[147] R. A. Lewis. *Terahertz Physics*. Cambridge University Press, 2013.

[148] N Krumbholz, K Gerlach, F Rutz, M Koch, R Piesiewicz, T Kürner, and D Mittleman. Omnidirectional terahertz mirrors: A key element for future terahertz communication systems. *Applied Physics Letters*, 88(20):202905, 2006.

[149] Christian Jördens, Kin Lien Chee, Ibraheem AI Al-Naib, Ioachim Pupeza, Sören Peik, Gerhard Wenke, and Martin Koch. Dielectric fibres for low-loss transmission of millimetre waves and its application in couplers and splitters. *Journal of Infrared, Millimeter, and Terahertz Waves*, 31(2):214–220, 2010.

[150] Claudia Goy, Maik Scheller, Benedikt Scherger, Vincent P Wallace, and Martin Koch. Terahertz waveguide prism. *Optics express*, 21(16):19292–19301, 2013.

[151] Mira Naftaly and Robert E Miles. Terahertz time-domain spectroscopy for material characterization. *Proceedings of the IEEE*, 95(8):1658–1665, 2007.

[152] EV Fedulova, Maxim M Nazarov, AA Angeluts, MS Kitai, VI Sokolov, and AP Shkurinov. Studying of dielectric properties of polymers in the terahertz frequency range. In *Saratov Fall Meeting 2011: Optical Technologies in Biophysics and Medicine XIII*, volume 8337, page 83370I. International Society for Optics and Photonics, 2012.

[153] M Hangyo, T Nagashima, and S Nashima. Spectroscopy by pulsed terahertz radiation. *Measurement Science and Technology*, 13(11):1727, 2002.

[154] F Mohamed, RA Zaghlool, and W El Hotaby. Terahertz spectroscopic analysis of non-radiated and radiated synthetic and natural polymer/go nanocomposites. *Journal of Molecular Structure*, 1250:131659, 2022.

[155] Muhammad Mumtaz, M Ahsan Mahmood, Sabih D Khan, M Aslam Zia, Mushtaq Ahmed, and Izhar Ahmad. Experimental measurement of temperature-dependent sellmeier coefficients and thermo-optic coefficients of polymers in terahertz spectral range. *Optical Materials*, 91:126–129, 2019.

[156] Lars Liebermeister, Simon Nellen, Robert B Kohlhaas, Sebastian Lauck, Milan Deumer, Steffen Breuer, Martin Schell, and Björn Globisch. Optoelectronic frequency-modulated continuous-wave terahertz spectroscopy with 4 thz bandwidth. *Nature Communications*, 12(1):1–10, 2021.

[157] Lars Liebermeister, Simon Nellen, Robert B Kohlhaas, Sebastian Lauck, Milan Deumer, Steffen Breuer, Martin Schell, and Björn Globisch. Terahertz multilayer thickness measurements: Comparison of optoelectronic time and frequency domain systems. *Journal of Infrared, Millimeter, and Terahertz Waves*, 42(11):1153–1167, 2021.

[158] S Mair, B Gompf, and M Dressel. Microspectroscopy and imaging in the thz range using coherent cw radiation. *Physics in Medicine & Biology*, 47(21):3719, 2002.

[159] Charles S Adams and Ifan G Hughes. *Optics f2f: from Fourier to Fresnel*. Oxford University Press, 2018.

[160] https://www.vadiodes.com/en/power-meter-pm5.

[161] Clive R Siviour and Jennifer L Jordan. High strain rate mechanics of polymers: a review. *Journal of Dynamic Behavior of Materials*, 2(1):15–32, 2016.

[162] Yun-Shik Lee. *Principles of terahertz science and technology*, volume 170. Springer Science & Business Media, 2009.

[163] Hichem Guerboukha, Kathirvel Nallappan, and Maksim Skorobogatiy. Toward real-time terahertz imaging. *Advances in Optics and Photonics*, 10(4):843–938, 2018.

[164] J Axel Zeitler and Yao-Chun Shen. Industrial applications of terahertz imaging. In *Terahertz spectroscopy and imaging*, pages 451–489. Springer, 2012.

[165] Frank Rutz, Martin Koch, Shilpa Khare, Martin Moneke, Heike Richter, and Uwe Ewert. Terahertz quality control of polymeric products. *International Journal of Infrared and Millimeter Waves*, 27(4):547–556, 2006.

[166] Dirk Nüßler and Joachim Jonuscheit. Terahertz based non-destructive testing (ndt). *tm-Technisches Messen*, 88(4):199–210, 2021.

[167] Yu Heng Tao, Anthony J Fitzgerald, and Vincent P Wallace. Non-contact, non-destructive testing in various industrial sectors with terahertz technology. *Sensors*, 20(3):712, 2020.

[168] Shujie Fan, Tongchun Li, Jun Zhou, Xiaoqing Liu, Xiaoming Liu, Huijun Qi, and Zhiyong Mu. Terahertz non-destructive imaging of cracks and cracking in structures of cement-based materials. *AIP Advances*, 7(11):115202, 2017.

[169] Hua Zhong, Jingzhou Xu, Xu Xie, Tao Yuan, Ron Reightler, Eric Madaras, and Xi-Cheng Zhang. Nondestructive defect identification with terahertz time-of-flight tomography. *IEEE Sensors Journal*, 5(2):203–208, 2005.

[170] Kiarash Ahi, Navid Asadizanjani, Sina Shahbazmohamadi, Mark Tehranipoor, and Mehdi Anwar. Terahertz characterization of electronic components and comparison of terahertz imaging with x-ray imaging techniques. In *Terahertz Physics, Devices, and Systems IX: Advanced Applications in Industry and Defense*, volume 9483, page 94830K. International Society for Optics and Photonics, 2015.

[171] Ji-Yang Zhang, Jiao-Jiao Ren, Li-Juan Li, Jian Gu, and Dan-Dan Zhang. Thz imaging technique for nondestructive analysis of debonding defects in ceramic matrix composites based on multiple echoes and feature fusion. *Optics express*, 28(14):19901–19915, 2020.

[172] Kiarash Ahi, Sina Shahbazmohamadi, and Navid Asadizanjani. Quality control and authentication of packaged integrated circuits using enhanced-spatial-resolution terahertz time-domain spectroscopy and imaging. *Optics and Lasers in Engineering*, 104:274–284, 2018.

[173] Jong Hyuk Yim, Su-yeon Kim, Yiseob Kim, Suyoung Cho, Jangsun Kim, and Yeong Hwan Ahn. Rapid 3d-imaging of semiconductor chips using thz time-of-flight technique. *Applied Sciences*, 11(11):4770, 2021.

[174] Qi Mao, Yunlong Zhu, Cixing Lv, Yao Lu, Xiaohui Yan, Shihan Yan, and Jingbo Liu. Convolutional neural network model based on terahertz imaging for integrated circuit defect detections. *Optics express*, 28(4):5000–5012, 2020.

[175] Zhang Zhenwei, Xu Jing, Jia Rui, Wu Yinghong, Guan Hao, Han Siyi, Zhang Cunlin, and Zhao Yuejin. Terahertz non-destructive testing and imaging of high-voltage cables. *Frontiers in Physics*, page 383, 2022.

[176] Ho-Jin Song and Tadao Nagatsuma. *Handbook of terahertz technologies: devices and applications*. CRC press, 2015.

[177] GG Hernandez-Cardoso, SC Rojas-Landeros, M Alfaro-Gomez, AI Hernandez-Serrano, I Salas-Gutierrez, E Lemus-Bedolla, AR Castillo-Guzman, HL Lopez-Lemus, and E Castro-Camus. Terahertz imaging for early screening of diabetic foot syndrome: A proof of concept. *Scientific reports*, 7(1):1–9, 2017.

[178] Cecil S Joseph, Rakesh Patel, Victor A Neel, Robert H Giles, and Anna N Yaroslavsky. Imaging of ex vivo nonmelanoma skin cancers in the optical and terahertz spectral regions optical and terahertz skin cancers imaging. *Journal of biophotonics*, 7(5):295–303, 2014.

[179] Anil Jain, Ruud Bolle, and Sharath Pankanti. *Biometrics: personal identification in networked society*, volume 479. Springer Science & Business Media, 1999.

[180] Anil K Jain, Karthik Nandakumar, and Arun Ross. 50 years of biometric research: Accomplishments, challenges, and opportunities. *Pattern recognition letters*, 79:80–105, 2016.

[181] Bozhao Tan and Stephanie Schuckers. Spoofing protection for fingerprint scanner by fusing ridge signal and valley noise. *Pattern Recognition*, 43(8):2845–2857, 2010.

[182] Ctirad Sousedik and Christoph Busch. Presentation attack detection methods for fingerprint recognition systems: a survey. *Iet Biometrics*, 3(4):219–233, 2014.

[183] Shoude Chang, Kirill V Larin, Youxin Mao, Costel Flueraru, and Wahab Almuhtadi. Fingerprint spoof detection using near infrared optical analysis. *State of the Art in Biometrics*, pages 57–84, 2011.

[184] Kristin Adair Nixon, Valerio Aimale, and Robert K Rowe. Spoof detection schemes. In *Handbook of biometrics*, pages 403–423. Springer, 2008.

[185] Davide Maltoni, Dario Maio, Anil K Jain, and Salil Prabhakar. Synthetic fingerprint generation. *Handbook of fingerprint recognition*, pages 271–302, 2009.

[186] Panagiotis C Theofanopoulos and Georgios C Trichopoulos. A novel fingerprint scanning method using terahertz imaging. In *2018 IEEE International Symposium on Antennas and Propagation & USNC/URSI National Radio Science Meeting*, pages 2463–2464. IEEE, 2018.

[187] Norbert Pałka and Marcin Kowalski. Towards fingerprint spoofing detection in the terahertz range. *Sensors*, 20(12):3379, 2020.

[188] Angelina I Nikitkina, Polina Bikmulina, Elvira R Gafarova, Nastasia V Kosheleva, Yuri M Efremov, Evgeny A Bezrukov, Denis V Butnaru, Irina N Dolganova, Nikita V Chernomyrdin, Olga P Cherkasova, et al. Terahertz radiation and the skin: a review. *Journal of Biomedical Optics*, 26(4):043005, 2021.

[189] Borwen You, Ching-Yu Chen, Chin-Ping Yu, Pei-Hwa Wang, and Ja-Yu Lu. Frequency-dependent skin penetration depth of terahertz radiation determined by water sorption–desorption. *Optics express*, 26(18):22709–22721, 2018.

[190] Qiushuo Sun, Edward PJ Parrott, Yuezhi He, and Emma Pickwell-MacPherson. In vivo thz imaging of human skin: Accounting for occlusion effects. *Journal of biophotonics*, 11(2):e201700111, 2018.

[191] Jiarui Wang, Rayko I Stantchev, Qiushuo Sun, Tor-Wo Chiu, Anil T Ahuja, and Emma Pickwell MacPherson. Thz in vivo measurements: the effects of pressure on skin reflectivity. *Biomedical optics express*, 9(12):6467–6476, 2018.

[192] Ilya Ozheredov, Mikhail Prokopchuk, Mikhail Mischenko, Tatiana Safonova, Petr Solyankin, Andrey Larichev, Andrey Angeluts, Alexei Balakin, and Alexander Shkurinov. In vivo thz sensing of the cornea of the eye. *Laser Physics Letters*, 15(5):055601, 2018.

[193] Françoise Viallefont-Robinet, Dennis Helder, Renaud Fraisse, Amy Newbury, Frans van den Bergh, DongHan Lee, and Sébastien Saunier. Comparison of mtf measurements using edge method: towards reference data set. *Optics express*, 26(26):33625–33648, 2018.

[194] Marc Offroy, Myriam Moreau, Sophie Sobanska, Peyman Milanfar, and Ludovic Duponchel. Pushing back the limits of raman imaging by coupling super-resolution and chemometrics for aerosols characterization. *Scientific reports*, 5(1):1–14, 2015.

[195] Daniel M Mittleman, Stefan Hunsche, Luc Boivin, and Martin C Nuss. T-ray tomography. *Optics letters*, 22(12):904–906, 1997.

[196] Christian Jansen, Steffen Wietzke, Ole Peters, Maik Scheller, Nico Vieweg, Mohammed Salhi, Norman Krumbholz, Christian Jördens, Thomas Hochrein, and Martin Koch. Terahertz imaging: applications and perspectives. *Applied optics*, 49(19):E48–E57, 2010.

[197] P Uhd Jepsen, David G Cooke, and Martin Koch. Terahertz spectroscopy and imaging–modern techniques and applications. *Laser & Photonics Reviews*, 5(1):124–166, 2011.

[198] Andrew Chen, Arjun Virk, Zachery Harris, Azin Abazari, Robert Honkanen, and M Hassan Arbab. Non-contact terahertz spectroscopic measurement of the intraocular pressure through corneal hydration mapping. *Biomedical Optics Express*, 12(6):3438–3449, 2021.

[199] Zhengyong Song, Zhen Gao, Youming Zhang, and Baile Zhang. Terahertz transparency of optically opaque metallic films. *EPL (Europhysics Letters)*, 106(2):27005, 2014.

[200] Vincent P Wallace, Emma MacPherson, J Axel Zeitler, and Caroline Reid. Three-dimensional imaging of optically opaque materials using nonionizing terahertz radiation. *JOSA A*, 25(12):3120–3133, 2008.

[201] Michael Pecht et al. The counterfeit electronics problem. *Open Journal of Social Sciences*, 1(07):12, 2013.

[202] Wing Chiu Jason Tam and Ronald D Shawn Blanton. Lasic: Layout analysis for systematic ic-defect identification using clustering. *IEEE Transactions on Computer-Aided Design of Integrated Circuits and Systems*, 34(8):1278–1290, 2015.

[203] Ssu-Han Chen and Der-Baau Perng. Automatic optical inspection system for ic molding surface. *Journal of Intelligent Manufacturing*, 27(5):915–926, 2016.

[204] Shuye Zhang, Xiangyu Xu, Tiesong Lin, and Peng He. Recent advances in nano-materials for packaging of electronic devices. *Journal of Materials Science: Materials in Electronics*, 30(15):13855–13868, 2019.

[205] Thomas D Moore, Daniel Vanderstraeten, and Pia M Forssell. Three-dimensional x-ray laminography as a tool for detection and characterization of bga package defects. *IEEE Transactions on Components and Packaging Technologies*, 25(2):224–229, 2002.

[206] Chan Zheng, Zheyu Song, Shihan Yan, Jingbo Liu, Dongxiong Ling, Dongshan Wei, and Jinyun Zhou. Enhanced terahertz imaging of electronic packaging materials with deconvolution algorithm. In *2019 International Conference on Optical Instruments and Technology: IRMMW-THz Technologies*

and Applications, volume 11441, page 114410D. International Society for Optics and Photonics, 2020.

[207] Nikola Šibalić, Jonathan D Pritchard, Charles S Adams, and Kevin J Weatherill. Arc: An open-source library for calculating properties of alkali rydberg atoms. *Computer Physics Communications*, 220:319–331, 2017.

[208] Xin He, Paul Beckett, and Ranjith R Unnithan. Hybrid color filters for multispectral imaging. In *Multispectral Image Sensors Using Metasurfaces*, pages 87–97. Springer, 2021.

[209] Zhongping Lee, Kendall L Carder, Curtis D Mobley, Robert G Steward, and Jennifer S Patch. Hyperspectral remote sensing for shallow waters. i. a semianalytical model. *Applied optics*, 37(27):6329–6338, 1998.

[210] J Anthony Gualtieri and Robert F Cromp. Support vector machines for hyperspectral remote sensing classification. In *27th AIPR workshop: advances in computer-assisted recognition*, volume 3584, pages 221–232. SPIE, 1999.

[211] Bo-Cai Gao, Marcos J Montes, Ziauddin Ahmad, and Curtiss O Davis. Atmospheric correction algorithm for hyperspectral remote sensing of ocean color from space. *Applied optics*, 39(6):887–896, 2000.

[212] Oscar Carrasco, Richard B Gomez, Arun Chainani, and William E Roper. Hyperspectral imaging applied to medical diagnoses and food safety. In *Geo-Spatial and Temporal Image and Data Exploitation III*, volume 5097, pages 215–221. SPIE, 2003.

[213] Martin A Afromowitz, JAMES B Callis, DAVID M Heimbach, LARRY A DeSoto, and MARY KAYE Norton. Multispectral imaging of burn wounds: a new clinical instrument for evaluating burn depth. *IEEE Transactions on Biomedical Engineering*, 35(10):842–850, 1988.

[214] Wen-Lou Liu, Lin-Wei Wang, Jia-Mei Chen, Jing-Ping Yuan, Qing-Ming Xiang, Gui-Fang Yang, Ai-Ping Qu, Juan Liu, and Yan Li. Application of

multispectral imaging in quantitative immunohistochemistry study of breast cancer: a comparative study. *Tumor Biology*, 37(4):5013–5024, 2016.

[215] Christian Fischer and Ioanna Kakoulli. Multispectral and hyperspectral imaging technologies in conservation: current research and potential applications. *Studies in Conservation*, 51(sup1):3–16, 2006.

[216] Yao-Ze Feng and Da-Wen Sun. Application of hyperspectral imaging in food safety inspection and control: a review. *Critical reviews in food science and nutrition*, 52(11):1039–1058, 2012.

[217] Megandhren Govender, Kershani Chetty, and Hartley Bulcock. A review of hyperspectral remote sensing and its application in vegetation and water resource studies. *Water Sa*, 33(2):145–151, 2007.

[218] Elhadi Adam, Onisimo Mutanga, and Denis Rugege. Multispectral and hyperspectral remote sensing for identification and mapping of wetland vegetation: a review. *Wetlands Ecology and Management*, 18(3):281–296, 2010.

[219] Haida Liang. Advances in multispectral and hyperspectral imaging for archaeology and art conservation. *Applied Physics A*, 106(2):309–323, 2012.

[220] Jaana Kuula, Ilkka Pölönen, Hannu-Heikki Puupponen, Tuomas Selander, Tapani Reinikainen, Tapani Kalenius, and Heikki Saari. Using vis/nir and ir spectral cameras for detecting and separating crime scene details. In *Sensors, and Command, Control, Communications, and Intelligence (C3I) Technologies for Homeland Security and Homeland Defense XI*, volume 8359, pages 150–160. SPIE, 2012.

[221] Valerie C Coffey. Multispectral imaging moves into the mainstream. *Optics and Photonics News*, 23(4):18–24, 2012.

[222] Marwan Abuleil and Ibrahim Abdulhalim. Narrowband multispectral liquid crystal tunable filter. *Optics Letters*, 41(9):1957–1960, 2016.

[223] Jeffrey JL Carson, Mohamadreza Najiminaini, Fartash Vasefi, and Bozena Kaminska. Nanostructure-based optical filters for multispectral imaging applications. In *AIP Conference Proceedings*, volume 1590, pages 57–63. American Institute of Physics, 2014.

[224] Raju Shrestha and Jon Yngve Hardeberg. Multispectral image capture using two rgb cameras. In *2010 18th European Signal Processing Conference*, pages 1801–1805. IEEE, 2010.

[225] Marc Moncrieff, Symon Cotton, Elzbieta Claridge, and Per Hall. Spectrophotometric intracutaneous analysis: a new technique for imaging pigmented skin lesions. *British Journal of Dermatology*, 146(3):448–457, 2002.

[226] Romuald Jolivot, Yannick Benezeth, and Franck Marzani. Skin parameter map retrieval from a dedicated multispectral imaging system applied to dermatology/cosmetology. *International journal of biomedical imaging*, 2013, 2013.

[227] Paul Dean, Nor Kamila Saat, Suraj P Khanna, Mohammed Salih, Andrew Burnett, John Cunningham, Edmund H Linfield, and A Giles Davies. Dual-frequency imaging using an electrically tunable terahertz quantum cascade laser. *Optics express*, 17(23):20631–20641, 2009.

[228] Nor Kamilah Saat, Paul Dean, Suraj P Khanna, Mohamed Salih, A Giles Davies, and Edmund H Linfield. Multiple-frequency imaging using a terahertz quantum cascade laser. In *35th International Conference on Infrared, Millimeter, and Terahertz Waves*, pages 1–2. IEEE, 2010.

[229] Nourah F Almuhawish, Shuying Chen, Lucy A Downes, Matthew J Jamieson, Andrew R MacKellar, and Kevin J Weatherill. Polarization spectroscopy of an excited state transition in rubidium. *OSA Continuum*, 4(10):2598–2605, 2021.

[230] Robert W Boyd. *Nonlinear optics*. Academic Press, 2020.

[231] AK Mohapatra, TR Jackson, and CS Adams. Coherent optical detection of highly excited rydberg states using electromagnetically induced transparency. *Physical review letters*, 98(11):113003, 2007.

[232] M Tanasittikosol, C Carr, CS Adams, and KJ Weatherill. Subnatural linewidths in two-photon excited-state spectroscopy. *Physical Review A*, 85(3):033830, 2012.

[233] CY Ye, AS Zibrov, Yu V Rostovtsev, and MO Scully. Unexpected doppler-free resonance in generalized double dark states. *Physical Review A*, 65(4):043805, 2002.

[234] MG Bason, AK Mohapatra, KJ Weatherill, and CS Adams. Narrow absorptive resonances in a four-level atomic system. *Journal of Physics B: Atomic, Molecular and Optical Physics*, 42(7):075503, 2009.

[235] Daniel J Whiting, Erwan Bimbard, James Keaveney, Mark A Zentile, Charles S Adams, and Ifan G Hughes. Electromagnetically induced absorption in a nondegenerate three-level ladder system. *Optics letters*, 40(18):4289–4292, 2015.

[236] Patrick Rizk, Rafic Younes, Adrian Ilinca, and Jihan Khoder. Wind turbine blade defect detection using hyperspectral imaging. *Remote Sensing Applications: Society and Environment*, 22:100522, 2021.

[237] Atsushi Nakanishi, Koichiro Akiyama, Shohei Hayashi, Hiroshi Satozono, and Kazuue Fujita. Spectral imaging of pharmaceutical materials with a compact terahertz difference-frequency generation semiconductor source. *Analytical Methods*, 13(46):5549–5554, 2021.

[238] John F Federici, Brian Schulkin, Feng Huang, Dale Gary, Robert Barat, Filipe Oliveira, and David Zimdars. Thz imaging and sensing for security applications—explosives, weapons and drugs. *Semiconductor Science and Technology*, 20(7):S266, 2005.

[239] John F Federici, Louis Rizzo, Alexander Clark, Christopher Bolton, Samuel Gatley, and Ian Gatley. Industrial applications of thz imaging: Plastics, food industry, moisture detection, and additive manufacturing. In *Applied Industrial Spectroscopy*, pages AW4I–1. Optical Society of America, 2020.

Appendix A

Correct The Spatial Resolution By The Magnification Factor

In Fig.5.4 we can see the THz beam after being launched from the horn and is collimated by the Teflon lens. This collimated beam will illuminate the letter "T" sample at the imaging plane, then it will be imaged onto the light sheet imager in the vapour cell by using optical system M1, and then the letter will be re-imaged in the optical camera by using a second optical system M2. In order to determine the spatial resolution of the system, we have placed our occlusion in the imaging plane that has been imaged in our light sheet imager, which was then re-imaged in our optical camera, which will be our data image. This image is converted to a 1D array and the derivative was calculated to obtain a peak that has a width which is obtained by knowing the scale of the magnification factor, M2. Our spatial resolution needs to be corrected by finding the scale of the magnification factor where the actual object is placed (M1). M1 is a commercial THz lens system that is discussed in Chapter 3 and is designed to have a 1:4 magnification according to the placement of the object. This magnification can be calculated from the real size and the size of the image of the letter "T" in our piece sample. Since the letter "T" has a non-uniform shape, the real size can be calculated by measuring the size of the letter "T" using a travelling microscope. The magnification M1 which can

be expressed as:

$$\mathrm{M1} = \frac{\text{Image size}}{\text{object size}}. \tag{A.1}$$

$$\text{object size} = 8.86 \pm 0.07 \text{ mm}. \tag{A.2}$$

where the error in the real scale is the statistical deviation of five measurements. For the imaging scale, again, we have two different THz frequencies that have been used, we have measured the width of the letter "T" in pixels by using 0.55 THz frequency to be $N_{(0.55)} = (354 \pm 10)$ pixels, and for the 1.1 THz frequency $N_{(1.1)} = (331 \pm 10)$ pixels. The image scales for both frequencies can be written as:

$$\begin{aligned} \text{image size}_{(0.55)} &= N_{(0.55)} \times \text{ converter} \\ &= 4.78 \pm 0.14 \text{ mm}. \end{aligned} \tag{A.3}$$

$$\begin{aligned} \text{image size}_{(1.1)} &= N_{(1.1)} \times \text{ converter} \\ &= 4.47 \pm 0.14 \text{ mm}. \end{aligned} \tag{A.4}$$

By inserting Eq.A.2, Eq.A.3 and Eq.A.4 in Eq.A.1 we can obtain the magnification factor, M1, for 0.55 and 1.1 THz frequencies.

$$\mathrm{M1}_{(0.55)} = 0.54 \pm 0.02, \tag{A.5}$$

$$\mathrm{M1}_{(1.1)} = 0.50 \pm 0.02. \tag{A.6}$$

To obtain the corrected spatial resolution, we substitute the width and magnification factor M1 from Eq.5.2 and Eq.A.5 for 0.55 THz, Eq.5.3 and Eq.A.6 for 1.1 THz into Eq.5.4:

$$\begin{aligned} \text{Spatial resolution}_{(0.55)} &= \frac{\text{Width}_{(0.55)}}{\text{M1}_{(0.55)}} \\ &= 0.78 \pm 0.07 \text{ mm}, \end{aligned} \tag{A.7}$$

$$\begin{aligned} \text{Spatial resolution}_{(1.1)} &= \frac{\text{Width}_{(1.1)}}{\text{M1}_{(1.1)}} \\ &= 0.59 \pm 0.08 \text{ mm}. \end{aligned} \tag{A.8}$$